Investigation of The Corrosion Behavior of Metallic Aluminum Embedded in A Cement Matrix

By
Alfred Gurning

A Thesis done in
SCK•CEN

Presented to
INP Phelma Grenoble and UPC Barcelona

As Part of
European Master in Nuclear Energy (EMINE)

Supervisor: Sébastien Caes (sebastien.caes@sckcen.be)
Academic Referee: Luc Salvo (luc.salvo@grenoble-inp.fr)

Done in the academic year of
2018/2019

ACKNOWLEDGMENTS

First and foremost, praises and thanks to God Almighty, Jesus Christ, for only by his grace and blessings throughout my master program I am able to finish this master thesis. I am also grateful for my family, especially my father, mother, and sister for all of their support during my time working on this master thesis and during my master study. I am also thankful from all the support from my friends during my master program, especially friends from PPI Spanyol, PPI Grenoble, PPI Antwerp, and Indoenergy.

I would like to express my deep and sincere gratitude to SCK•CEN and all of the person that really helps me during my master thesis research. I am thankful to my supervisor Sébastien Caes for all his support and guidance during my master thesis. I am thankful to Bruno Kursten and Elie Valcke for guiding and helping me to write the master thesis with all the constructive comments. I am thankful to Pieter Schroeders, Sabrina Lunardi, Stef Geukens, and Wim Verwimp for all the help during my lab work and experiment. I am grateful for the opportunity of doing my master thesis with the R&D Waste Packages team at SCK•CEN.

Finally, I am extremely grateful to Innoenergy for giving me the opportunity to do the European Master in Nuclear Energy (EMINE) program. I am thankful to all of the lecturers in UPC Barcelona and INP Phelma Grenoble for the learning opportunity and knowledge that has been shared. I am thankful to all my friends during my study in UPC Barcelona and INP Phelma Grenoble for the opportunity to know all of them and able to make friends from different parts of the world.

TABLE OF CONTENT

ACKNOWLEDGMENTS i

TABLE OF CONTENT ii

LIST OF TABLES iv

LIST OF FIGURES v

LIST OF ACRONYMS vii

LIST OF APPENDIXES viii

CHAPTER I INTRODUCTION 1

- **1.1 Issue Addressed in the Master Thesis** 1
- **1.2 Introduction of SCK•CEN** 2

CHAPTER II LITERATURE REVIEW 3

- **2.1 BR1 Fuel** 3
- **2.2 Belgian Geological Disposal** 4
- **2.3 General Overview of Portland Cement (OPC)** 4
- **2.4 Corrosion of Aluminum in High Alkalinity** 5
  - 2.4.1 In Alkaline Solution 6
  - 2.4.2 In Cement Matrix 6
- **2.5 $LiNO_3$ as Corrosion Inhibitor** 8
- **2.6 Electrochemical Impedance Spectroscopy** 10
- **2.7 Gas Chromatography** 12
- **2.8 Gas Pressure Measurement** 12

CHAPTER III EXPERIMENTAL METHODS 13

- **3.1 Materials** 13
- **3.2 EIS Corrosion Test** 13
- **3.3 Static Corrosion Tests** 16
- **3.4 Porosity measurement for cement** 18

CHAPTER IV RESULTS AND DISCUSSION 20

- **4.1 Mercury Intrusion Porosimetry** 20
- **4.2 EIS Measurements** 21

4.2.1 EIS Measurements 21
4.2.2 Determination of Charge Transfer Resistance (Rt) 26
4.2.3 EIS Tafel Slope Measurement 27
4.2.4 Corrosion Rate Calculation 27
4.2.5 EIS Measurement for Bare Aluminum in Saturated Limewater 32
4.3 Static Corrosion Test Results 35
4.3.1 Gas Chromatography 35
4.3.2 Pressure Measurement 36
4.4 EIS and static corrosion test comparison 37
CHAPTER V SOCIO-ECONOMIC CONTEXT 37
CHAPTER VI CONCLUSION 44
5.1 Summary 44
5.2 Future Improvements 44
BIBLIOGRAPHY 44
APPENDIX A EIS MEASUREMENT RESULTS xii
APPENDIX B CORROSION RATE CALCULATION xxii
APPENDIX C STERN-GEARY CONSTANT CALCULATION xxxiii
APPENDIX D CORROSION RATE xxxv
APPENDIX E PORE SIZE DISTRIBUTION IN DIFFERENT CEMENTS xxxvi
APPENDIX F CORROSION CALCULATION FROM STATIC CORROSION TEST xxxix

LIST OF TABLES

Table 1. Stern-Geary Constant (B) from Tafel Slope Measurements. 27
Table 2. Stern-Geary Constant (B) for Bare aluminum 33

LIST OF FIGURES

Figure 1. Schematic of ORNL X-10 reactor fuel. 3

Figure 2. Belgian Supercontainer design for vitrified high level waste 4

Figure 3. Corrosion rate of metals in dependence on the pH value. 6

Figure 4. Schematic representation of mechanism of aluminum corrosion in cements 7

Figure 5. Volume of hydrogen gas generated in Matsuo's experiment. 8

Figure 6. Effect of LiNO3 addition in Matsuo’s experiment. 8

Figure 7. $LiNO_3$ effect on aluminum corrosion after the land disposal. 9

Figure 8. Aluminum corrosion with the Li-Al preservation film removed 9

Figure 9. Sinusoidal current response in a linear system. 10

Figure 10. Example of a Nyquist plot. 11

Figure 11. Example of a Bode plot. 11

Figure 12. Simplified Randles Cell 12

Figure 13. Electrochemistry as an electrical circuit. 12

Figure 14. Aluminum plates and the welded aluminum wire coated with Teflon®. 14

Figure 15. Samples after taping. 14

Figure 16. Final configuration of the sample. 14

Figure 17. EIS test samples. 14

Figure 18. EIS corrosion test scheme. 15

Figure 19. EIS corrosion test. 15

Figure 20. Small Al plates for limewater immersion. 16

Figure 21. Al plates system for limewater immersion. 16

Figure 22. Bare Al plates immersion test. 16

Figure 23. Small Al plates for static test. 17

Figure 24. Static test samples. 17

Figure 25. Static Test containers. 17

Figure 26. Static Test Setup. 17

Figure 27. Gas Sampling System for the Gas Chromatography. 18

Figure 28. Samples for Mercury Intrusion Porosimetry. 19

Figure 29. Average pore radius comparison. 21

Figure 30. Total porosity comparison. 21

Figure 31. Crack in the sample 0.36_2. 22
Figure 32. Broken Wire in sample 0.8_4. 22
Figure 33. EIS Measurement of 0.36_1 (0.36 without crack). 24
Figure 34. EIS Measurement of 0.36_2 (0.36 with crack). 24
Figure 35. EIS Measurement of 0.36Li_1. 24
Figure 36. EIS Measurement of 0.8_3 (0.8 without broken wire). 24
Figure 37. EIS Measurement of 0.8_4 (0.8 with broken wire). 25
Figure 38. EIS Measurement of 0.8Li_1. 25
Figure 39. Amplitude and phase angle Bode plots of 0.36_1. 25
Figure 40. Amplitude and phase angle Bode plots of 0.36Li_1. 25
Figure 41. Circuit used to fit the EIS Result. 26
Figure 42. Circuit fitting the EIS results of sample 0.36_1_Day1. 26
Figure 43. Example of Tafel slope measurement result by Linear Polarization. 27
Figure 44. Corrosion rate comparison of 0.36 Samples. 29
Figure 45. Corrosion rate comparison of 0.36Li Samples. 29
Figure 46. Corrosion rate comparison of 0.8 Samples. 29
Figure 47. Corrosion rate comparison of 0.8Li Samples. 29
Figure 48. Corrosion rate comparison of Series 3. 30
Figure 49. Average corrosion rate. 32
Figure 50. Nyquist plot of bare aluminum. 33
Figure 51. Bode plot of bare aluminum. 33
Figure 52. Circuit used for Bare aluminum EIS fitting. 33
Figure 53. Corrosion rate of bare aluminum in $Ca(OH)_2$. 34
Figure 54. Bare aluminum plate corrosion. 34
Figure 55. Static corrosion test samples after the test. 35
Figure 56. Corrosion rate from GC measurement. 36
Figure 57. Corrosion rate from pressure measurement. 36
Figure 58. Corrosion rate comparison. 37
Figure 59. Jules Horowitz Reactor [20] 39
Figure 60. U.S. Nuclear research and test reactors 40
Figure 61. Speculative map of Mo-99 supply in 2020. 42
Figure 62. Speculative map of Mo-99 supply in 2030. 42

LIST OF ACRONYMS

AAS = Atomic Absorption Spectroscopy
AC = Alternating Current
BFS = Blast Furnace Slag
BR1 = Belgian Reactor 1
BR2 = Belgian Reactor 2
BR3 = Belgian Reactor 3
CEA = Commissariat À L'énergie Atomique Et Aux Énergies Alternatives
EIS = Electrochemical Impedance Spectroscopy
FIMA = Fissions Per Initial Metal Atom
GC = Gas Chromatography
HADES = High Activity Disposal Experimental Site
IAEA = International Atomic Energy Agency
ICP-MS = Inductively Coupled Plasma Mass Spectrometry
JHR = Jules Horowitz Reactor
LILW = Low And Intermediate Level Waste
LPR = Linear Polarization Resistance
MIP = Mercury Intrusion Porosimetry
MKP = Magnesium Phosphate Cement-based
MYRRHA = Multi-purpose hYbrid Research Reactor for High-tech Applications.
NAA = Neutron Activation Analysis
NTD = Neutron Transmutation Doped
OPC = Ordinary Portland Cement
ORNL = Oak Ridge National Lab
PWR = Pressurized Water Reactor
SEM = Scanning Electron Microscope
VITO = Vlaamse Instelling voor Technologisch Onderzoek
XRD = X-Ray Diffraction

LIST OF APPENDIXES

Appendix 1. EIS Measurement Result 0.3_1 xii
Appendix 2. EIS Measurement Result 0.3_2 xii
Appendix 3. EIS Measurement Result 0.3_3 xiii
Appendix 4. EIS Measurement Result 0.3_4 xiii
Appendix 5. EIS Measurement Result 0.3_5 xiv
Appendix 6.EIS Measurement Result 0.3Li_1 xiv
Appendix 7. EIS Measurement Result 0.3Li_2 xv
Appendix 8. EIS Measurement Result 0.3Li_3 xv
Appendix 9. EIS Measurement Result 0.3Li_4 xvi
Appendix 10. EIS Measurement Result 0.3Li_5 xvi
Appendix 11. EIS Measurement Result 0.8_1 xvii
Appendix 12. EIS Measurement Result 0.8_2 xvii
Appendix 13. EIS Measurement Result 0.8_3 xviii
Appendix 14. EIS Measurement Result 0.8_4 xviii
Appendix 15. EIS Measurement Result 0.8_5 xix
Appendix 16. EIS Measurement Result 0.8Li_1 xix
Appendix 17. EIS Measurement Result 0.8Li_2 xx
Appendix 18. EIS Measurement Result 0.8Li_3 xx
Appendix 19. EIS Measurement Result 0.8Li_4 xxi
Appendix 20. EIS Measurement Result 0.8Li_5 xxi
Appendix 21. Corrosion Rate Calculation for 0.3_1 xxii
Appendix 22. Corrosion Rate Calculation for 0.8_1 xxii
Appendix 23. Corrosion Rate Calculation for 0.8Li_1 xxiii
Appendix 24. Corrosion Rate Calculation for 0.3Li_1 xxiii
Appendix 25. Corrosion Rate Calculation for 0.3_2 xxiv
Appendix 26. Corrosion Rate Calculation for 0.8_2 xxiv
Appendix 27. Corrosion Rate Calculation for 0.8Li_2 xxv
Appendix 28. Corrosion Rate Calculation for 0.3Li_2 xxv
Appendix 29. Corrosion Rate Calculation for 0.3_3 xxvi
Appendix 30. Corrosion Rate Calculation for 0.8_3 xxvi

Appendix 31. Corrosion Rate Calculation for 0.8LI_3 xxvii
Appendix 32. Corrosion Rate Calculation for 0.3Li_3 xxvii
Appendix 33. Corrosion Rate Calculation for 0.3_4 xxviii
Appendix 34. Corrosion Rate Calculation for 0.8_4 xxviii
Appendix 35. Corrosion Rate Calculation for 0.8Li_4 xxix
Appendix 36. Corrosion Rate Calculation for 0.3Li_4 xxix
Appendix 37. Corrosion Rate Calculation for 0.3_5 xxx
Appendix 38. Corrosion Rate Calculation for 0.8_5 xxx
Appendix 39. Corrosion Rate Calculation for 0.8Li_5 xxxi
Appendix 40. Corrosion Rate Calculation for 0.3Li_5 xxxi
Appendix 41. Total Measurement Period Corrosion Rate Calculation xxxii
Appendix 42. Steady state Period Corrosion Rate Calculation xxxii
Appendix 43. Stern-Geary Constant Calculation for Cemented Samples xxxiii
Appendix 44. Stern-Geary Constant Calculation for Bare aluminum Samples........ xxxiv
Appendix 45. Corrosion rate comparison of Series 1 xxxv
Appendix 46. Corrosion rate comparison of Series 2 xxxv
Appendix 47. Corrosion rate comparison of Series 4 xxxv
Appendix 48. Corrosion rate comparison of Series 5 xxxv
Appendix 49. Pore Size Distribution for 0.36........ xxxvi
Appendix 50. Pore Size Distribution for 0.36Li xxxvi
Appendix 51. Pore Size Distribution for 0.8........ xxxvii
Appendix 52. Pore Size Distribution for 0.8Li xxxvii
Appendix 53. Summary of Mercury Porosimetry........ xxxviii
Appendix 54. Example of Corrosion rate calculation by GC xl
Appendix 55. Example of Corrosion rate calculation by gas pressure measurement........ xli
Appendix 56. Corrosion Rate from Static Corrosion Test........ xli

CHAPTER I

INTRODUCTION

1.1 Issue Addressed in the Master Thesis

Since the discovery of the atom in 1897, humankind has been fascinated by the idea of harnessing the power of the atom. The discovery of the atom has been the foundation of the advancement of human into the era of nuclear technology. Currently, nuclear technology has integrated with the way human lives such as to produce energy, to produce medical isotopes, to create advanced and better crops in farming technology, etc. One of the applications of nuclear technology is the research reactor. Research reactor technology is not used to produce energy but instead it is used to test materials under irradiation conditions and also to be able to produce medical isotopes. One example of a research reactor is the BR1 (i.e. the Belgian Reactor 1) at SCK•CEN which is located in Mol, Belgium.

BR1 is the first Belgian reactor. It was able to maintain the chain reaction inside the reactor for the first time on 11th May 1956 [1]. After the start-up period, BR1 was mainly used for research in reactor and neutron physics. Until after the start-up of BR2 in 1964, BR1 was also used for the production of radioisotopes for medical applications. The reactor worked continuously, 24 hours a day, 7 days a week. The BR1 is currently used for neutrography, calibration and validation of radiation measurement instruments, neutron activation analysis (NAA), training and education especially on nuclear reactor theory for students, and production of Neutron Transmutation Doped (NTD) Silicon.

The fuel inside BR1 is composed of natural unalloyed metallic uranium, coated with an aluminosilicate alloy bonding layer and an $U(Al,Si)_3$ anti-diffusion layer, and encapsulated in an aluminum cladding [2]. There is a need for long-term management of this fuel, which will eventually become waste. One of the solutions for the management of this waste is geological disposal. A direct embedding of the waste in a cement-based material could be considered as a technique for geological disposal.

Previous research and experiments have shown that there are several phenomena that might be harmful to the intactness of the nuclear waste caused by cement embedding. In contact with the highly alkaline cement pore water, high corrosion rates are observed for aluminum and uranium to form e.g. aluminum hydroxide, uranium oxides and hydrides, and hydrogen gas. These products can then lead to stresses in the encapsulated matrix, damaging this matrix. The damage of the matrix might cause a leak of radioactive material into the environment which will cause unwanted and harmful effects. That is why a research must be done to limit the corrosion rates and prevent the damage of the nuclear waste.

The main topic of this research is the interaction between the aluminum with the cement. Use of low porosity cement and use of corrosion inhibitor $LiNO_3$ is studied in this research as an attempt to reduce the corrosion rates of aluminum. The hypothesis is that if a cement-based material, possessing a low porosity, is used, the diffusion of water through the material will be limited, and due to this mass transport limitation, the corrosion rate should drastically decrease. The use of $LiNO_3$ as corrosion inhibitor should induce a protective layer in the aluminum to protect the aluminum from high rate corrosions. The study used Electrochemical Impedance Spectroscopy (EIS) and Gas Chromatography (GC) to measure the corrosion rate of the aluminum.

1.2 Introduction of SCK•CEN

SCK•CEN (Dutch: Studiecentrum voor Kernenergie; French: Centre d'Étude de l'énergie Nucléaire) is a research center located in Mol (Belgium) dealing with peaceful applications of radioactivity [3]. It performs forward-looking research and develops sustainable technology, organizes training courses, offers specialist services and acts as a consultancy. It is also one of the largest research institutions in Belgium, employing more than 750 employees.

The three main research topics of SCK•CEN are:

- the safety of nuclear installations
- the well-considered management of radioactive waste
- human and environmental protection against ionizing radiation.

The current focus research activities for SCK•CEN are:

- protection of humans and environment against radioactivity
- disposal of radioactive waste
- a new research reactor: MYRRHA
- innovative reactors and nuclear fuels
- nuclear fusion
- dismantling of nuclear installations
- astronautics.

SCK•CEN comprises 3 scientific institutes:

- Institute for nuclear materials science
- Institute for advanced nuclear systems
- Institute for environment, health, and safety.

Research infrastructures available in SCK•CEN are:

- MYRRHA: in development → Multifunctional research infrastructure
- VENUS reactor: GUINEVERE project → Zero power reactor
- Reactor BR1 → Low Power Graphite Reactor
- Reactor BR2 → Very high flux research reactor
- Reactor BR3: in the process of decommissioning → PWR power plant decommissioning
- HADES: underground laboratory → underground high level waste disposal research lab
- Nuclear and non-nuclear laboratories

CHAPTER II

LITERATURE REVIEW

2.1 BR1 Fuel

The Belgian Reactor 1 (BR1) is the Belgian research reactor that is mainly used as a neutron source for reactor physics experiments, neutron activation analysis, and calibration of nuclear detectors and instruments. The reactor core consists of a graphite matrix, serving as moderator, in which the fuel rods are loaded in horizontal channels. These rods consist of a natural uranium (0.7% $^{235}U/U_{tot}$) cylindrical bar in an aluminum cladding [2]. The reactor is operational for 3 days a week at 700 kW for a maximum of 8 hours per day. BR1 is cooled with forced air convection using a fan and it is kept well below 200 °C. After more than 50 years, the average fuel element burn-up is calculated to be only 0.07% FIMA (fissions per initial metal atom).

The BR1 fuel is composed of natural unalloyed metallic uranium, coated with an aluminosilicate alloy (AlSi) bonding layer and an $U(Al,Si)_3$ anti-diffusion layer, and encapsulated in an aluminum cladding [2]. The bonding layer needs to ensure proper heat transfer and the anti-diffusion barrier is applied to limit the interaction between the uranium and the aluminum cladding. The fuel is similar to that used in the Oak Ridge National Laboratory (ORNL) graphite reactor X-10, this fuel schematics can be seen in Figure 1.

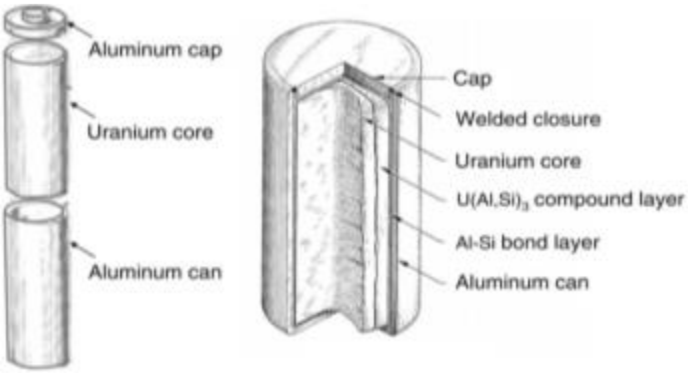

Figure 1. Schematic of ORNL X-10 reactor fuel *[2]*.

The aluminum can was deep drawn from aluminum alloy 1100 which has the following composition: Al: 99.0–99.95%, Cu: 0.05–0.20%, Fe: 0.95% max, Mn: 0.05% max, Si: 0.95% max, Zn: 0.1% max, Residuals: 0.15% max. The uranium slugs were machined from rods, degassed and heat treated to provide a randomly oriented grain structure. The aluminum can was then dipped into Al-Si molten bath to create the bonding layer while the uranium slugs were coated with $U(Al,Si)_3$ anti-diffusion layer by dipping the heated uranium slug in a molten aluminum-silicon alloy of eutectic composition. The fuel rod is thus composed of an uranium slug coated with an $U(Al,Si)_3$ anti-diffusion layer and tightly bonded to the Al can and cap through an AlSi bonding layer.

There are several routes to dispose the BR1 fuel. The routes are:

- Direct emplacement of the fuel capsules in a cementitious matrix
- Mechanical removal of the Al cladding (the AlSi and $U(Al,Si)_3$ layers, followed by the encapsulation of the U core in a cementitious matrix

- Pre-oxidation of the metallic uranium
- Reprocessing of the spent fuel

This research focusses on the first route, which is direct emplacement in a cementitious matrix.

2.2 Belgian Geological Disposal

In Belgium, radioactive waste is classified in three categories: A, B, and C. Category A is the short-lived (half-life less than 30 years) low and intermediate level waste (LILW), category B is the long-lived LILW, and category C is the high level waste, comprising both vitrified waste and spent fuel [4]. The ultimate fate of B and C waste is final storage, by means of geological disposal, in a poorly indurated clay placed in supercontainers, involving the use of a cement buffer. The supercontainer design can be seen in Figure 2 below.

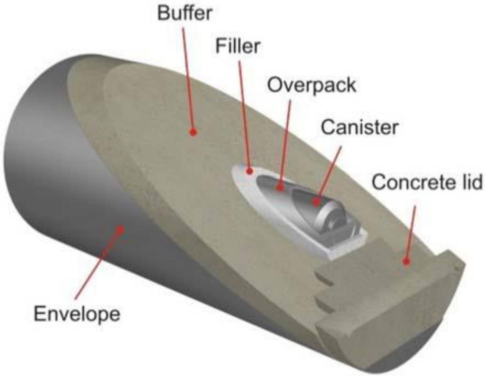

Figure 2. Belgian Supercontainer design for vitrified high level waste.

2.3 General Overview of Portland Cement (OPC)

Cement is a hydraulic mineral binding material. Blended with water, the pulverous cement can generate the plastic paste which will turn into hard cement block and bind granulated (or block) materials together after a series of physical and chemical effects [5]. The hardening of cement paste will happen not only in air but also in water. It is also known to be able to maintain and increase its strength. Ordinary Portland cement (OPC) is one of the most common types of cement, and today it is the most commonly used construction material.

The names and contents of the main mineral compounds in Portland cement clinker are as follows [5]:

- Tricalcium Silicate ($3CaO\text{-}SiO_2$, abbreviated as C_3S), accounting for 37%-60%;
- Dicalcium Silicate ($2CaO*SiO_2$ abbreviated as C_2S), accounting for 15%-37%;
- Tricalcium Aluminate ($3CaO*A1_2O_3$, abbreviated as C_3A), accounting for 7%-15%;
- Tetracalcium Aluminoferrite ($4CaO*Al_2O_3*Fe_2O_3$, abbreviated as C_4AF) accounting for 10%-18%.

In addition to these four major minerals, there are a small amount of free calcium oxide, gypsum ($CaSO_4.2H_2O$), magnesium oxide, and alkali in cement. It is clearly prescribed in the national standards that the total amount should not be more than 10% [5].

When water is added, the cement particles are surrounded by water, causing the surface of the mineral granules in the clinker to react with the water immediately, which results in the generation of a series of new compounds and the release of a certain heat. Portland cement reacts with water and generates colloidal hydrated products mainly containing calcium silicate hydrate, calcium ferrite hydrate gel, calcium aluminate hydrate, and the crystals of calcium sulfate hydrate, this is the hydration process. In the complete-hydrated cement paste, the calcium silicate hydrate accounts for about 50%, and the calcium hydroxide accounts for about 25%. The generated colloidal hydrated products increase continuously and form a loose mesh structure by contacting with some points which make the paste lose mobility and plasticity, known as setting of cement. Then, the calcium silicate hydrate gel, calcium hydroxide, crystals of calcium sulfate hydrate, and other kinds of hydrated products continue to increase and they contact with and adhere to each other, and then a closer mesh crystal structure is established, which will keep be packed along the time and begin to render the cement with strength, this phase is known as "hardening" of the cement. After the hardening process, the cement paste becomes a heterogeneous structure consisting of crystals, gel, unhydrated clinker particles, free water, and pores in various sizes. It is well known that there is a high alkalinity in the pore solution of conventional OPC materials ($pH > 12.6$) [6].

The water-to-cement (w/c) ratio also plays a significant part of cement characteristics. The increase of the water content will enhance the amount of capillary porosities, lower the strength of cement paste, and extend the setting time [5]. Water dynamics is modified by the evolution in maturity and w/c ratio [7]. Penetration of limewater through the cement in this experiment will be affected by the w/c ratio because of the difference of water dynamics in the cement.

OPC is also one of the most widely used materials for conditioning radioactive wastes because it is inexpensive, it can be easily supplied, and it can exhibit high stability over time after hydration [8]. However, OPC possesses a high pH pore water solution. The corrosion of aluminum in OPC, and the production of H_2, could be high, possibly leading to cracks in the cement matrix because of the increase of pressure in the container.

2.4 Corrosion of Aluminum in High Alkalinity

Aluminum is the third most abundant element in the Earth's crust. Aluminum has been used as cladding material for the nuclear fuels and targets because it has a low thermal neutron absorption cross-section. Usually Material Testing reactors, such as the BR1, use aluminum as the cladding because the reactor doesn't operate in high temperature.

Aluminum generally has a good corrosion behavior caused by the development of passivating oxide and hydroxide coatings which are largely insoluble in the pH range between 4 and 9. Aluminum alloys have good resistivity against corrosion in nearly neutral to weakly acid aqueous media and in humid air, thus in atmospheric corrosion conditions. In all other cases, the protective effect of the coating is lost as a result of its disintegration in more strongly acid and alkaline media because aluminum is an amphoteric metal. The corrosion rate of aluminum as a function of pH of the electrolyte can be seen in Figure 3 [9].

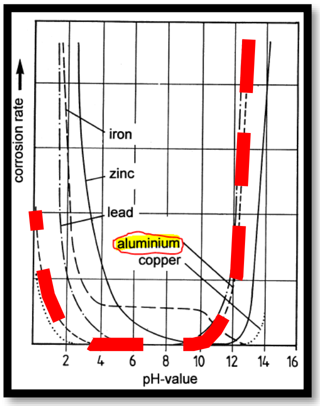

Figure 3. Corrosion rate of metals in dependence on the pH value *[9]*.

2.4.1 In Alkaline Solution

When metallic aluminum is immersed in alkaline solutions, aluminum is oxidized following the anodic reaction presented in Equation (1) [4]:

$$Al^\circ \rightarrow Al^{3+} + 3\ e^- \tag{1}$$

Then, aluminum cations react with hydroxide ions to form aluminum hydroxides according to Equation (2):

$$Al^{3+} + 3\ OH^- \rightarrow Al(OH)_3 \tag{2}$$

However, in alkaline condition, this hydroxide layer dissolves to form soluble aluminate ions (Equation (3)):

$$Al(OH)_3 + OH^- \rightarrow Al(OH)_4^- \ (\text{or } AlO^{2-} + 2\ H_2O) \tag{3}$$

In oxic conditions, the anodic reaction is counterbalanced by the reduction of oxygen (Equation (4)):

$$O_2 + 2\ H_2O + 4\ e^- \rightarrow 4\ OH^- \tag{4}$$

However in anoxic conditions, to counterbalance the anodic reaction, the reduction of water occurs as the cathodic reaction, which takes place at the aluminum surface [4]. (Equation (5):

$$2\ H_2O + 2\ e^- \rightarrow 2\ OH^- + H_2 \tag{5}$$

Finally, Equation (6) gives the overall reaction of the aluminum dissolution in alkaline solution under anaerobic conditions:

$$Al^\circ + OH^- + 3\ H_2O \rightarrow Al(OH)_4^- + 3/2\ H_2 \tag{6}$$

2.4.2 In Cement Matrix

The corrosion rate of metallic aluminum in Lime solution can reach 1.0817 mm/y when immersed in Lime solution [10]. However, for aluminum embedded in cement matrix, it will have a fairly high rate of corrosion in the beginning. It can fluctuate between 1600 to 22000 µm/yr [4]. After a few tens of days the corrosion rate will decrease very rapidly to reach values of 16 to 800 µm/yr. Some studies also show that with an increase of time the corrosion rate reaches values of 0.1 to 0.5 µm/yr after less than 2 years [4]. Another study shows that aluminum alloy 3003 in an Ordinary Portland Cement (OPC) matrix has a corrosion rate of 1000 µm/yr during the first hours, the rate quickly dropped to reach 50 µm/yr after 6 months, and finally the average of the corrosion rate during the 27 years of measurement was 1.3 µm/yr. So, the corrosion of aluminum in cement matrix has a very high initial rate and decreases to much lower values in time. This decrease can be attributed to the depletion of water at the surface of aluminum or by passivation [4].

Based on previous studies, it is known that when aluminum is embedded in cement, the aluminum corrodes to produce a porous zone into which white corrosion products grow at the interface between the metal and the cement. The corrosion products accumulate after ~24 h hydration reaching a thickness of 1 – 2 mm after 28 days of hydration [11]. Aluminum hydroxide ($Al(OH)_3$) and strätlingite ($2CaO.Al_2O_3.SiO_2.8H_2O$) were identified as the major components of the corrosion products. After 360 days of hydration, it was observed that the aluminum hydroxide was predominant in form of gibbsite while strätlingite was not identified anymore [11].

The corrosion mechanism of aluminum in cement can be described in three stages, which is shown in Figure 4 [11]. The alumina layer on the aluminum surface normally protects the metal from further reaction with moisture, but in the alkaline pore solution of cement the OH^- ions attack and dissolve this layer which will produce soluble hydroxyl aluminate ions (Equation 3) and expose the metal surface. The bare metal surface will then be attacked by hydroxide ions and water which produces more soluble hydroxyl aluminate ions and hydrogen gas, this reaction can be seen in Equation 6. The hydroxyl aluminate ions then react with silicates and possibly calcium hydroxide from the hydrating cement to form strätlingite. Along with time and as the cement hardens, the OH^- is depleted from the vicinity of the aluminum due to reduced diffusion rates. The hydroxyl aluminate will then decompose leading to the release of OH^-, which can be further consumed through corrosion and precipitation of an aluminum hydroxide phase.

The main concerns with corrosion of aluminum in a cement matrix are the hydrogen gas evolution and expansion of the waste as result of continuous corrosion. The cement matrix of aluminum samples that were embedded in OPC have cracked after ~90 days [11]. It is generally accepted that lowering the pH of the cement system and/or reducing available free water will reduce the reaction of aluminum in the cement matrix [12]. From other studies it is known that reduction of aluminum corrosion has been seen in systems using 9:1 Blast Furnace Slag (BFS)-OPC system [11], cement of excess sulphate [12], or magnesium phosphate cement-based (MKP) mortar [8] instead of using OPC matrix to embed the aluminum.

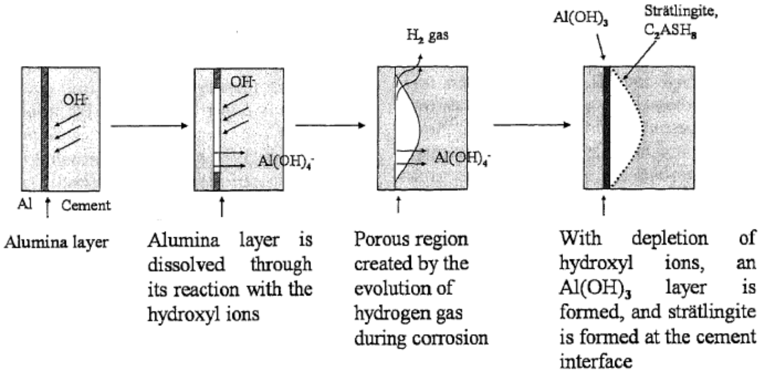

Figure 4. Schematic representation of mechanism of aluminum corrosion in cements *[11]*.

2.5 $LiNO_3$ as Corrosion Inhibitor

Corrosion inhibitors are chemical compounds that can be added to a system to decrease the corrosion rate of a material inside a certain system. Previous studies have shown that $LiNO_3$ is one of the best solutions to be used as corrosion inhibitor for aluminum embedded in cement. $LiNO_3$ addition to cement is effective to prevent H_2 gas generation by forming an insoluble film on aluminum to prevent the corrosion of aluminum in a cement matrix [13].

Addition of $LiNO_3$ reduces the generated H_2 gas to less than 10% of the amount of gas generated in samples without $LiNO_3$ before cement paste starts solidifying. After the cement paste starts to solidify, the H_2 is still produced in samples without $LiNO_3$ while there is no increase in samples with $LiNO_3$, as can be seen in Figure 5 [13]. It is also observed that addition of 3 wt.% of $LiNO_3$ to the samples was able to reduce the rate of H_2 gas generation regardless of the amount of aluminum. It has been shown that $LiNO_3$ can be effective to prevent aluminum corrosion in cement such as can be seen in Figure 6.

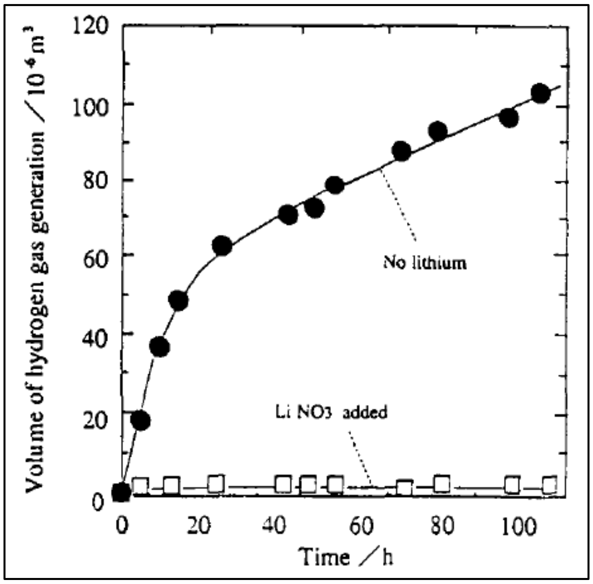

Figure 5. Volume of hydrogen gas generated in Matsuo's experiment. [12]

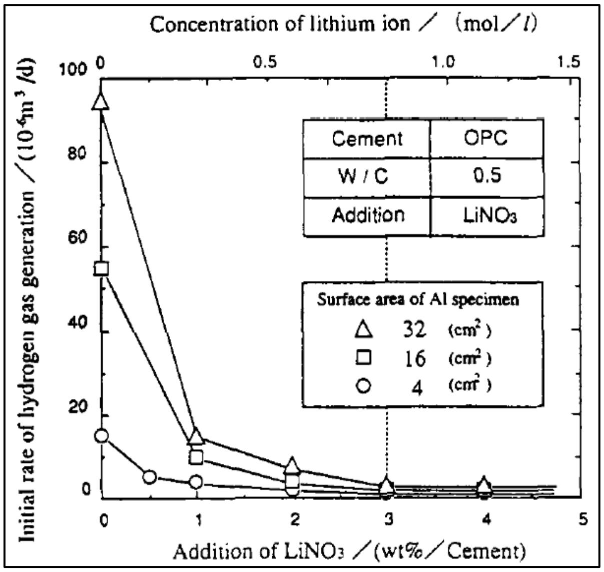

Figure 6. Effect of $LiNO_3$ addition in Matsuo's experiment. [13]

By Scanning Electron Microscopy (SEM) analysis, Matsuo et al. *[13]* also show that a thin layer with a thickness of 5 – 20 µm is homogeneously covering the aluminum surface. X-ray diffraction (XRD) indicates that the thin layer is made of Li-Al double salt ($LiH(AlO_2)_2.5H_2O$), bayerite ($Al_2O_3.3H_2O$), and Al_2O_3. Li-Al double salt settled on the layer of bayerite and acts as a film to prevent the layers of bayerite and Al_2O_3 from dissolution into the alkaline solvent, which prevents the oxidation and H_2 gas generation of the aluminum in the cement matrix.

However, the protective effect of the Li-Al may fail. Three possibilities can describe the failure of the protective effect of the Li-Al film [14]:

1. Underground water penetrates the concrete wall and reaches the waste, this will cause the dissolution of $LiNO_3$ and lower the concentration of Li^+ in the waste. The lower concentration of Li^+ will cause the dissolution of the Li-Al film caused by the shift of equilibrium to the left in the reaction, which can be seen in Equation 7.

$$Li^+ + 2\ Al(OH)_4^- + 2\ H_2O \leftrightarrow LiH(AlO_2)_2.\ 5H_2O + OH^- \qquad (7)$$

2. If the waste includes components with complex shapes, it is possible that the Li-Al preservation film is not formed on some parts of the metal surface during cement solidification.
3. Natural processes such as earthquake shocks might degrade the Li-Al preservation film in some parts of the waste.

Matsuo's experiment [14] also shows that addition of $LiNO_3$ has additional effects to reduce the corrosion rate of aluminum after land disposal:

- When the Li^+ concentration is lowered by underground water penetration causing dissolution of the Li-Al film and generation of H_2 gas, there is also dissolution of Na_2O and K_2O from the cement. This will decrease the pore water pH from ~13 to ~12.3, leading to the reduction of the aluminum corrosion to 10% of the corrosion amount without initial addition of $LiNO_3$. The phenomena can be seen in Figure 7.
- In case of complex shapes or earthquake, where there is a loss of protective effect of the Li-Al film, $LiNO_3$ included in the waste will form Li-Al preservation film when the underground water penetrates the cement. $LiNO_3$ will be dissolved in the water and react with the exposed aluminum to produce Li-Al film which will prevent H_2 gas generation. This phenomenon can be seen in Figure 8 where in a solution with the same pH of 12.9, the one with Li corroded less.

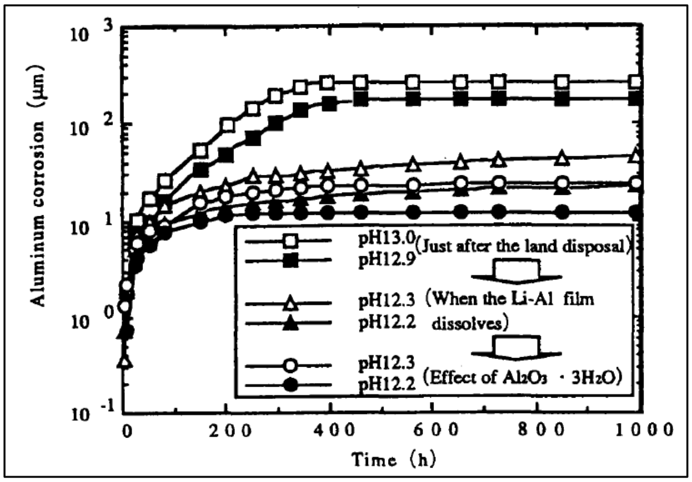

Figure 7. $LiNO_3$ effect on aluminum corrosion after the land disposal *[14]*.

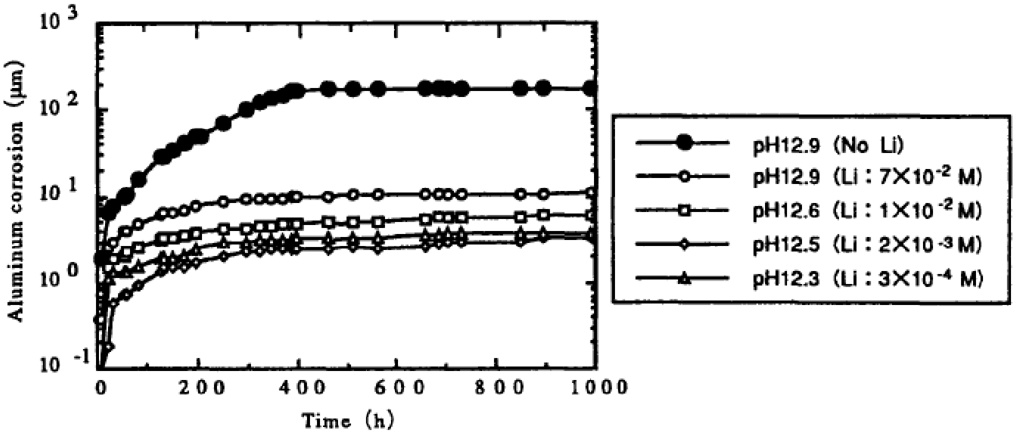

Figure 8. Aluminum corrosion with the Li-Al preservation film removed *[14]*.

2.6 Electrochemical Impedance Spectroscopy

The electrochemical impedance spectroscopy (EIS) is a tool that can be used for corrosion research. EIS measurement is done by applying an alternating current (AC) into a system and measure the response. EIS is a useful method because it is a non-destructive test.

First step for EIS is to apply AC of fixed frequencies. An AC potential perturbation is applied over a range of frequencies and the resulting current response of the system is measured [15]. The impedance of the system is then calculated by analyzing the response signal at each frequency. The result can be represented graphically in a Nyquist plot or Bode plots. The EIS results need to be modelled and fitted with an appropriate equivalent electrical circuit that represents the electrochemical processes in the system. Charge transfer resistance can be calculated by the fitting procedure, which can then be used to calculate the corrosion current.

EIS is done by applying a small excitation signal (1 to 10 mV) so the system's response is pseudo-linear [16]. In a pseudo-linear system, the current response to a sinusoidal potential will also be sinusoid at the same frequency but shifted in phase (see Figure 9) [16]. Using Ohm's law and Euler's relationship, it is possible to represent the impedance as a complex number such can be seen in Equation 8 with E being the excitation signal potential, I is the current response, Z is the impedance, ω is the radial frequency, and Φ is the phase shift.

$$Z\ (w) = \frac{E}{I} = Z_0 \exp(j\Phi) = \ Z_0\ (\cos\Phi + \mathrm{j}\sin\Phi) \tag{8}$$

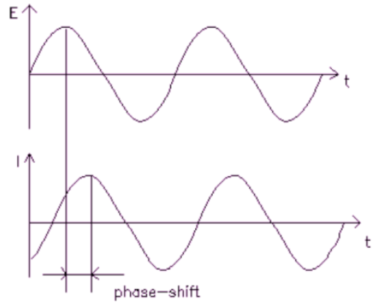

Figure 9. Sinusoidal current response in a linear system.

Equation 8 shows that the impedance is composed of a real and an imaginary part. The real part is plotted on the X-axis and the imaginary part is plotted on the Y-axis to create a "Nyquist plot" [16]. An example of a Nyquist plot can be seen in Figure 10. Nyquist plot has a major weakness, because when you look at any data point on the plot one cannot tell what frequency was used to record that point, although usually the data in the left side is obtained from high frequency while the data on the right side is from the low frequency. The semicircle in the plot represents a single time constant, where the diameter of the semicircle is equal to the polarization resistance [16].

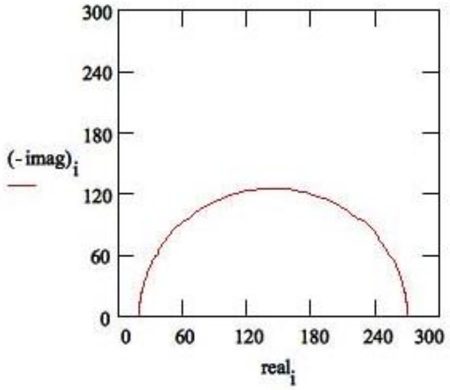

Figure 10. Example of a Nyquist plot.

Another popular way to present the EIS results is by using Bode Plots. An example of Bode plots can be seen in Figure 11. The Bode Plots can be separated into a magnitude plot and a phase plot. In a Bode Plot, the logarithm of the frequency is plotted on the X-axis and both the logarithm of the absolute value of the impedance and the phase shift on the Y-axis.

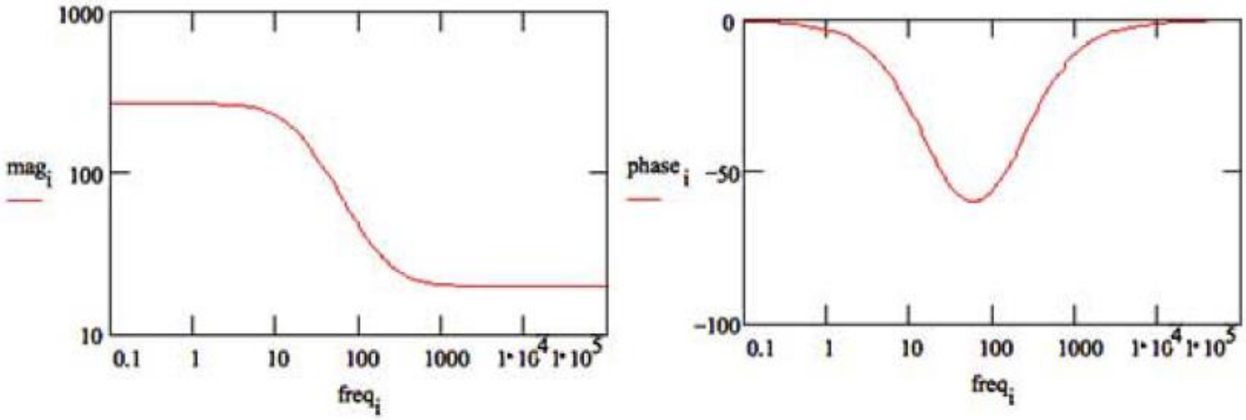

Figure 11. Example of Bode plots.

As mentioned before, the EIS needs a fitting procedure to a cell model. One of the most common cell model is the Simplified Randles Cell like the one in Figure 12 [16]. The Simplified Randles Cell can model a system with a solution resistance (Rs), a double layer capacitor (Cdl), and a charge transfer (polarization resistance, Rt or Rp or Rct), such as the one in Figure 13. The Nyquist plot for a Simplified Randles cell is always a semicircle such as the one before in Figure 10. The solution resistance can be found by reading the real axis value at the high frequency intercept, while the real axis value at the low frequency intercept shows the sum of polarization resistance and the solution resistance. The diameter of the semicircle is an approximation to the polarization resistance [16]. From Figure 10 it can be seen that Rs = 20 Ω and Rt = 230 Ω.

The Rt obtained from the measurement can then be used to calculate the corrosion current density (i_{CORR}, $\mu a.cm^{-2}$), using the Stern-Geary Equation (Equation 9) [15], while the Stern-Geary constant (B) and the anodic and cathodic Tafel slopes (ba and bc) are obtained via the Tafel slope measurement. The corrosion rate (ν_{CORR}, $\mu m.yr^{-1}$) can be calculated using i_{CORR} by using Equation 10 with ρ as the metal density (g.cm^{-3}, ρ_{Al} = 2.7 g.cm^{3}) and EW as equivalent weight . EW is calculated by dividing the atomic weight of an element with the valence of the metal, in this case the atomic weight of Al is 27 and the valence is 3 (EW_{Al} = 27/3 = 9).

$$\mathrm{i}_{CORR} = \frac{1}{2.30\ x\ Rt}\ x\ \left(\frac{\mathrm{ba\ x\ bc}}{\mathrm{ba+\ bc}}\right) = \frac{B}{Rt} \qquad (9)$$

$$v_{CORR} = 3.27\ x\ \frac{i_{CORR}}{\rho}\ x\ EW \qquad (10)$$

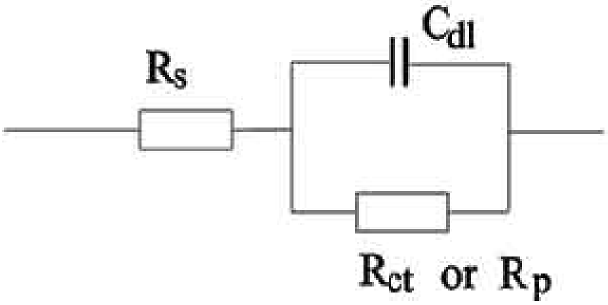

Figure 12. Simplified Randles Cell.

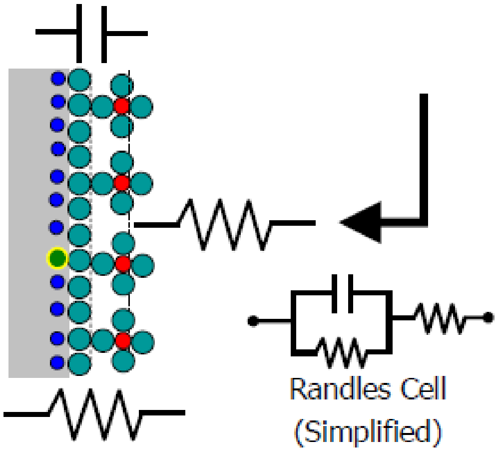

Figure 13. Electrochemistry as an electrochemical circuit.

2.7 Gas Chromatography

Gas Chromatography (GC) is a method that can be used to measure the amount of H_2 gas produced during the corrosion of aluminum embedded in a cement matrix. This technique requires an inert gas stream to flow the sample over a sealed cell [15]. Hydrogen from the sample is then entrained in the inert gas, which is then carried to and quantified by a gas chromatograph.

2.8 Gas Pressure Measurement

The pressure of the gas produced from the corrosion is measured using a barometer. Using the ideal gas law (Equation 11) the moles of gas produced can be calculated. In Equation 11, p is the measured pressure, v is the volume of the head space container used in the experiment, R is the gas constant (R = 8.3145 J/mol·K), T is is the temperature inside the glove box of the experiment (T = 295 K), and n is the moles of the H_2 gas.

$$p\ v\ = n\ R\ T \qquad (11)$$

CHAPTER III

EXPERIMENTAL METHODS

3.1 Materials

3.1.1 Aluminum

The aluminum used in the experiment is aluminum with 99% Al purity. There are two dimensions of Al plates used in this research. Larger Al plates welded to Al wire and taped for the immersion test, while smaller Al plates were used for the static test. Detailed dimension of the Al plates will be explained in the section below.

3.1.2 Cement

The cement used in this research is Ordinary Portland Cement, which was conditioned in 4 different ways:

- 0.36 water-to-cement ratio;
- 0.36 water-to-cement ratio with 3wt.% $LiNO_3$;
- 0.8 water-to-cement ratio;
- 0.8 water-to-cement ratio with 3wt.% $LiNO_3$.

The 0.36 water-to-cement ratio was chosen because it is the lowest water-to-cement ratio commonly used in cement, while 0.8 is commonly the highest water-to-cement ratio. The higher the water-to-cement ratio results in higher workability of the cement but lower the strength of the cement, while lower water-to-cement ratio means less excess water in the cement, which should decrease the corrosion of aluminum [12]. The water-to-cement ratio will also influence the diameter pore size of the cement, which will affect the mass transport of the solution surrounding the sample to the aluminum inside the cement. The lower water-to-cement ratio should produce smaller diameter of pores which means lower mass transport and lower corrosion of the embedded aluminum. $LiNO_3$ (anhydrous, 99.98% (metal basis) ; Thermo Fisher (Kandel) GmbH) was also added to see the effect of corrosion inhibition [13].

In this experiment, the embedding process was done inside the glove box to minimize the amount of oxygen. The experiments were prepared and conducted in anoxic conditions to mimic the conditions of the anaerobic phase of the waste disposal.

3.2 EIS Corrosion Test

First, aluminum wires were welded on the aluminum plates for electrical connection. The wires were shielded with shrinkage Teflon tubes to isolate the wires from the test solution. This is illustrated in Figure 14. To control the exposed surface, the plates were covered using tape to create a circular surface with a diameter of 1.8 cm, leaving an exposed surface of 2.54 cm^2 (Figure 15). The plates were then connected by Teflon® screws to control the distance between the two aluminum plates to 0.55 cm (Figure 16). The plates were finally rinsed with water and cleaned using ethanol to remove any smudge before doing the test.

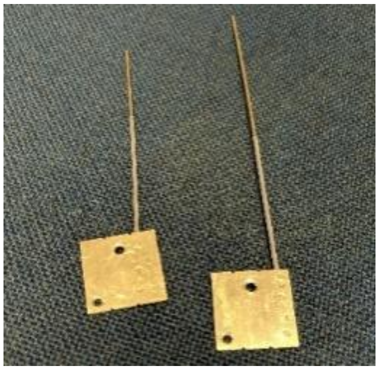

Figure 14. Aluminum plates and the welded aluminum wire coated with Teflon®.

Figure 15. Samples after taping.

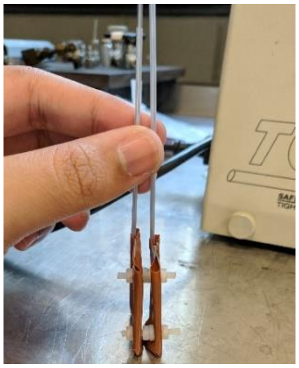

Figure 16. Final configuration of the sample.

After the sample preparation was done, the samples and the cement were introduced inside a glove box. The cementation and embedding process were all done inside a glove box to avoid as much as possible the presence of oxygen in the cement to perform the corrosion tests in anaerobic conditions. The aluminum plates were embedded into 4x4x4cm cube of cement. Five samples were prepared for each type of cement (see Section 3.1.2 for the type of cement) as can be seen in Figure 17. The samples were then immersed into saturated $Ca(OH)_2$ (1.6 g/l) limewater. The water used to make this solution was deoxygenated milliQ water. The lids for the samples were then closed to minimize the evaporation. The system of the EIS measurement can be seen in Figure 18 and Figure 19.

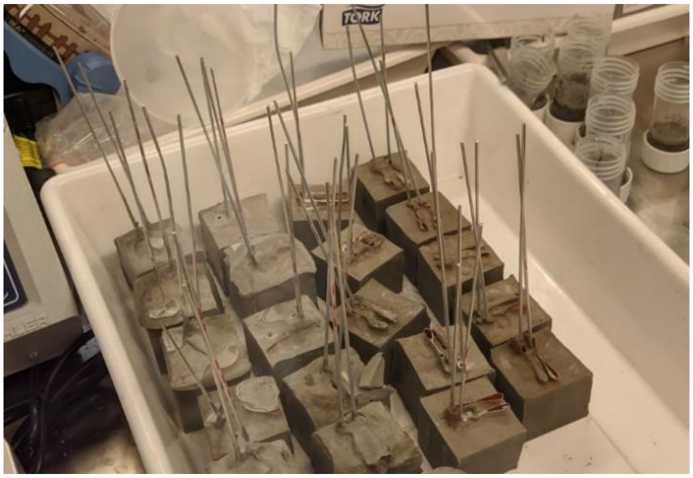

Figure 17. EIS test samples.

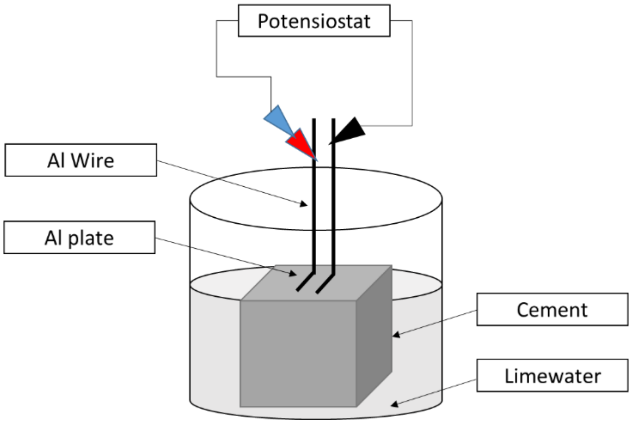

Figure 18. EIS corrosion test scheme.

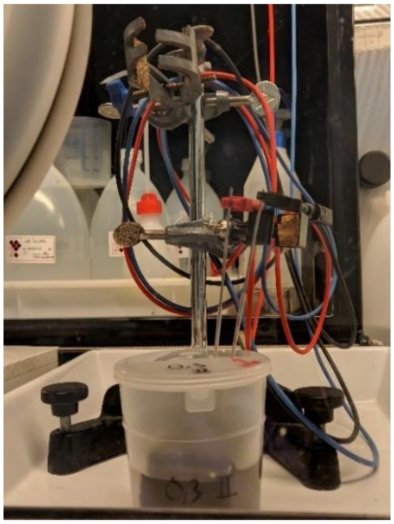

Figure 19. EIS corrosion test.

The EIS measurements were carried out weekly for each sample. The measurements were conducted using an excitation potential of 10 mV (peak-to-peak) over the frequency range from 100 kHz to 10 mHz, with the impedance being measured at ten frequencies per decade. A few measurements were also done in the range of 1 MHz – 1 mHz. . The quality of the obtained EIS data was checked experimentally and theoretically, with the latter being performed using the Kramers-Kronig transformations. The data were checked experimentally by stepping the frequencies from high-to-low and then immediately back from low-to-high, with the impedance being measured at each step, to ascertain that the same values were obtained at equivalent frequencies in the two directions. Linear polarization measurements were done after EIS to obtain the value of the Tafel slopes, which are necessary to calculate the corrosion rate (see Section 4.2.3).

The results from the EIS measurements were then treated using ZView software. In ZViews the EIS results will be fitted to an electrical circuit. The fitting provides the value for the polarization resistance (Rt). The Rt is then used to calculate the corrosion rate using Equation 9 and Equation 10 in Section 2.6.

EIS corrosion tests were also done by immersing bare aluminum plates into saturated limewater without embedding them into cement. Small Al plates were used and taped in this test. After taping, the surface area of the samples was 3.5 cm^2 (Figure 20). The Al plates were then connected using Teflon® screws, as can be seen in Figure 21. The EIS corrosion test for the bare Al plates is illustrated in Figure 22.

Figure 20. Small Al plates for limewater immersion.

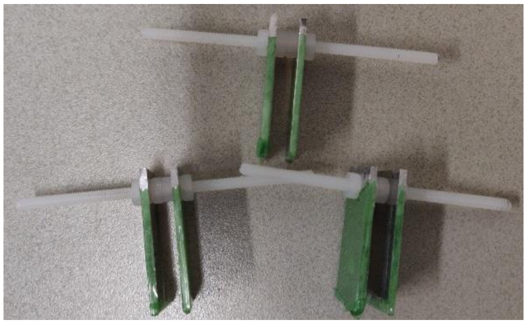

Figure 21. Al plates system for limewater immersion.

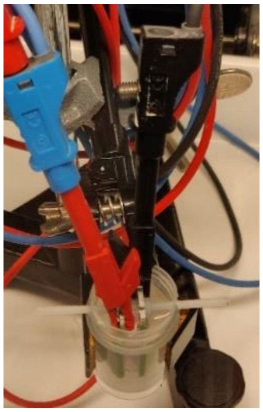

Figure 22. Bare Al plates immersion test.

3.3 Static Corrosion Tests

Samples are prepared by cutting the aluminum into small rectangular plates possessing a dimension of 1.5 x 1.5 x 0.15 cm (Figure 23). The exposed surface area in contact with cement is then 5.4 cm^2.. The samples were embedded two-by-two in four different cement conditions (such as mentioned before in Section 3.1). Plastic containers with 3 cm diameter and 5 cm height were used for the embedding process. For cement with the water-to-cement ratio of 0.8, due to low viscosity, Teflon® spacers were added between the two aluminum plates and at the bottom of the container to be sure the aluminum plates are embedded in the middle of the cement block. After hardening, the containers were removed to free the cement+Al samples (Figure 24). Finally, the samples were put in gas-tight containers filled with limewater up until 43.5 mm to create 18.5 mL of head space (Figure 25). The schematic of the container used in the static test is shown in Figure 26. The container is then connected to a system seen in Figure 27 to extract the H_2 gas. The H_2 content is then measured using a Gas Chromatography equipment. Calculation of the corrosion rate from the measured H_2 content is explained in Appendix F. The pressure from the barometer (Figure 27) is also used to calculate the number of moles of H_2 (see Section 2.8).

Figure 23. Small Al plates for static test.

Figure 24. Static test samples.

Figure 25. Static Test containers.

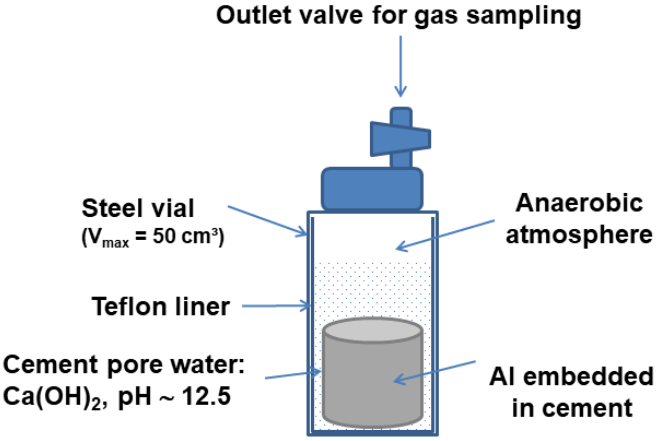

Figure 26. Static Test Setup.

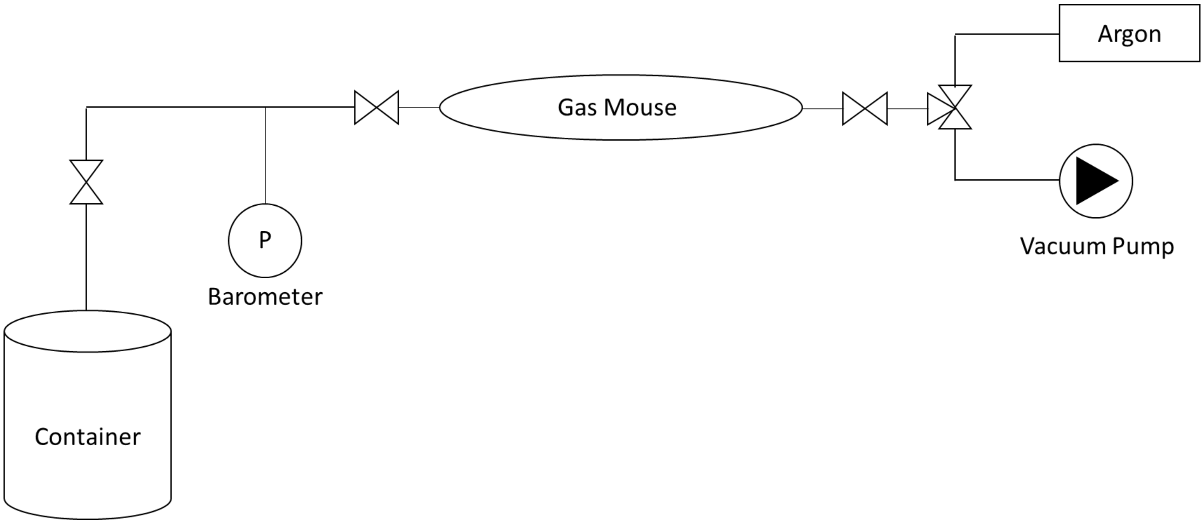

Figure 27. Gas Sampling System for the Gas Chromatography.

A Shimadzu GC-2010 Plus type gas chromatograph was used to quantitatively measure the hydrogen gas evolving from the corrosion reaction of Al. The carrier gas used was pure Argon (N7.5, Air Products), which passed through two gas purifiers (VICI Valco Instruments Co. Inc.) before entering the GC column in order to remove any residual impurities (H_2O, H_2, O_2, N_2, NO, NH_3, CO, CO_2 and CH_4). The injector used is a split/splitless injector made with material called ShinCarbon ST. A ShinCarbon ST composed of high surface area carbon molecular sieves. It is a micropacked column with dimensions of 2 m length x 1.27 mm outer diameter x 1 mm inner diameter. The detector used is a Barrier Discharge Ionisation Detector (BID). The detection limit of the BID is approximately 500 nL/L. To determine the H_2 concentration, a calibration curve was made by injecting calibration gas composed of argon containing different H_2 concentrations (1, 10, 100, 500, 10000 μL/L).

3.4 Porosity measurement for cement

Four cement samples were fabricated to measure the porosity condition of the cement. The different conditions of the cement samples are mentioned in Section 3.1.2. Cement samples were cast, demolded, and prepared inside a glove box. The samples were cast and demolded the day after. The samples were dried for a day after demolding. After drying, the samples were submerged in saturated $Ca(OH)_2$ (1.6 g/l) limewater for 70 days. After 70 days of immersion, the samples were taken out of the glove box and then dried for 3 days at room temperature. The dried samples were then hammered to reduce the size, as can be seen in Figure 28. The picture shows sample 3 (0.36 water-to-cement ratio), sample 7 (0.36 water-to-cement ratio with 3wt.% $LiNO_3$), sample 11 (0.8 water-to-cement ratio, sample 15 (0.8 water-to-cement ratio with 3wt.% $LiNO_3$).

Figure 28. Samples for Mercury Intrusion Porosimetry.

The samples were analyzed at VITO (Vlaamse Instelling voor Technologisch Onderzoek). Samples were analyzed using Mercury Intrusion Porosimetry (MIP). MIP experiments were performed using a PASCAL 140/440 porosimeter. MIP was done by pressurizing the sample and filling it with mercury. The pressurization was done in low and high pressure parts. In the low pressure part, after evacuation and mercury filling, the pressure was continuously increased up to 0.2 MPa and then reduced to atmospheric pressure before moving to the high pressure part. As pressure is applied, mercury fills the larger pores first. As pressure increases, the filling proceeds to smaller and smaller pores. The sample volume was determined from the low pressure part and also information of large pores was provided from this part. In the high pressure part, the pressure of mercury was continuously increased up to a maximum pressure of 200 MPa for all samples except for leached samples for which maximum applied pressure was 30 MPa in order to prevent large deformation of the samples. MIP is used to evaluate pore size, pore volume, and porosity of samples.

CHAPTER IV

RESULTS AND DISCUSSION

The measurement of the corrosion rate of the samples embedded in cement can be done mainly by three methods: Electrochemical Impedance Spectroscopy (EIS), measuring the H_2 gas produced from the corrosion by using e.g. Gas Chromatography (GC), and measuring the pressure of the H_2 gas produced during the corrosion reaction which can then be used to calculate the number of moles of H_2 by using the ideal gas law. EIS can determine the corrosion resistance linked to the corrosion rate (see Section 2.6). The GC measurement is performed by collecting the gas in a sealed container (see Figure 25 in Section 3.3) and subsequently extracting the gas and measuring it using a gas chromatograph (see Figure 27 in Section 3.3). The pressure of H_2 gas produced is also analyzed during the gas sampling made for the GC analysis.

As mentioned earlier (Section 3.4), the porosity of the cement can play an important role on the corrosion rate of the embedded metal. So, the porosity of the different cements studied needs to be known to understand the corrosion rate obtained by EIS and GC. Then, the first section of this chapter discusses the results from Mercury Intrusion Porosimetry (MIP) while the second and third sections are dedicated to EIS, GC measurements, and pressure measurements, respectively. The last section of this chapter discusses the comparison from EIS results with GC results.

4.1 Mercury Intrusion Porosimetry

The porosity of the cement is related to the corrosion rate of the aluminum sample. The easier the limewater coming from the outside can diffuse through the cement, the higher the corrosion rate will be. One of the parameters that can affect the diffusion of limewater is the porosity of the cement. The porosity of the cement is affected by the water-to-cement-ratio [5].

Figure 29 shows that cement with a 0.36 water-to-cement ratio has a mean pore size in volume around 10 nm, whatever the lithium content in the cement. This is around 3 times smaller than the pore radius obtained for the cements with a 0.8 water-to-cement ratio. Those cements possess a mean pore size in volume of 32 nm (without lithium) and 39 nm (with lithium). The pore size distributions are shown in Appendix E. The percentage of porosity change also depends on the water-to-cement ratio (Figure 30). For samples with a 0.8 water-to-cement ratio, the percentage of porosity is close to 30%. This is also around 3 times higher compared to the porosity of the 0.36 water-to-cement ratio samples, which are close to 7-10 %. Even if small differences can be observed, the addition of lithium doesn’t really affect the porosity of the samples.

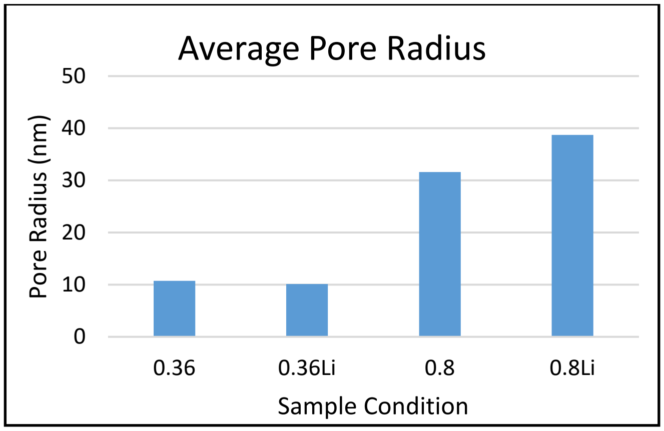

Figure 29. Average pore radius comparison.

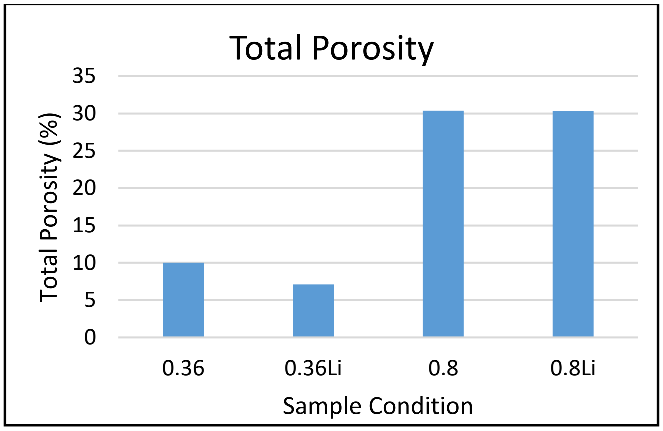

Figure 30. Total porosity comparison.

4.2 EIS Measurements

From EIS measurement, Nyquist and Bode plots are obtained (see Section 2.6). These results are explained in Section 4.2.1. EIS do not result in the direct measurement of a corrosion rate. To obtain the corrosion rate, Nyquist plots are fitted to an equivalent electrical circuit to obtain the charge transfer resistance (Rt) that is linked to the resistance of the corrosion process. Determination of Rt from the EIS results is explained in Section 4.2.1. After Rt is obtained, Tafel slope measurement was done to obtain the Stern-Geary Constant (B). B is required to calculate the corrosion rate which is explained in Section 4.2.2. Last part of Section 4.2 explains the corrosion rate calculation using the Rt and B obtained and compares the results of the corrosion rate.

4.2.1 EIS Measurements

EIS measurements were done during a three months period at regular intervals (approximately one measurement every week). As mentioned in the previous chapter (Section 3.1.2), the measurement were done for four types of cement with five series of samples for each condition. This section is focused only on some of these series. Indeed, only one series is presented when results are similar. Moreover, some problems appeared with some samples:

- Cracks appeared on all samples with 0.8 water-to-cement ratio without lithium. Cracks appeared due to stress caused by high H_2 pressures produced by the corrosion reaction or due to the lower density of the corrosion products that induce mechanical stresses in the cement.
- Cracks appeared on all samples with 0.36 water-to-cement ratio without lithium (Figure 31), except for sample in Series 1.
- Cracks appeared on sample 0.8 water-to-cement ratio with lithium in Series 5.
- Broken connecting wires on all samples with 0.8 water-to-cement ratio without lithium (Figure 29), except for sample in Series 3. Broken wires are caused by corrosion of the wire, because it was sometimes welded on the front site of the sample, too close to the surface in contact with the cement (see Section 3.2).
- Broken connecting wires on samples with 0.36 water-to-cement ratio without lithium in Series 4 and Series 5.

The full results of the EIS measurements are presented in Appendix A. The format used to describe the samples is "water-to-cement_ratio_series_Days". For example, 0.36Li_1_Day1 is the tag of sample with 0.36 water-to-cement ratio plus lithium from series 1 taken at day 1 of measurement and 0.8_4_Day35 is the tag of sample with 0.8 water-to-cement ratio without lithium from series 4 taken at day 35 of measurement period. Usually, the EIS measurements were realized by analyzing the systems from high-to-low frequency range. However, to check the stability of the system, each sample was also analyzed from low to high frequency. These analyses are represented with dotted lines in Figure 33 to Figure 38.. Indeed, if both low-to-high and high-to-low frequency responses are similar, this means that the studied system is stable within the analyzing time, leading to reliable EIS results. In this study, the EIS responses are very similar whatever the frequency direction, meaning that our systems are stable over the time range of our measurement.

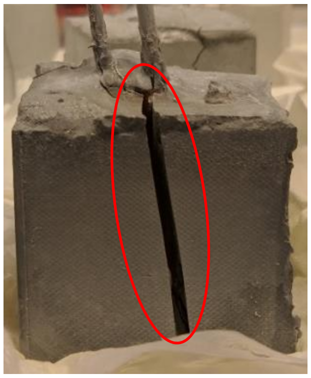

Figure 31. Crack in the sample 0.36_2.

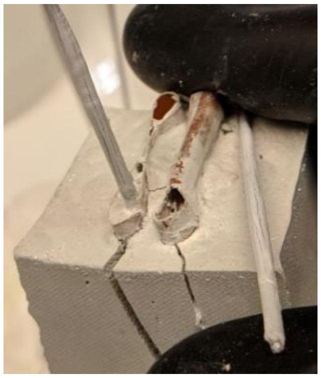

Figure 32. Broken Wire in sample 0.8_4.

The EIS measurement results for 0.36_1, 0.36_2, 0.8_3, 0.8_4, 0.8Li_1 and 0.36Li_1 are presented in Figure 33 to Figure 38, respectively. Figure 33 (sample 0.36_1) shows a Nyquist plot with a semicircle which correlates with the impedance of the corrosion process [16] (see Section 2.6). The radius of the semicircle increases with the time of measurement. This is caused by the increase of the polarization resistance of the corrosion process with time [16]. The polarization resistance is the charge transfer resistance of the aluminum corrosion reaction [8] and it is affected by the available water for the corrosion process to occur. The increase shown in Figure 33 results from the lack of water because the cement porosity limits the mass transfer for the limewater to make contact with the Al even though the cement is submerged in limewater. The increase of polarization resistance shows the decrease of corrosion rate, which will be explained in Section 4.2.4. There is a significant difference observed in Figure 33 compared to Figure 34 (sample 0.36_2). In Figure 34 the radius of the semicircle increases up to 27 days before it decreases again. The increase of the polarization resistance in sample 0.36_1 is caused by the decrease of water in cement due to the corrosion process where at one point the only water available is the water that is able to diffuse through the cement, while in sample 0.36_2 the same thing happened until a crack was formed after 27 days. The crack in sample 0.36_2 created a pathway for the water surrounding the cement block to make contact with the aluminum sample and increase the corrosion again. After 27 days, the corrosion decreases again until it reaches a steady state. This could be caused by the formation of corrosion products and the subsequent precipitation of $Ca(OH)_2$ from the limewater that will fill the crack thereby limiting the contact of limewater with the aluminum plates.

Samples with 0.36 water-to-cement ratio with lithium addition have the same pattern for all the EIS measurements. Result for sample 0.36Li_1 can be seen in Figure 35 and all the other results are reported in Appendix A. It shows a Nyquist plot with a semicircle. The radius of the semicircle is increasing in time. By comparing Figure 33 (sample 0.36_1) and Figure 35 (sample 0.36Li_1) it can also be roughly seen that the radius of the semicircle is bigger for sample 0.36Li_1 compared to sample 0.36_1. It shows the effect of lithium to minimize the corrosion (see Section 2.5). This issue will be discussed further in Section 4.2.4.

During the measurement period of all the five samples of 0.8 water-to-cement ratio, only the Al wire of sample 0.8_3 remained intact (i.e. it was not broken). Some of the wires were broken because of corrosion. This was believed to be caused due to a flaw in the design of the aluminum electrodes. Indeed, for some plates the wire was welded on the front side too close to the aluminum surface in contact with the cement, leading to difficulties to properly cover the aluminum sample with the non-conductive tape. Then, due to this flaw in the design of some samples, corrosion also took place on the connecting wires.

Figure 36 shows the Nyquist plot from sample 0.8_3. It can be seen that the phenomenon observed for sample 0.8_3 is very similar to the one of sample 0.36_1 in Figure 33. The semicircle radius is seen to increase with time. Sample 0.8_3 suffers from cement cracking but no anomaly was observed in the Nyquist plots. The reason is that the corrosion in 0.8 water-to-cement ratio is very high in the beginning, but decreases in time. So when the crack occurred during the measurement period it cannot be seen very clearly.

The Nyquist plots obtained from sample 0.8_4 are shown in Figure 37. A huge sudden increase of the semicircle is observed after day 28 along with a very noisy result. This is believed to be caused by the corrosion of the wire leading to a bad connection with the Al plate and innacurate EIS measurement. However, up to 28 days, Figure 37 shows that the semicircle radius obtained for sample 0.8_4 is quite similar to the ones of sample 0.8_3 (Figure 36). Figure 38 shows that the results for samples with 0.8Li_1 lithium are similar to the results for samples with 0.36Li_1 (Figure 35) but with a smaller radius of the semicircle.

According to Delpech in 2017 [8], the Nyquist plot consists of three impedances: the impedance due to mortar at high frequency (semicircle in the left), and by two impedances caused by the oxidation of aluminum and reduction of water (see Section 2.4.1). The difference between the samples without lithium (Figure 33 and Figure 36) and the samples with lithium (Figure 35 and Figure 38) is that the semicircle in the high frequency is very small and cannot be clearly seen. The low frequency impedance (semicircle in the right) cannot either be seen clearly. To obtain more information, the frequency range should be extended. This would lead to a longer analysis time. To get more information on the impedance in function of the frequency, Bode plots can also be analyzed.

Examples of the Bode plots can be seen in Figure 39 and Figure 40, respectively for samples 0.36_1 and 0.36Li_1. All the Bode plot results can be seen in Appendix A. From the Bode plots, the frequency range where the corrosion is occurring can be deduced. In this study, corrosion appeared between 100 mHz and 1 kHz. The frequency where the corrosion process is taking place is similar for all samples.

The Bode plot correlates with the Nyquist plot. The increase of Nyquist plot semicircle is seen as a shift up of the graph in Figure 39A and a phase shift in Figure 39B.Then a shift up in Bode plot corresponds to lower corrosion rate such as an increase in Nyquist plot semicircle. The comparison of Figure 39 and Figure 40shows that more shift in the Bode plots are observed for sample without lithium (idem for 0.8 and 0.8Li samples (Appendix A)).

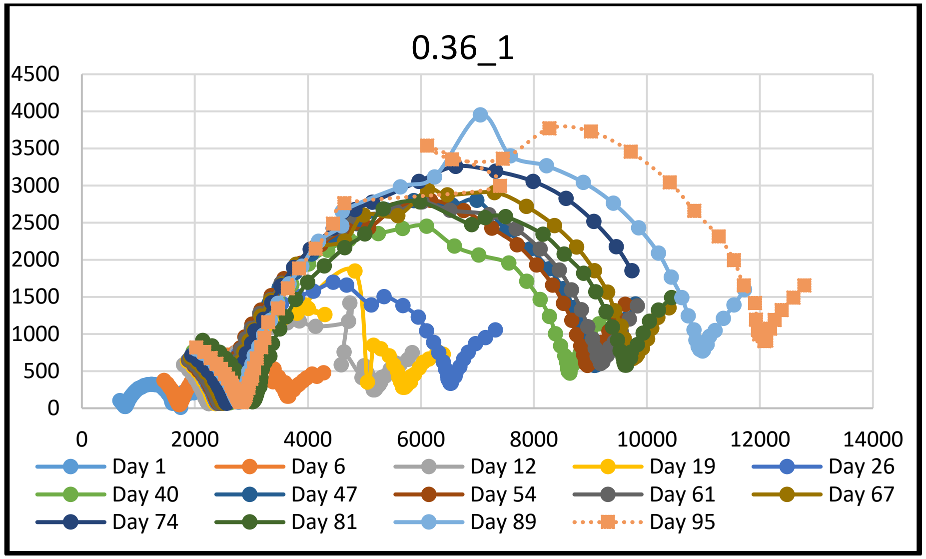

Figure 33. EIS Measurement of 0.36_1 (0.36 without crack).

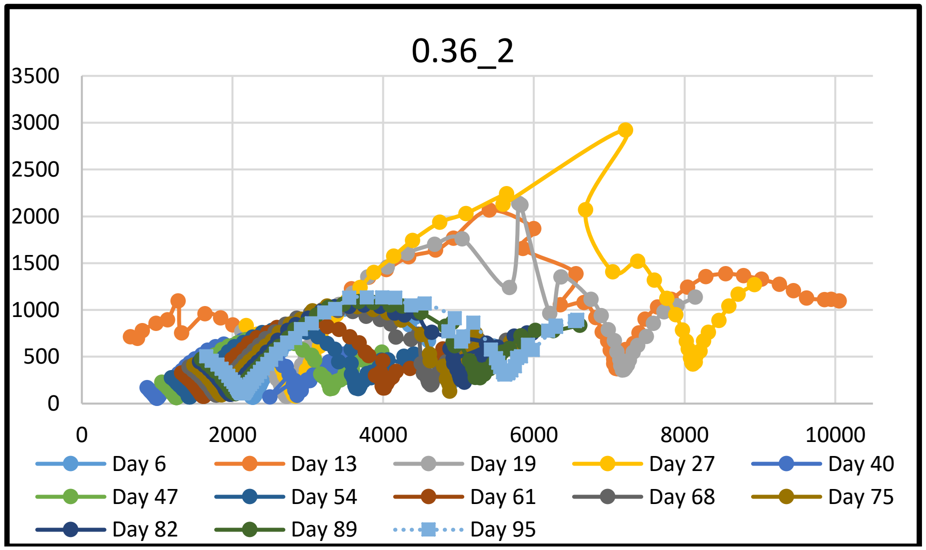

Figure 34. EIS Measurement of 0.36_2 (0.36 with crack).

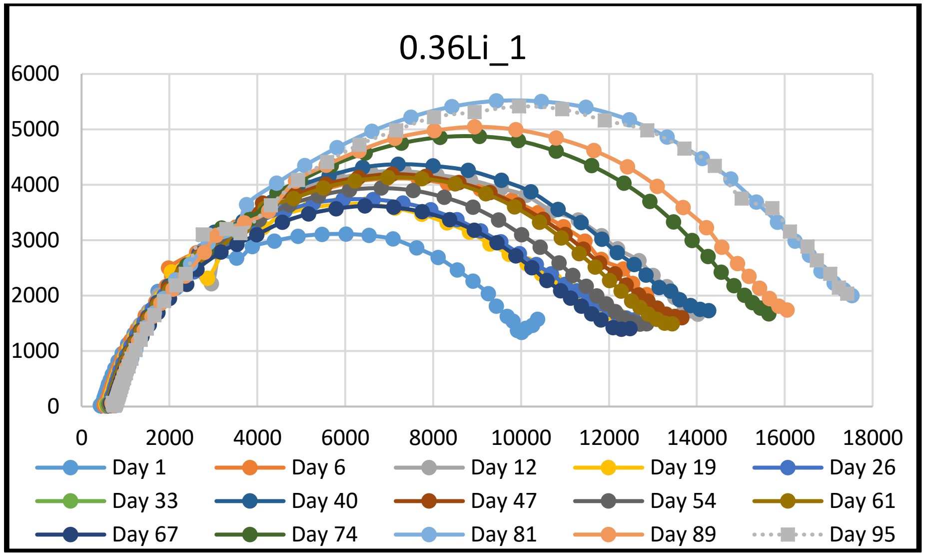

Figure 35. EIS Measurement of 0.36Li_1.

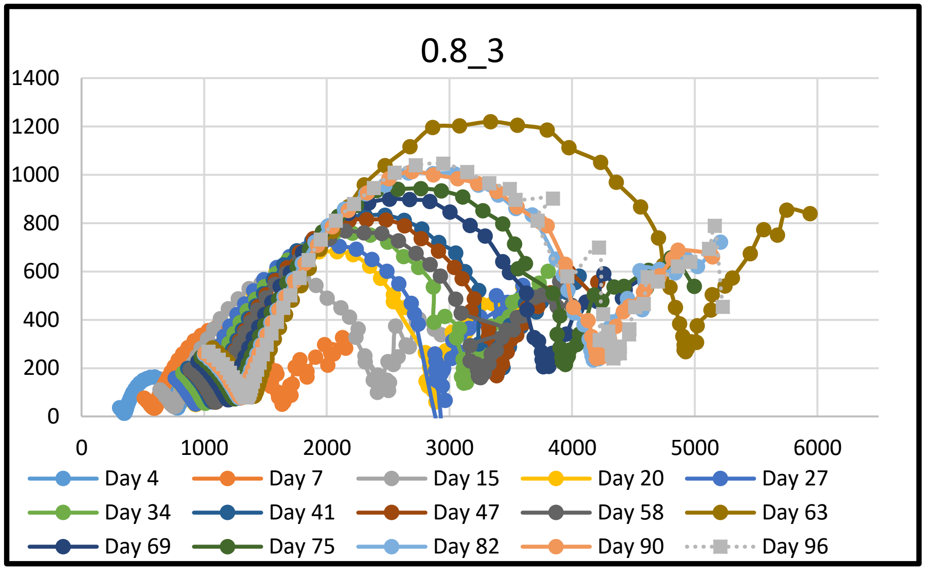

Figure 36. EIS Measurement of 0.8_3 (0.8 without broken wire).

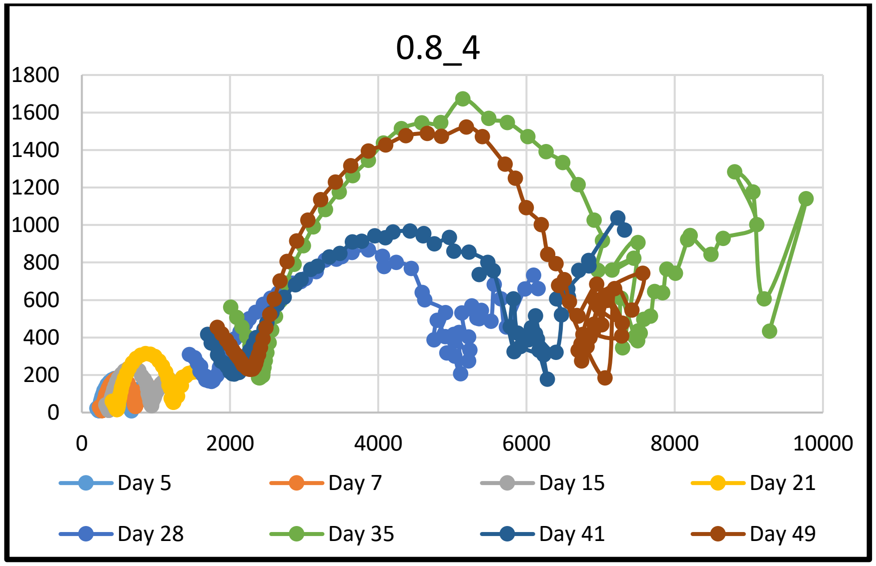

Figure 37. EIS Measurement of 0.8_4 (0.8 with broken wire).

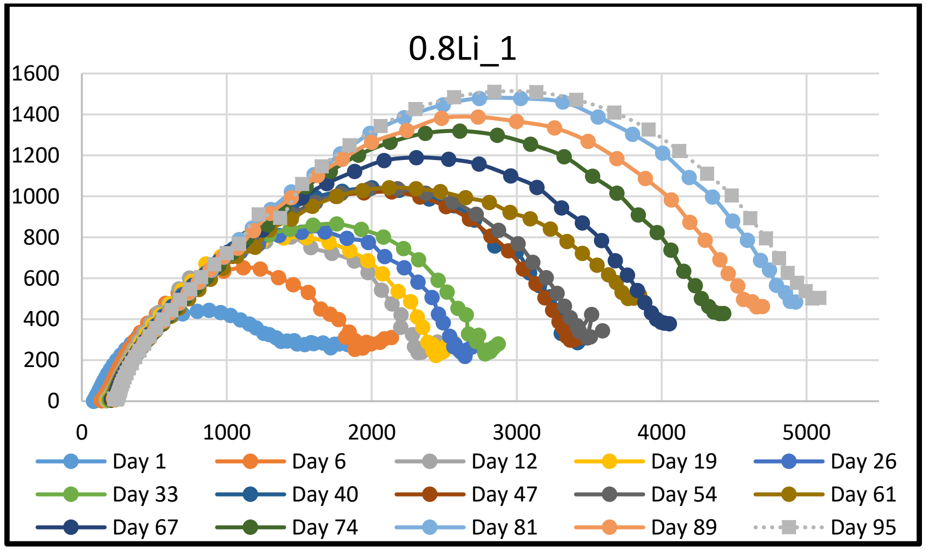

Figure 38. EIS Measurement of 0.8Li_1.

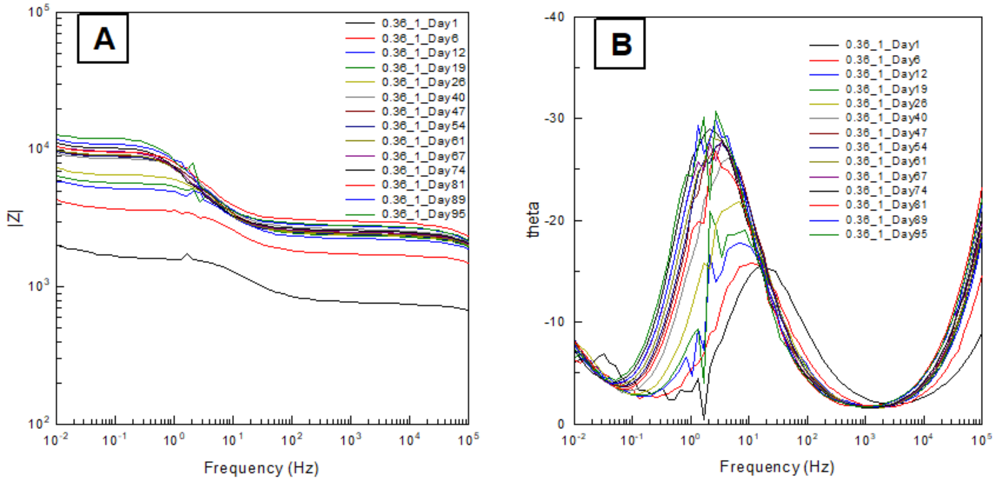

Figure 39. Amplitude and phase angle Bode plots of 0.36_1.

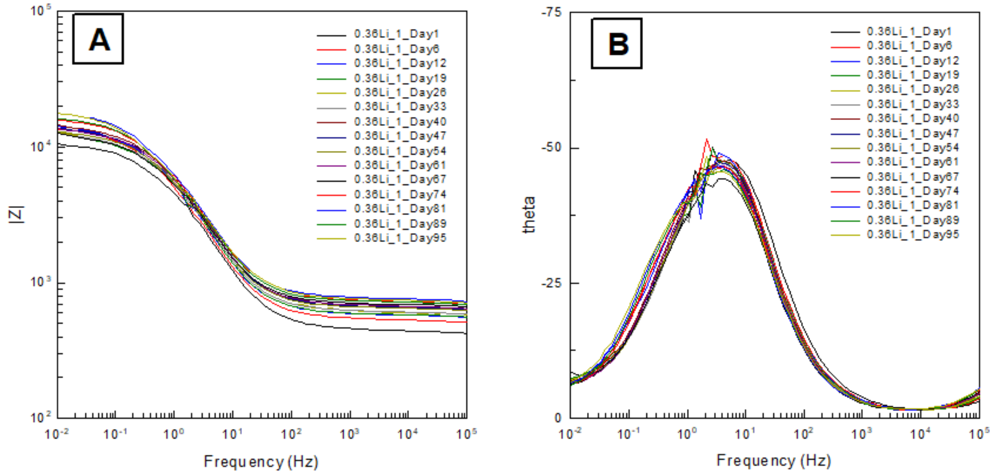

Figure 40. Amplitude and phase angle Bode plots of 0.36Li_1.

4.2.2 Determination of Charge Transfer Resistance (Rt)

To be able to determine the Charge Transfer Resistance (Rt), which is needed to calculate the corrosion rate, an equivalent electrical circuit needs to be constructed to model the studied system. In this study, the model used is the same than the one used by Delpech et al. [8], because it correlates with aluminum corrosion inside a cement matrix (Figure 38). This equivalent electrical circuit is then used to fit the EIS measurement results described in the previous section (and in Appendix A). This was done by using the Zview software.

This model consists of three parts modelling the effect of the solution, the cement, and the aluminum. The solution part consists of one resistor modeled as Rs. The cement part consists of two resistors and two constant phase elements where R_{CEM1} is the impedance of continuously connected micro-pores in the cement, CPE_{CEM1} models the capacitance across the cement, R_{CEM2} and CPE_{CEM2} models the discontinuous connected micro-pores of the cement. The last part, corresponding to the aluminum, consists of one resistor and one constant phase element where CPE_{CD} is the double layer capacitance and Rt is the charge transfer resistance. Rt is the important parameter needed to calculate the corrosion rate (see Section 2.6).

One example for circuit fitting is presented in Figure 42, which is the circuit fitting of the EIS results of sample 0.36_1_Day1. All the results of the Rt from the circuit fitting is given in Appendix B. The Rt is then used to measure the corrosion rate which will be discussed in Section 4.2.4.

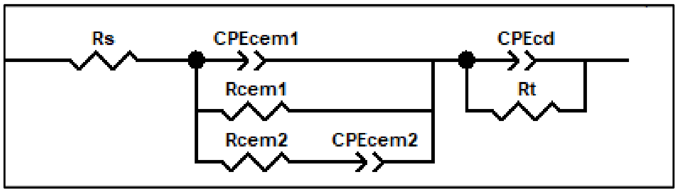

Figure 41. Circuit used to fit the EIS Result.

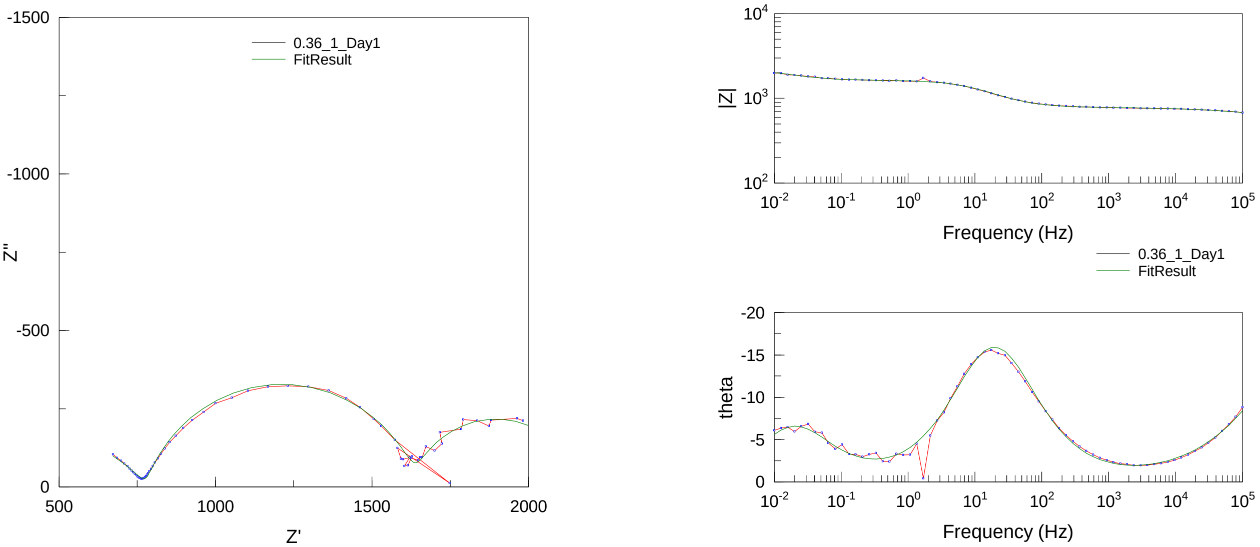

Figure 42. Circuit fitting the EIS results of sample 0.36_1_Day1.

4.2.3 Tafel Slope Measurement

Tafel slope measurements by linear polarization were done to determine the parameter of ba (anodic slope) and bc (cathodic slope) (see Section 2.6). The ba and bc were then used to calculate the Stern-Geary Constant (B) by using Equation 12. The result from the measurement can be seen in Figure 43. The Tafel slopes were determined by choosing two points in the linear section of the anodic and cathodic branch of the polarization curve manually. There are some uncertainties in the manual part of determining the two points, leading to uncertainties on the B values. The full results for the Stern-Geary constant measurement can be seen in Appendix C and the averaged of all the measurements of B leads to an average value of 32 (Table 1). The average value for B value is then used to the calculate the corrosion rate (see Section 2.6) which will be discussed in Section 4.2.4.

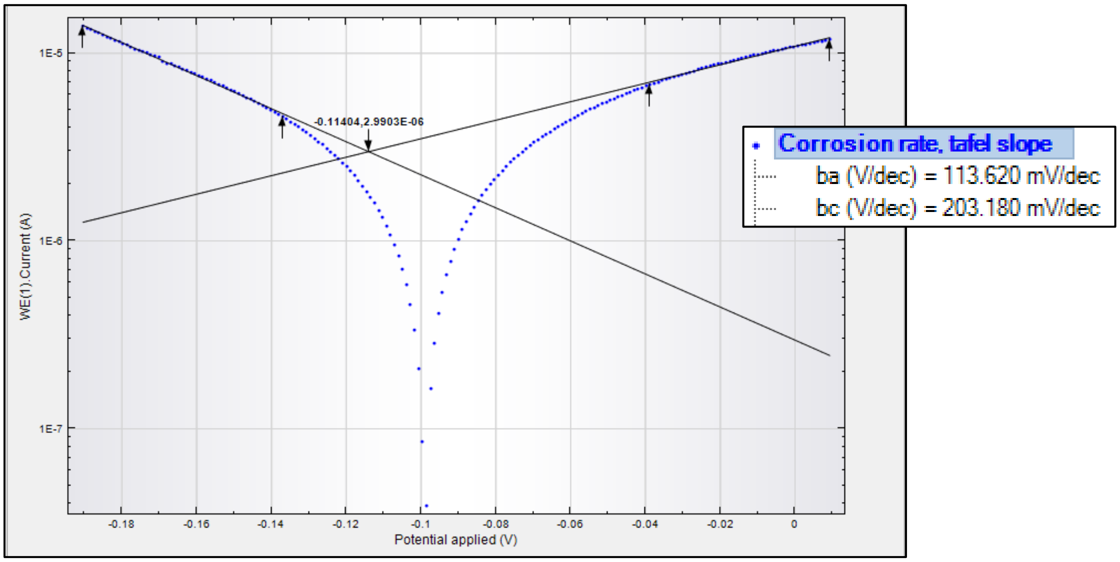

Figure 43. Example of Tafel slope measurement result by Linear Polarization.

$$\frac{1}{2.30}\ x \left(\frac{\text{ba x bc}}{\text{ba+ bc}}\right) = \text{B} \qquad (12)$$

Table 1. Stern-Geary Constant (B) from Tafel slope measurements.

B Min	29
B Max	38
B Average	**32**

4.2.4 Corrosion Rate Calculation

After obtaining the Rt from the EIS measurements (Section 4.2.2) and B from the Tafel slope measurements (Section 4.2.3), Equation 9 and 10 from Section 2.6 were used to measure the corrosion rate. All corrosion rate calculations and results are given in Appendix B and D, respectively.

A summary of the corrosion rates calculated from the EIS measurements of samples with 0.36 water-to-cement ratio can be seen in Figure 44. When interpreting this graph, it must be noted that samples 0.36_4 and 0.36_5 were corroded at the wire and inaccurate data were recorded after 40 days of testing. However, when considering the results from the tests without wire corrosion, it was observed that the samples without cement cracks (0.36_1) showed a lower corrosion rate compared to the samples with cracks (0.36_2 and 0.36_3). After a few days, the corrosion rate reached a steady state in the range of 14 µm/yr to 40 µm/yr, respectively for sample without or with cracked cement.

The same phenomena can be observed for the samples with lithium (0.36Li, Figure 45). The corrosion rate decreases in time to reach a lower value compared to samples 0.36 water-to-cement ratio without lithium (Figure 41). As mentioned by Matsuo [13] and in Section 2.5, this is probably due to the formation of a passive layer of complex Li-Al at the surface of the Al plate. The complex Li-Al passive layer is responsible for lowering the corrosion rate. At the end of the measurement period the corrosion rate ranges between 5 and 11 µm/yr.

Figure 46 shows the result of the corrosion rates for sample with 0.8 water-to-cement ratio. It can be seen that only sample 0.8_3 was able to be analyzed until the end of the measurement period, while the other samples suffered severe wire corrosion making it impossible to continue the measurement. Sample 0.8_3 reached a corrosion rate of 50 µm/yr at the end of the measurement. Although other 0.8 samples had experienced wire corrosion problems, the same trend of high initial corrosion rate that decreased over time could be observed in all samples with 0.8 water-to-cement ratio.

In contrast to sample 0.8 water-to-cement ratio without lithium, all 0.8 water-to-cement ratio samples with lithium were able to be analyzed until the end of the measurement period (Figure 47). The corrosion rate of 0.8Li samples also decreased over time just like the other samples. At the end of the measurement period the corrosion rate ranged between 20 and 33 µm/yr. The corrosion rate of 0.8Li is higher compared to 0.36Li. This can be caused by the higher porosity of samples 0.8Li compared to samples 0.36Li (see Section 4.1). This allows more water to be able to diffuse inside the cement and enter in contact with the aluminum. Moreover, this higher porosity allows a higher mass transfer of corrosion product through the cement. This extra water available at the surface of the aluminum can lead to a faster dissolution of the protective Li-Al protective layer. Indeed, the extra water available in the cement and the faster mass transfer through the cement (due to higher porosity) induces a faster decrease of the soluble lithium nitrate present in the cement, leading to a shift of the equilibrium to the dismantling of the Li-Al layer and to the increase of the corrosion rate. Even though the corrosion rate of samples 0.8Li is higher than the one of samples 0.36Li. It can be once again observed that lithium addition greatly reduces the corrosion rate by comparing Figure 46 and Figure 47.

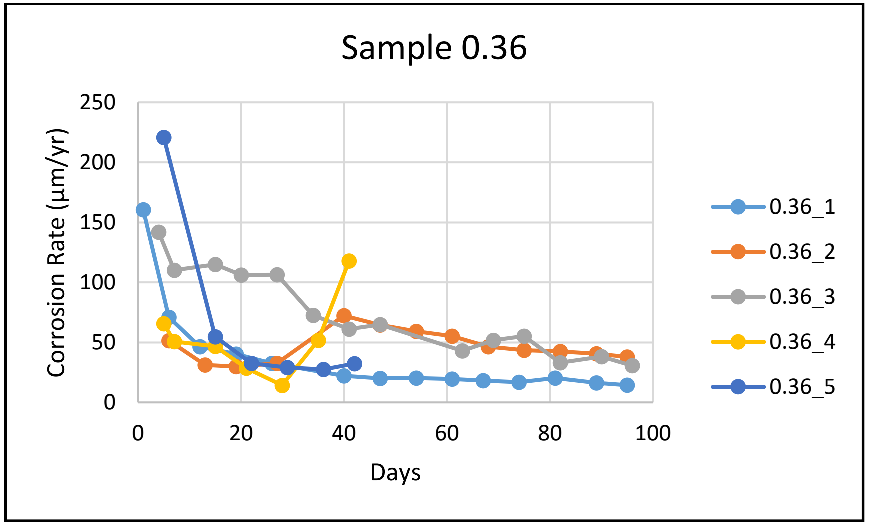

Figure 44. Corrosion rate comparison of 0.36 Samples.

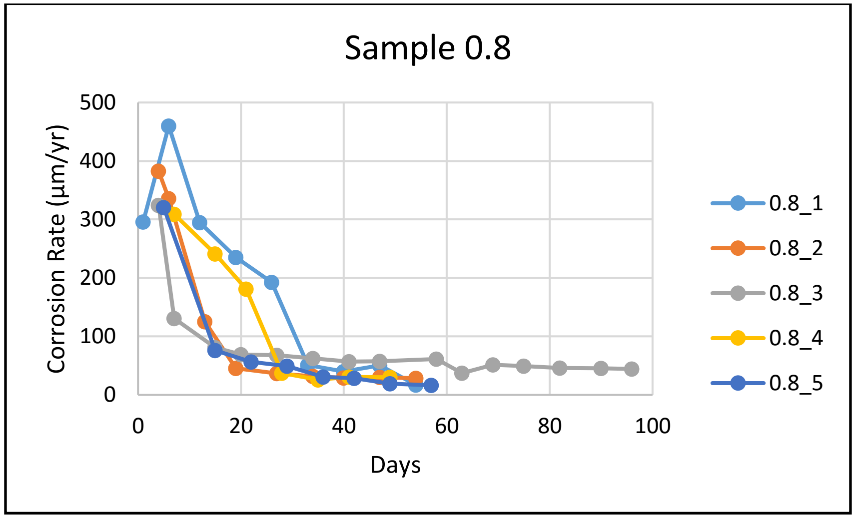

Figure 46. Corrosion rate comparison of 0.8 Samples.

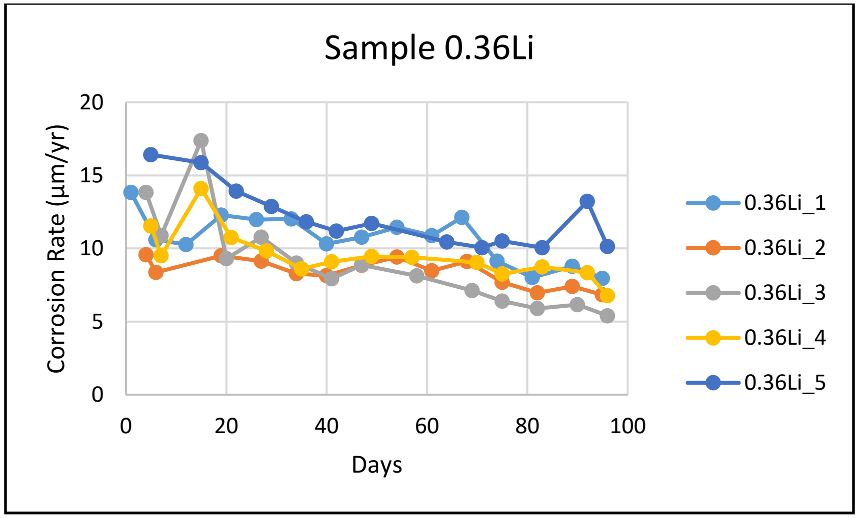

Figure 45. Corrosion rate comparison of 0.36Li Samples.

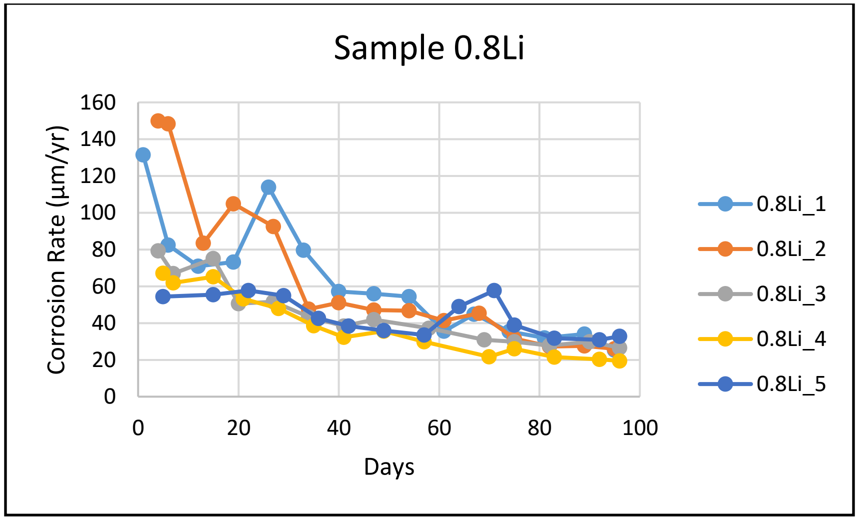

Figure 47. Corrosion rate comparison of 0.8Li Samples.

In order to compare more easily the measured corrosion rates as a function of the different cements, Figure 48 shows an overview of the most representative results from each cement. Figure 48 shows the evolution of corrosion rate for all samples in Series 3.

It can be seen that in time a decrease of the corrosion rate is observed. The decrease of the corrosion rate is most likely caused by the depletion of OH^- in the local environment surrounding the aluminum [12]. The corrosion rate of the samples reached a steady state after ~40 days. At this point the corrosion is caused by the limewater diffusing through the cement up to the Al plates. Corrosion of Al results in dissolved Al in the local environment of the plate. This results in a solution enriched in Al ions in the surrounding of the Al plates. The high amount of dissolved Al in the solution should also lower the corrosion rate (see Section 2.4.1). After ~40 days the steady state can be caused by the equilibrium of limewater diffusing inside the cement and the Al-rich solution diffusing out of the cement.

At the end of the measurement period it can be seen that the corrosion rate is the highest for cement with 0.8 water-to-cement ratio, and the lowest for samples with 0.36 water-to-cement ratio with lithium, while the corrosion rate of 0.8Li and 0.36 samples are quite similar. Similar results can be seen in all series (Appendix D). It can also be seen that the samples with the higher water-to-cement ratio will result in higher corrosion rates mainly due to the higher porosity of these cements.

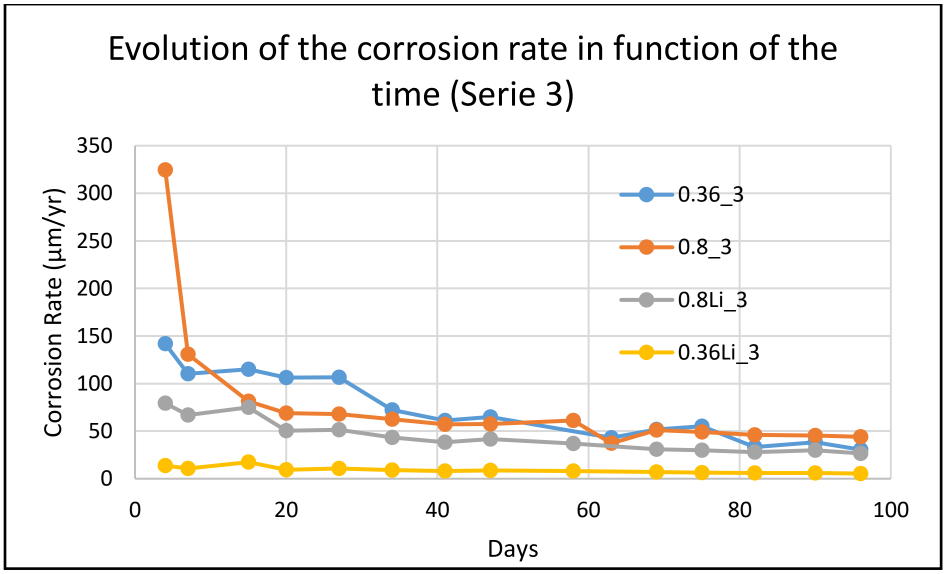

Figure 48. Corrosion rate comparison of Series 3.

Figure 49 shows the average corrosion rate of different samples:

- sample 0.36_1 to represent samples with 0.36 water-to-cement ratio without cracking;
- samples 0.36_2 and 0.36_3 to represent samples with 0.36 water-to-cement ratio with cracking;
- sample 0.8_3 to represent samples with 0.8 water-to-cement ratio with cracking;
- all samples 0.36Li, to represent samples with 0.36 water-to-cement ratio with lithium (and without cracking); and

- all samples 0.8Li, to represent samples with 0.8 water-to-cement ratio with lithium (and without cracking).

All the samples with broken wires were not used in the average corrosion rate calculation. Two averages are used in Figure 49. The grey bar is the average for the total measurement period and the green bar is the value calculated during the period after the steady state was reached (i.e. after 40 days)

The average corrosion rate, measured over the entire measurement period, shows that sample 0.36Li has the lowest corrosion rate. This result affirms that the addition of lithium together with the lower water-to-cement ratio induces a reduction of the corrosion rate of aluminum. The lower corrosion rate of samples 0.8Li compared to samples 0.8 affirms once again the capability of lithium to reduce corrosion. The lower corrosion rate of samples 0.36 compared to sample 0.8_3 during the total measurement period shows that a lower water-to-cement ratio leads to a lower corrosion rate. This is probably also partly due to the fact that higher water-to-cement ratio samples have a higher porosity that allows more limewater to diffuse inside and corrode the Al.

The average corrosion rates in the steady state period show that the corrosion rate for the cracked samples (0.36_2, 0.36_3, and 0.8_3) achieves similar corrosion rates in the steady state period. In the steady state period, the corrosion rate of sample 0.36 is lower compared to sample 0.8Li. This means that it is important to have lower water-to-cement ratios to achieve lower corrosion rates. It is linked to the higher porosity of 0.8Li that allows the limewater to diffuse easier in the cement and corrode the aluminum even though there is lithium in 0.8Li, because the lithium is not stable in the presence of water. Comparing the average corrosion rate of sample 0.36_1 to that of sample 0.8_3 in the steady state period affirms that a higher porosity causes higher corrosion rates. This is also related to the ability of limewater to diffuse easier in 0.8_3 because of the higher porosity. Comparing 0.8_3 with 0.8Li shows that even though lithium is very soluble in water, in the steady state period there is still lithium that allows a lower corrosion rate in 0.8Li.

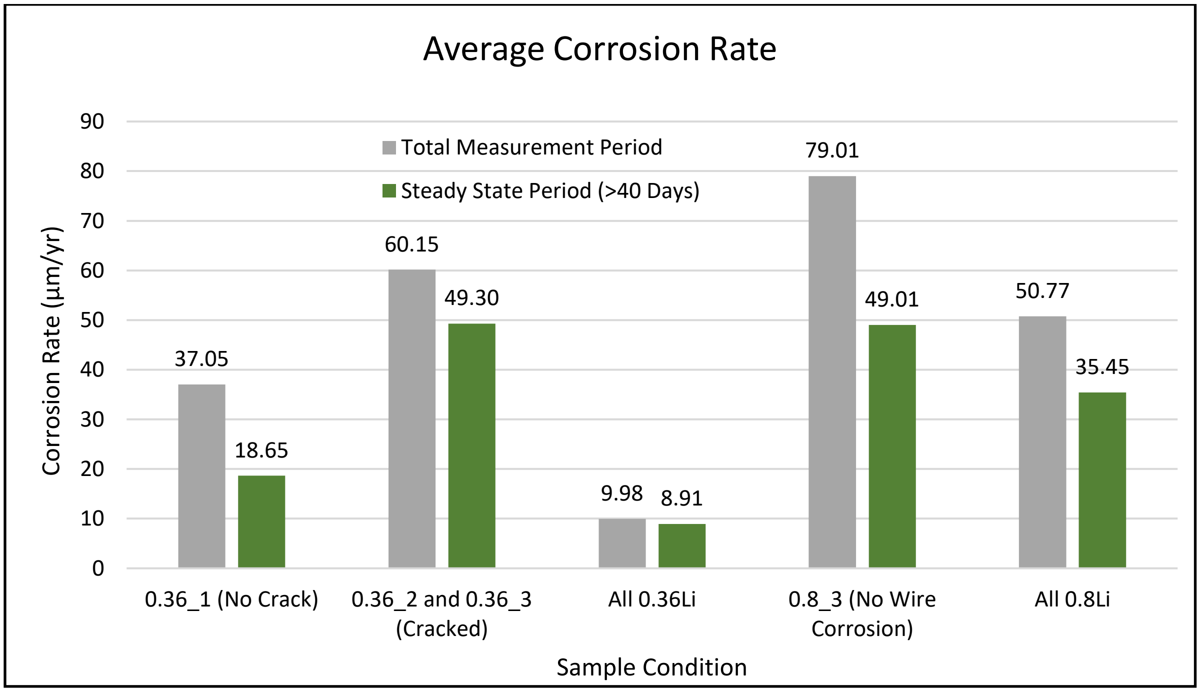

Figure 49. Average corrosion rate.

The main conclusions from the corrosion rate calculations are:

- all corrosion rates of the samples decrease over time and reach a steady state after 40 days;
- lithium is able to significantly decrease the corrosion rate;
- higher water-to-cement ratio results in a higher corrosion rate which is believed to be due to the higher water availability to corrode the Al and higher porosity to allow limewater to diffuse inside the cement;
- cement with a 0.36 water-to-cement ratio with the addition of lithium addition should be the best option to minimize the corrosion of aluminum.

4.2.5 EIS Measurement for Bare Aluminum in Saturated Limewater

The Nyquist plots and Bode plots for bare aluminum immersed in saturated limewater can be seen in Figure 50 and Figure 51, respectively. The Nyquist plots obtained from bare aluminum in limewater are similar to the ones obtained for aluminum in cement (Section 4.2.1) where the radius of the semicircle correlates to the charge transfer resistance. The Bode plots in Figure 51 show the frequency of the corrosion similar to aluminum samples embedded in cement (Figure 39 and 40) (see Section 4.2.1).

The measurement of the Tafel slopes and the calculation of the B value are gathered in Appendix C. The average B value used to calculate the corrosion rate is equal to 30 (Table 2), which is similar to the average B value used for aluminum in cement matrix (see Table 2 in Section 4.2.3).

The calculation of Rt from the EIS results was realized by using another equivalent electrical circuit than the one used to fit the EIS curves recorded for aluminum samples embedded in cements (see Section 4.2.2). The circuit used in this section is the one adopted by Liang Fan (2016) [17]. The circuit is shown in Figure 52. This circuit is used because there is no cement contribution for the case of bare aluminum in limewater. There are two parts in this circuit. The first part is the solution part where Rs represents the solution resistance. The second part is the corrosion process where Rt is the charge transfer resistance of the corrosion, CPE_1 is the double layer capacitance in the corrosion process, Rc is the charge transfer resistance of precipitation in the Al surface and CPE_2 is the double layer capacitance of the precipitation in the surface. The Rt is the main parameter used to calculate the corrosion rate. The Rt from the fitting is then used to calculate the corrosion rate (see Section2.6).

The test was done using three identical samples. The samples are called Al_1, Al_2, and Al_3. The corrosion rate can be seen in Figure 53. The corrosion is high in the beginning but it reaches a steady state instantly in a few days. The steady state period shows a value of 78 µm/yr. The corrosion rate in the steady state period is higher compared to values observed when aluminum is embedded in cement. (Section 4.2.4).

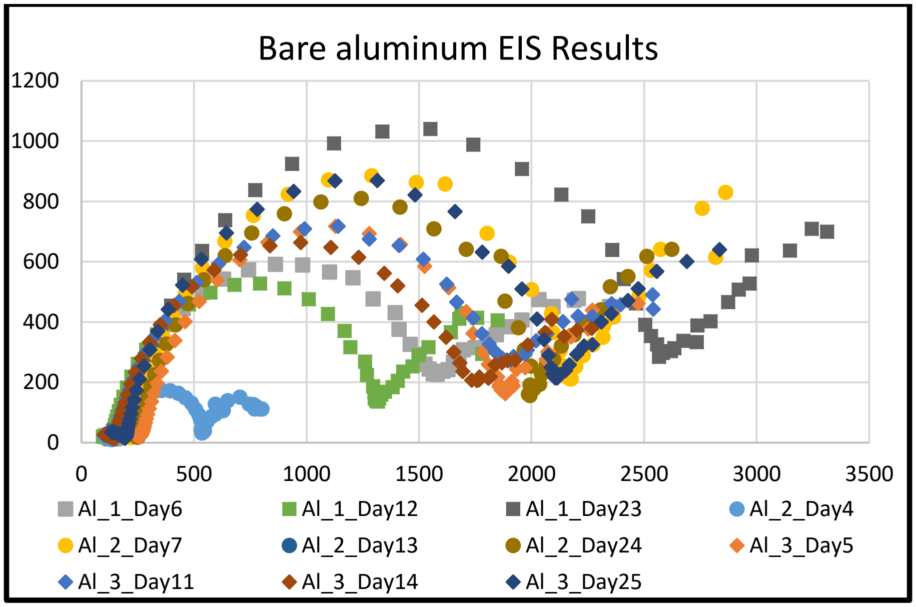

Figure 50. Nyquist plot of bare aluminum.

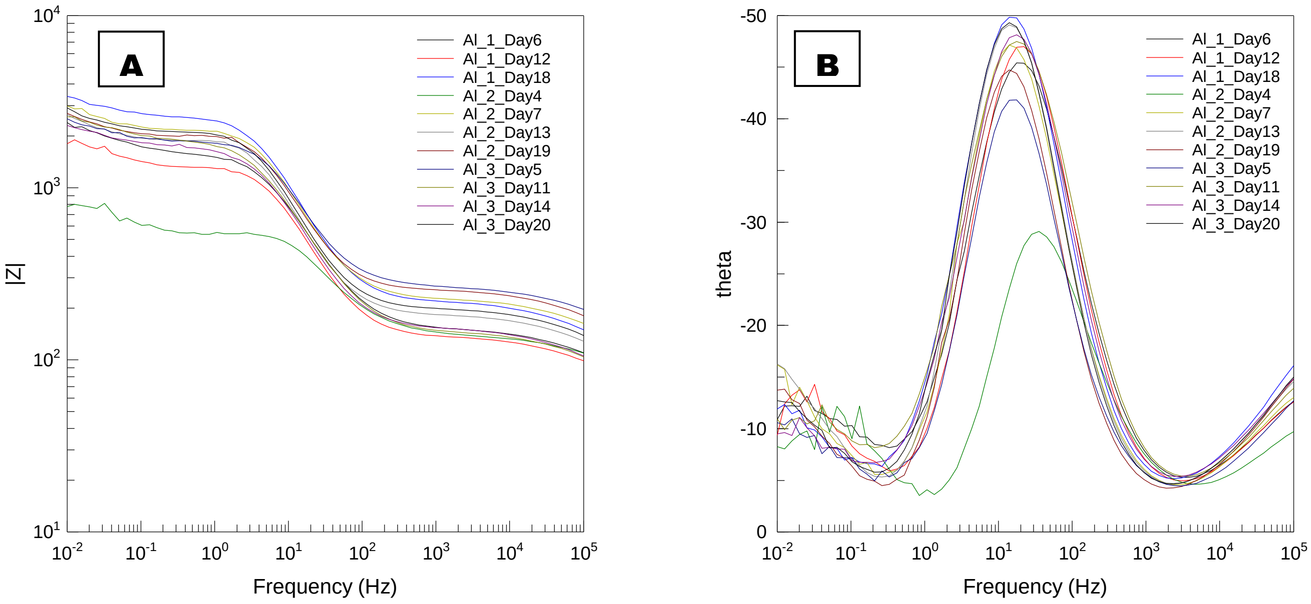

Figure 51. Bode plot of bare aluminum.

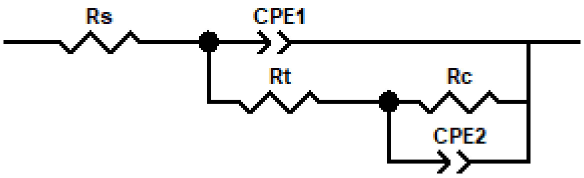

Figure 52. Circuit used for Bare aluminum EIS fitting.

Table 2. Stern-Geary constant (B) for bare aluminum

B Min	26
B Max	33
B Average	**30**

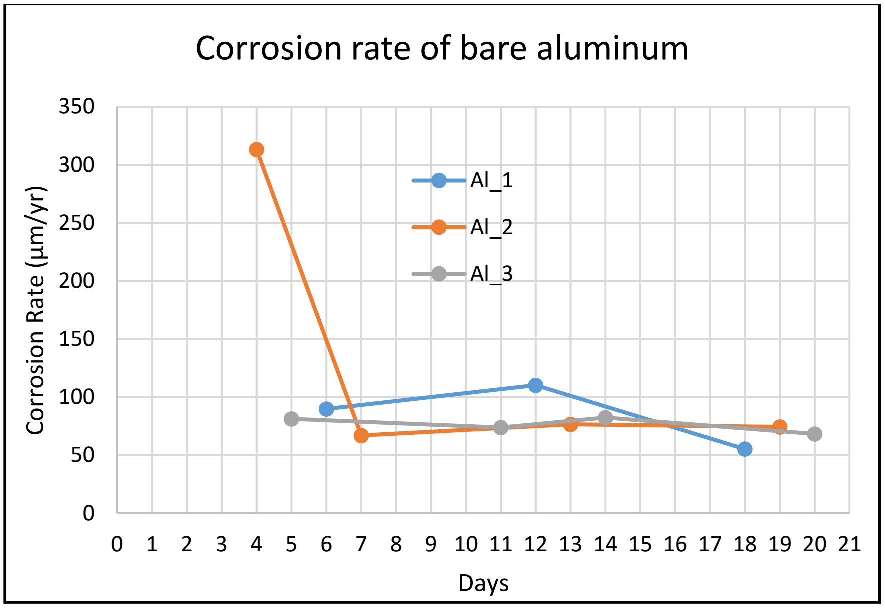

Figure 53. Corrosion rate of bare aluminum in $Ca(OH)_2$.

A layer of corrosion products could also be observed on the surface of the plate (Figure 54). The corrosion rate of the bare aluminum decreased rapidly reaching a steady-state value of ~78 µm/yr. Sample Al_2 revealed a very high initial corrosion rate, which was not observed in the other samples. This is maybe due to the fact that the first EIS analysis was realized on this sample after 4 days of corrosion, while the first analysis for Al_1 and Al_3 was done after 6 and 5 days, respectively (Figure 53). According to Bailey and Takatani [18] limewater causes surface pitting corrosion of aluminum and corrosion decreases soon due to the formation of an insoluble surface film of calcium aluminate $Ca(AlO_2)_2$ by the reaction of aluminate ions AlO_2^- that are present at pH values above 12, with Ca^{2+} ions originating from the dissociation of $Ca(OH)_2$.

Figure 54. Bare aluminum plate corrosion.

Comparing the corrosion rate of aluminum embedded in the four different cements with the corrosion rate of the bare aluminum (when the steady state is reached), it can be seen that the corrosion of bare aluminum is higher compared to aluminum embedded in cement. Similarities between bare aluminum immersed in limewater and aluminum embedded in cement is that in both conditions the corrosion rate decreases over time. In the bare aluminum tests, there was no cement to limit the contact of limewater to the cement. The cement matrix is able to influence the limewater mass transport thus decreasing the corrosion rate of aluminum.

4.3 Static Corrosion Test Results

From the static corrosion tests, the corrosion rate was calculated by two different methods. First, the corrosion rate was calculated from the H_2 production measured by GC. Secondly, the corrosion rate was calculated from the measured pressure in the container. The full calculation can be seen in Appendix F.

Figure 55 shows the samples post static corrosion test. There are no major cracks observed such as for the EIS samples (see Figure 31). However, some holes and small cracks are observed in the samples (red circles in Figure 55), except in sample 0.36Li which is not altered after 98 days in saturated limewater. Note that the shape of the sample 0.8 is due to manipulation problems at the beginning of the test, when the cement was removed from the plastic vial.

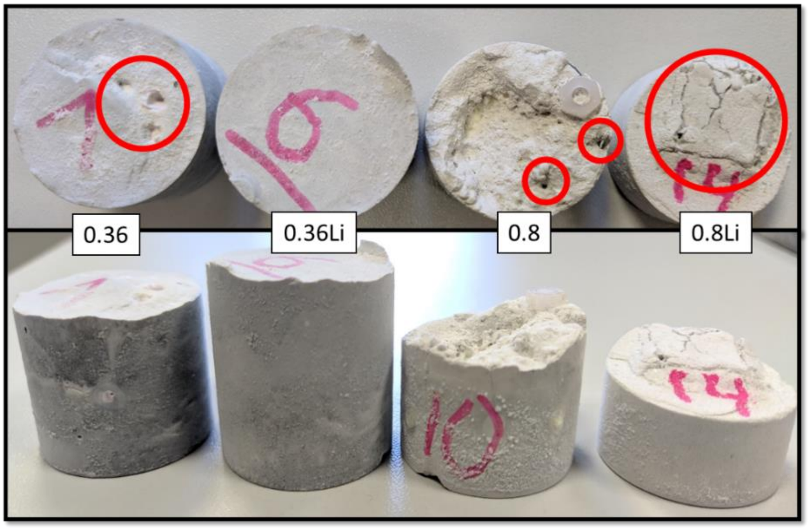

Figure 55. Static corrosion test samples after the test.

4.3.1 Gas Chromatography

The corrosion rate obtained from the GC measurements can be seen in Figure 56. High corrosion rates were calculated for samples without lithium (~ 160 µm/yr) while significantly lower corrosion rates were calculated for samples with lithium (~ 2 µm/yr and ~ 34 µm/yr for 0.36Li and 0.8Li respectively). This confirms the results previously obtained by EIS (Section 4.2) and the one related by Matsuo [13].

By comparing sample 0.36Li with 0.8Li it can also be seen that lower water-to-cement ratio causes lower corrosion rate, even if this phenomenon was not observed by comparing sample 0.36 and 0.8. This can be due to the high uncertainty on the GC measurement, mostly for samples 0.36 and 0.8. Indeed, to allow the GC measurements, gas samples needed to be diluted (see Section 3.3). Moreover, due to the huge H_2

production from samples 0.36 and 0.8, more dilution was needed to fall into the calibration curve made for the determination of the H_2 concentration. Then, the uncertainty is a lot higher for samples without lithium.

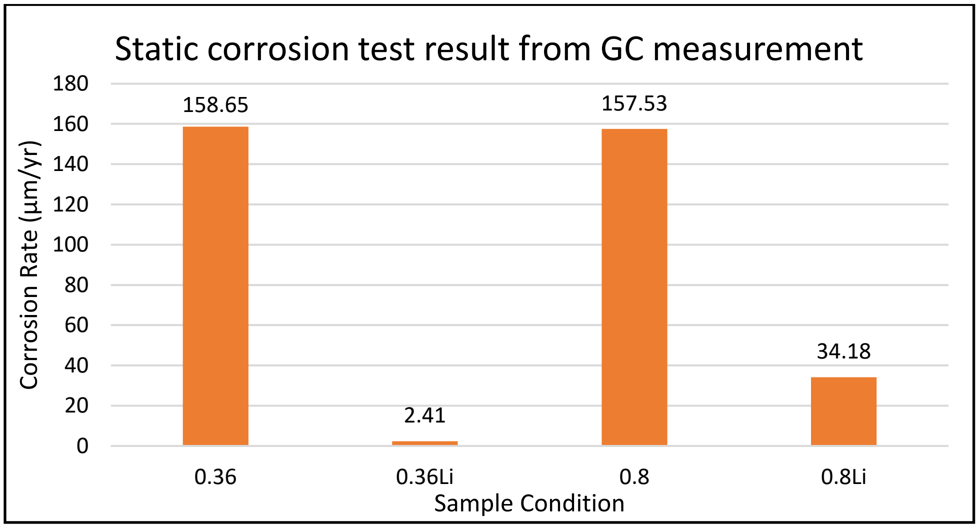

Figure 56. Corrosion rate from GC measurement.

4.3.2 Pressure Measurement

The pressure was measured by using a manometer prior to sampling of the gas phase for the GC measurement (see Section 3.3). This pressure used to calculate the number of moles of H_2 gas produced by using the ideal gas law. This number of moles was then used to calculate the corrosion rate (see Appendix F). Corrosion rate based on pressure measurements can be seen in Figure 57. The results are similar to the results obtained from GC in the previous section. The results in Figure 57 show that samples with lithium addition have a significantly lower corrosion rate (2-30 µm/yr) compared to sample without lithium (140-170 µm/yr). The pressure measurement technique has a lower uncertainty compared to GC because it doesn't need many iterations of dilution. The uncertainty in this method is the uncertainty of the manometer itself.

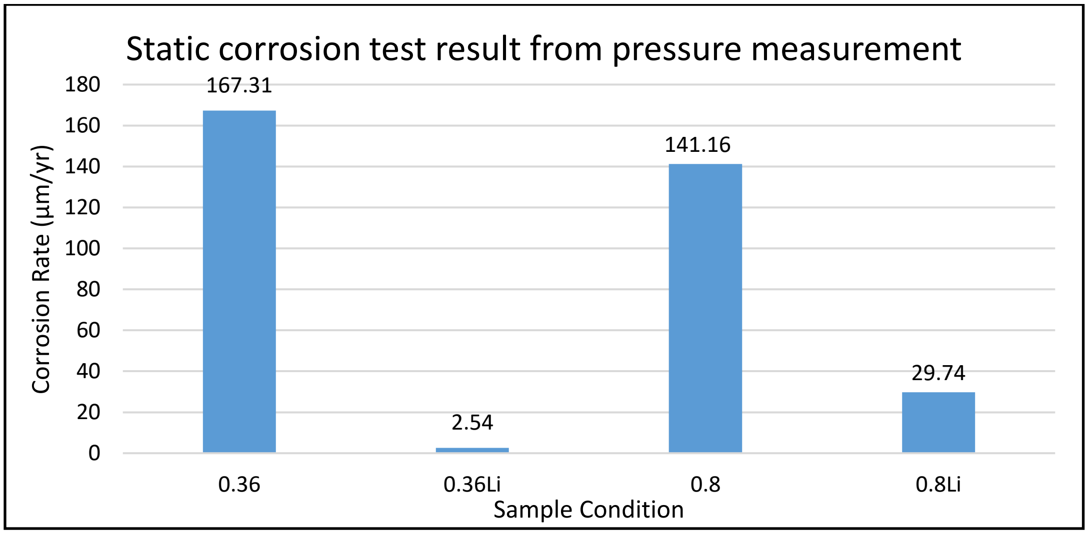

Figure 57. Corrosion rate from pressure measurement.

4.4 EIS and static corrosion test comparison

A comparison between the corrosion rates obtained from the EIS measurements and the static corrosion test is illustrated in Figure 58. The EIS corrosion rates shown on Figure 58 are the average corrosion rates taken over the total measurement period (see Figure 49) as it is also the case for the corrosion rate obtained from the GC measurement. Moreover, the cracked 0.36 is not used for sample condition 0.36. Figure 58 shows that whatever the method used, the sample that has the lowest rate of corrosion is sample 0.36Li.

There are several reasons that may explain the difference in corrosion rate obtained from the EIS measurements and the static corrosion tests:

- First, the geometry of the sample is different (see Section 3.2 and Section 3.3). This difference in geometry might have an effect on the diffusion of limewater inside the cement to reach the aluminum.
- Second, for the samples without lithium a significant increase of pressure inside a closed container was observed, while this did not occur for the EIS samples. The increase of pressure inside the container could increase the diffusion rate of limewater into the cement and accelerate the corrosion process.

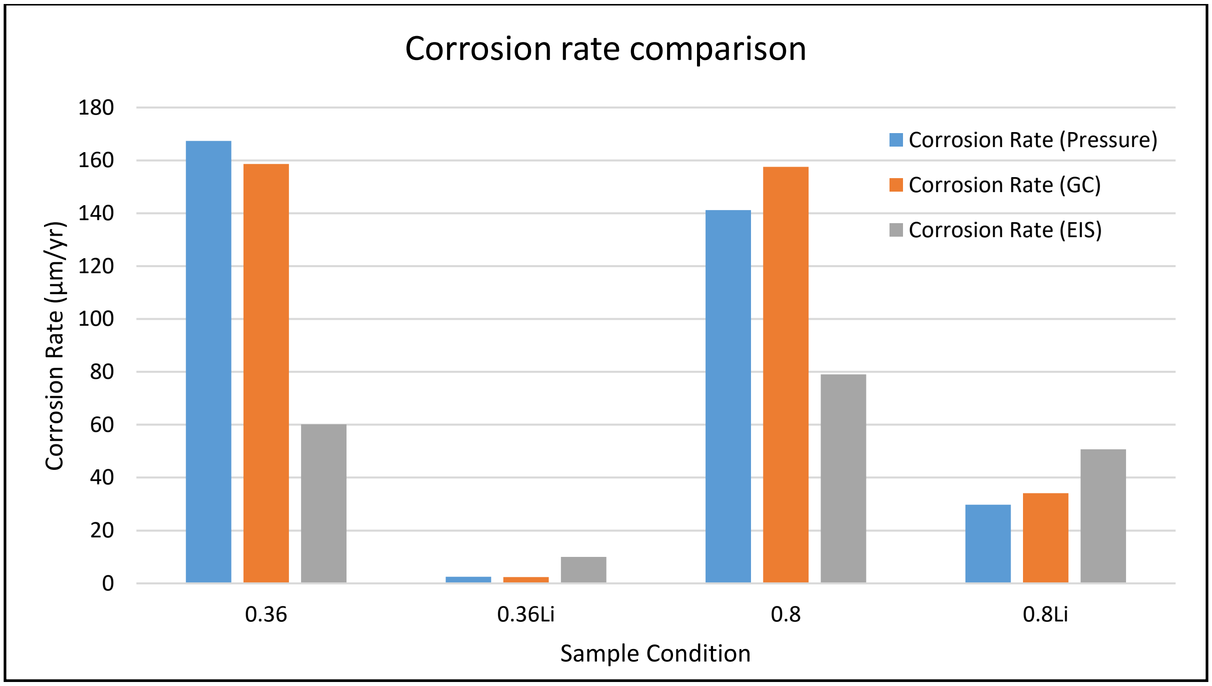

Figure 58. Corrosion rate comparison.

Even though there are some difference between EIS results and Static Corrosion test results, there are trends than can be clearly observed:

- Addition of lithium significantly decreases the corrosion rate of aluminum.
- A higher water-to-cement ratio in the cement matrices increases the corrosion rate.

CHAPTER V

SOCIO-ECONOMIC CONTEXT

The study is a real engineering case. As the study focused on BR1 fuel, it can also be used for other research reactors. This study can be used for all nuclear waste handling from aluminum cladded nuclear fuel.

The main socio-economic impact for this study is for spent fuel from BR1 reactor in Belgium (see Section 2.1). The fuel from BR1 is cladded with aluminum. The results from this study provide data for the possibility of direct cementation of BR1 spent fuel.

Currently there are more than 250 research reactors with fuels similar to the BR1 reactor (see Section 2.1) [19]. As of December 2018, the IAEA research reactor database showed that there were 226 operational research reactors (86 of them in developing countries), 9 under construction (four of these 100 MWt or more), 13 planned (11 in developing countries), 26 temporarily or in extended shutdown, 56 permanently shut down, and 510 decommissioned or undergoing decommissioning. Most of these research reactors use aluminum clad. This study is of benefit for the waste handling of all the aluminum cladded nuclear fuel waste.

France is currently building the Jules Horowitz research Reactor (JHR) [20]. The Jules Horowitz research Reactor (JHR), a project conducted by the CEA Nuclear Energy Division, is an answer to a key technological and scientific challenge: testing fuel and material behaviour under irradiation in support of current and future nuclear reactors. JHR, currently under construction at the CEA Cadarache site, will represent in Europe a unique experimenting tool available to nuclear power industry, research institutes, nuclear regulatory authorities and their technical supports. It will also ensure the production of radioelements for nuclear medicine and non-nuclear industry.

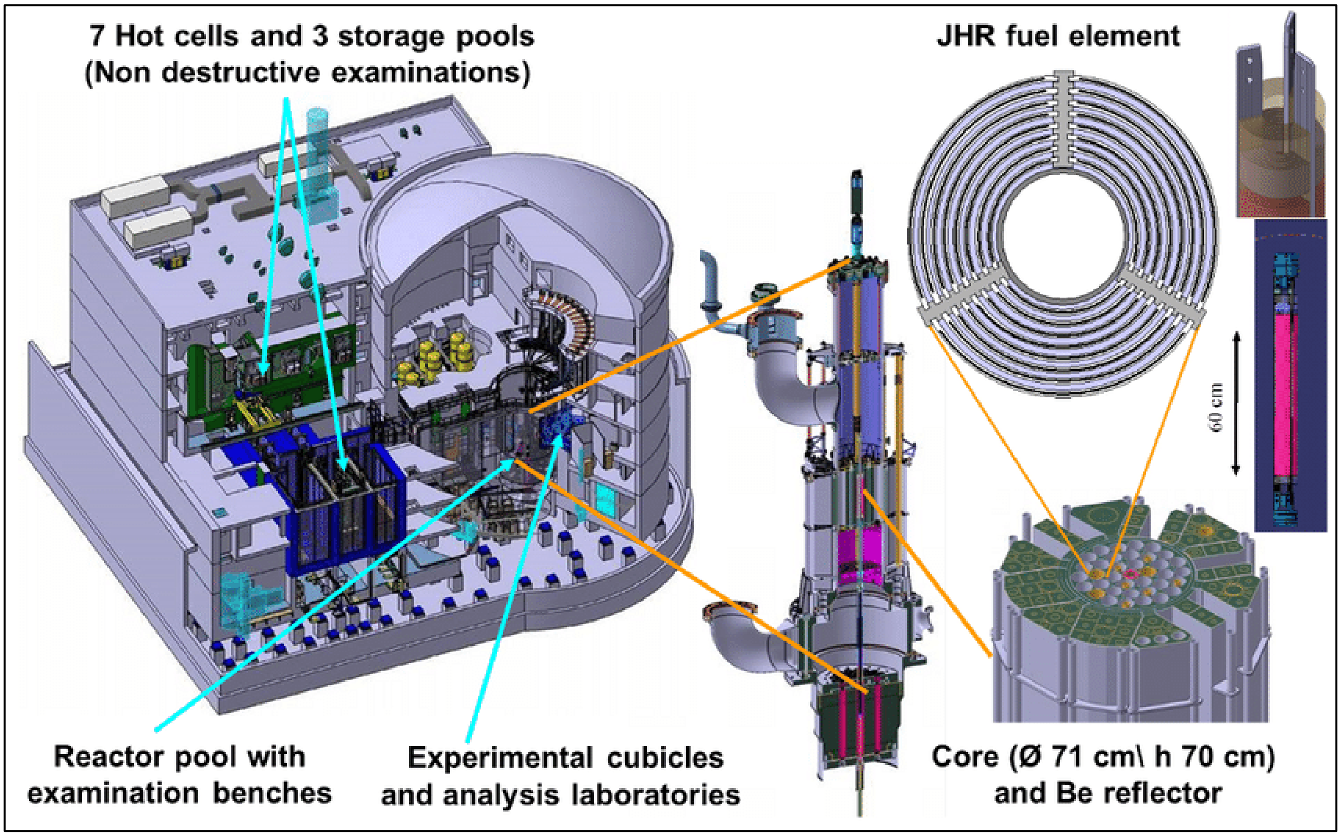

Figure 59. Jules Horowitz Reactor *[20]*.

JHR will use aluminum clad in the fuel. Spent fuel from JHR will also be stored in the future. One of the options for spent fuel management is direct emplacement in a cementitious matrix (see Section 2.1). This study is relevant to provide information regarding JHR spent fuel management.

In 2006, 105 m^3 of aluminum cladded spent fuels were removed from research reactors in the USA (see Figure 60) [21]. The volume of spent fuel increases by 7.2 m^3 per year. As for JHR and BR1, the spent fuels could be treated with direct emplacement in a cementitious matrix. This study is able to provide data and information for these research reactors in the USA.

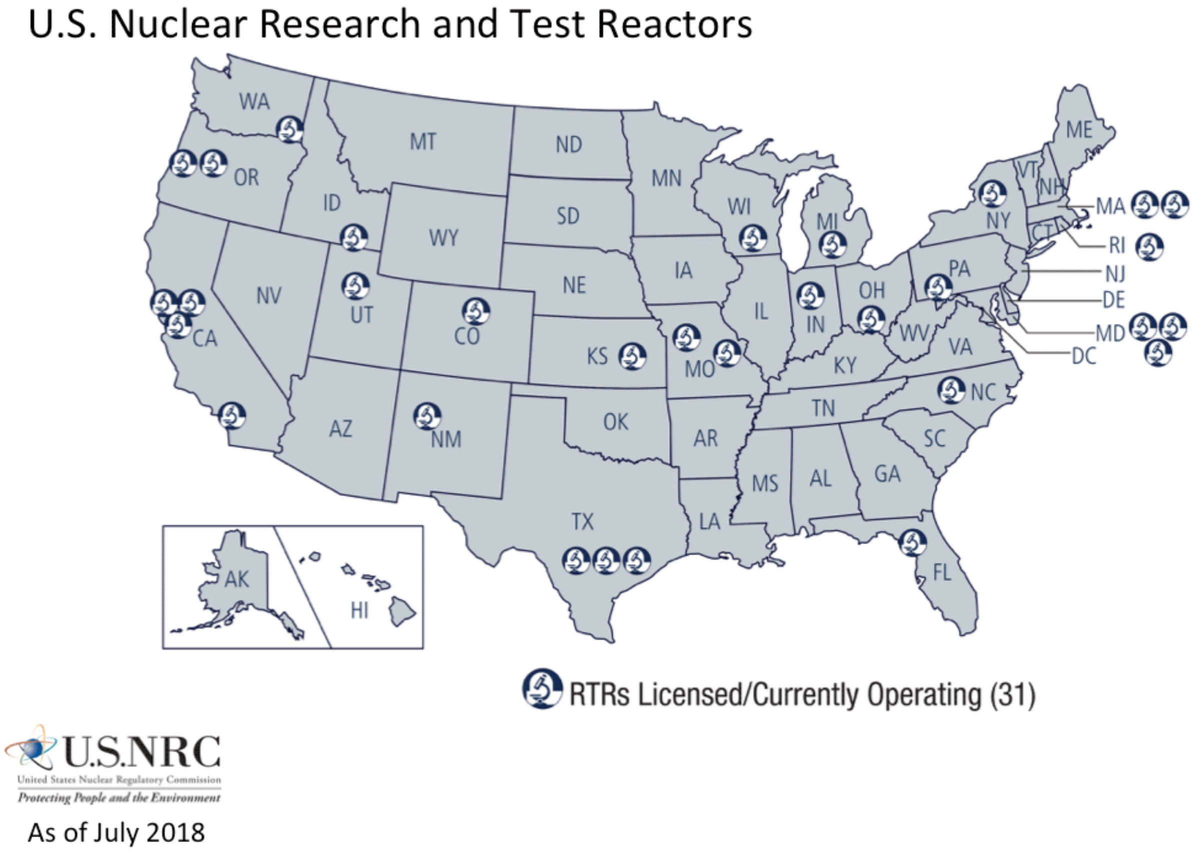

Figure 60. U.S. Nuclear research and test reactors.

This study provides preliminary results for a way to handle the spent fuel management from research reactors. This report is a preliminary study giving information on the behavior of aluminum in contact with water saturated OPC cement. This should increase the use of research reactors in daily life. The uses of research reactors are [22]:

- Materials research: The development and usage of new complex materials with improved properties and functionalities to provide solutions to major modern engineering challenges
- Neutron activation analysis: a method for the qualitative and quantitative determination of elements based on the measurement of characteristic radiation from radionuclides formed by irradiating materials by neutrons.
- Neutron imaging: a non-destructive technique for analyzing the structure of a sample. The basic principle is similar to that of X ray radiography: a beam of neutrons passes through the sample and is attenuated in accordance with the sample's composition or its geometrical form.
- Radioisotope production: Radiopharmaceuticals, such as those extracted from radioisotope generators, are substances that contain a radioisotope and have the ability to perform the role of marker in medical diagnostic or therapeutic procedures. Eighty per cent of all diagnostic medical scans worldwide rely on the availability of the radioisotope molybdenum-99 (^{99}Mo) and its daughter product, Technetium-99m (^{99}mTc), which are presently only produced at research reactors.

Socio-economic impacts of research reactors are:

- Material research in a research reactor has significantly improved the understanding in such areas as condensed matter physics and chemistry, nanotechnology, polymer science, life science, sustainable energy research, sensors and smart materials, biotechnology, engineering and archaeology.
- The samples that can be analyzed with neutron activation analysis benefit a number of different fields, including medicine, nutrition, biology, chemistry, forensics, the environment and mining.
- Neutron imaging allows determination of hydrogen in electrochemistry analyses of fuel cells, dynamic efficiency and performance study of batteries or engines, applications in car, aviation and building industry for quality control of various objects, non-invasive study of cultural heritage objects and biological samples, applications in geology and soil physics, non-destructive examination of nuclear fuel and its cladding, investigation of several aspects of materials research.
- Research reactors and accelerators are also used to develop new radioisotopes for diagnostics and therapy in nuclear medicine, non-destructive testing and radiotracer industrial applications, as well as for radiotracer studies in scientific research. Globally, the number of medical procedures involving the use of radioisotopes is growing, with an increasing emphasis on radionuclide therapy using radiopharmaceuticals for the treatment of cancer. These socio-economic benefits, as well as the effective quality control processes and cleaner environments provided by supporting technology, strengthen the national, regional and international capabilities of research reactor facilities.

Production of radioisotopes in research reactor is very important. Even though there is a rising sentiment against nuclear power, there is always a need for research reactors. The reactors that could supply radioisotopes can be seen in Figure 60 and Figure 61 [23]. Reactors that produce radioisotopes will most likely use aluminum cladding for their nuclear fuels, meaning that this study will be relevant to support the waste management of the reactors indicated in Figure 60 and Figure 61.

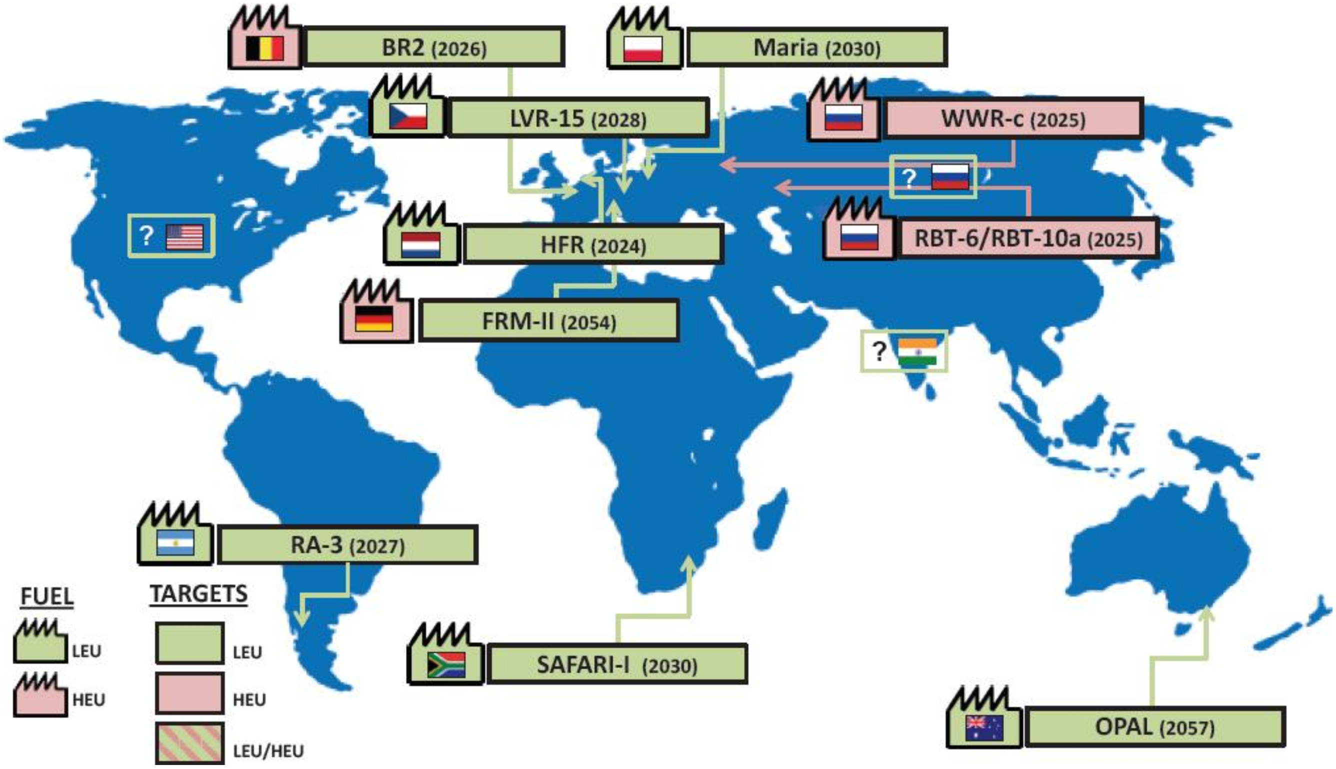

Figure 61. Speculative map of Mo-99 supply in 2020 [23].

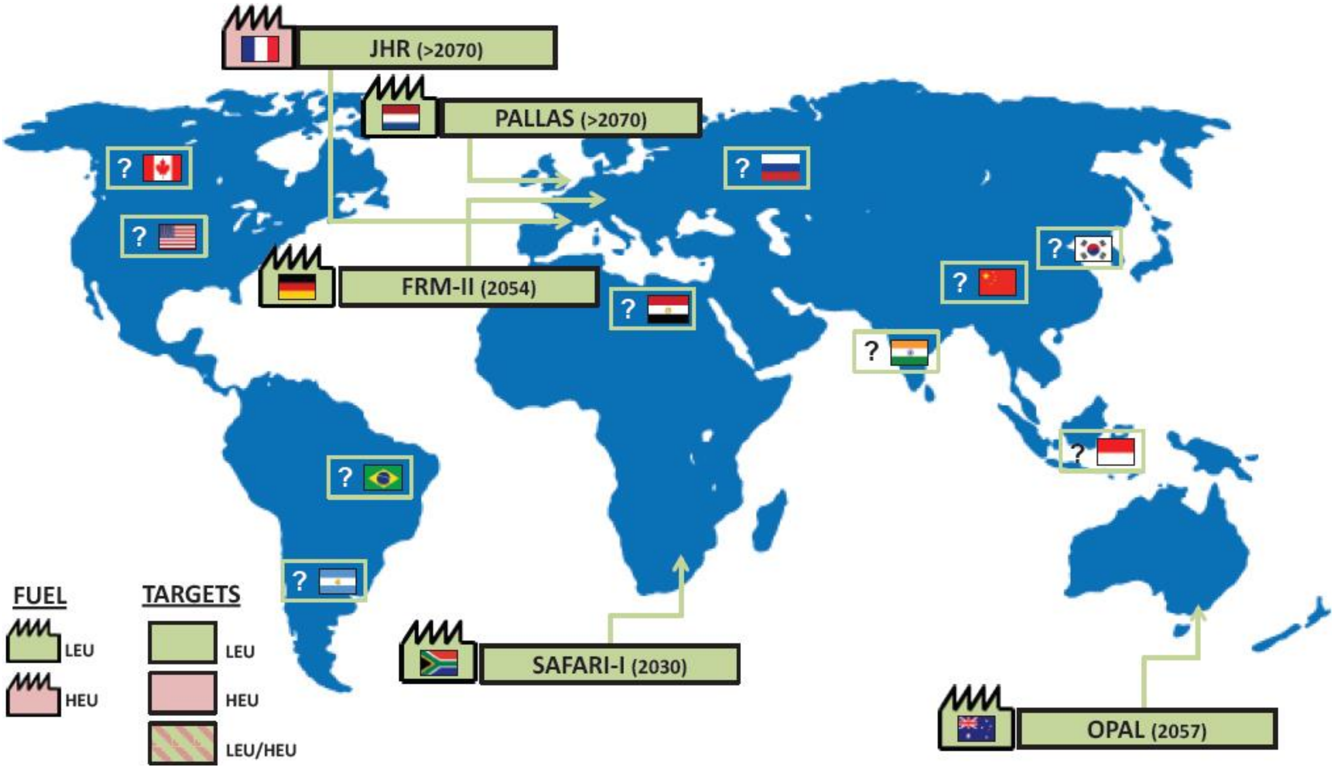

Figure 62. Speculative map of Mo-99 supply in 2030 [23].

In conclusion, the socio-economic impact for this study is to provide data and information about spent fuel management of research reactors such as BR1 and JHR. The socio-economic impacts from this study are the socio-economic impacts of research reactors, which are materials research, neutron activation analysis, neutron imaging, and radioisotope production. The socio-economic impact of this study is important for current and future research reactors and will not decrease in the future because of the need of radioisotopes.

CHAPTER VI

CONCLUSIONS

5.1 Summary

- Higher water-to-cement ratio results in more porous cement matrices.
- The corrosion of aluminum is high at the beginning but decreases over time along the measurement period.
- Addition of lithium is able to significantly decrease the corrosion rate.
- Higher water-to-cement ratio results in higher initial corrosion rate because more water is available to corrode the aluminum.
- More porous cement matrices result in a higher corrosion rate because of higher diffusion rate of limewater inside the cement to reach the aluminum.
- Higher water-to-cement ratio and more porous cement matrices reduce the effectivity of lithium for decreasing the corrosion rate.
- Cement with 0.36 water-to-cement ratio with 3 wt.% lithium addition achieved the lowest corrosion rate of metallic aluminum embedded in a cement matrix.

5.2 Future Improvements

This research provides preliminary results on the relatively slow corrosion rate of aluminum embedded in a low porous cement matrix containing 3wt% $LiNO_3$. Although promising, the conclusion of this work can in no way be considered as a decision for direct embedding of Al cladded metallic U nuclear fuel into the said cement matrix. Indeed, before such a decision can be taken, a much larger R&D programme needs to be performed, studying, among others, the corrosion rate of the metallic U in the said cement matrix, the corrosion rate of the metallic U – Al after re-saturation of the cement matrix and in accidental conditions (direct exposure of metallic U – Al to water as a result of a fissure). Future tests should be done to provide more data. Improvements for further research are:

- Decrease the pH of the cement [12]. This can be done by adding pozzolanic materials such as silica fume into the cement mix [24]. Future tests using silica fume in the cement mix should be done. This can also be done by using MKP (magnesia phosphate) cement [8].
- Future experiments could study the very low water-to-cement ratio. The corrosion rate of aluminum exposed to cement mixes decreases with lowering the water-to-cement ratio. Živica studied water-to-cement ratio as low as 0.075 [25]. Lower water-to-cement ratio will mean stronger cement but more brittle, while producing less H_2 and corrosion product. Mechanical testing for cement strength and brittleness should be performed.
- Usage of other types of cement to reduce the corrosion of aluminum. MKP cement [8] and CAC cement [12] were some of the cements proposed, but they are not commonly used cements which means their price will be higher compared to OPC. Future study could use Blast Furnace Slag (BFS), which has a lower pH than OPC, or Super Sulphate Cement (SSC), which has an excess of sulphate to promote formation of ettringite and reduce aluminum corrosion [12].

- Future studies could study the addition of sulphatic salt(s) to induce formation of ettringite to reduce aluminum corrosion [12]. The synergistic inhibiting effect of adding sulphatic salt and $LiNO_3$ simultaneously could also be studied.
- Study the reason why cements crack. Cracks could be the result of H_2 gas produced from the corrosion process or of the expansion caused by corrosion products inside the cement.
- Change the limewater every week to simulate flowing water conditions. It is better if the limewater used as immersion solution is controlled at a certain volume for every sample. Measurement of dissolved aluminum and lithium in the limewater should also be done using Atomic Absorption Spectroscopy (AAS) or Inductively coupled plasma mass spectrometry (ICP-MS). Measurement of solution pH should also be measured.
- Perform Scanning Electron Microscope (SEM) and Energy Dispersive X-Ray Spectroscopy (EDS) analysis. SEM and EDS analysis will provide more information about the surface corrosion and passive layer formation in the aluminum surface.

BIBLIOGRAPHY

[1] [Online]. Available: http://science.sckcen.be/en/facilities/br1. [Accessed 8 April 2019].

[2] A. Leenaers and S. V. d. Berghe, "MICROSTRUCTURE OF 50 YEAR OLD SCK•CEN BR1 RESEARCH," *THE RERTR-2007 INTERNATIONAL MEETING ON REDUCED ENRICHMENT FOR RESEARCH AND TEST REACTORS,* 2007.

[3] [Online]. Available: https://www.sckcen.be/en/About/Introduction. [Accessed 8 April 2019].

[4] F. Druyts and S. Caes, "Corrosion of metals in category B&C waste in highly alkaline and anoxic conditions," 2017.

[5] "Cement," in *Building Materials in Civil Engineering,* Woodhead Publishing, 2011, pp. 46-80.

[6] J. L. G. Calvo, "Study of the Microstructure Evolution of Low-pH Cements Based on Ordinary Portland Cement (OPC) by Mid- and Near-Infrared Spectroscopy, and Their Influence on Corrosion of Steel Reinforcement," *Materials,* 2013.

[7] G. Goracci, "Dynamics of nano-confined water in Portland cement - comparison with synthetic C-S-H gel and other silicate materials," *Scientific reports,* vol. 7, no. 1, p. 8258, 2017.

[8] S. Delpech, "Kinetic Model of Aluminum Behavior in Cement-Based Matrices Analyzed by Impedance Spectroscopy," *Journal of The Electrochemical Society,* 2017.

[9] U. Nürnberger, "Corrosion of metals in contact with mineral building materials," *Otto-Graf-Journal,* vol. 12, 2001.

[10] O. Adetunji, "Corrosion Resistance of Aluminum Plates in Lime Solution," *The Pacific Journal of Science and Technology,* vol. 12, no. 1, pp. 56-61, 2011.

[11] A. Setiadi, "Corrosion of aluminum and magnesium in BFS composite cements," *Advances in Applied Ceramics,* vol. 105, pp. 191-196, 2006.

[12] H. Kinoshita, "Corrosion of aluminium metal in OPC- and CAC- based cement matrices," *Cement and Concrete Research,* vol. 50, pp. 11-18, 2013.

[13] T. Matsuo, "LiNO3 Addition to Prevent Hydrogen Gas GEneration from Cement-Solidified Aluminum Wastes," *Journal of NUCLEAR SCIENCE and TECHNOLOGY,* vol. 32, no. 9, pp. 912-920, 1995.

[14] T. Matsuo, "Effect of LiNO3 on Corrosion Prevention of Aluminum Wastes after Their Land Disposal," *Journal of Nuclear Science and Technology,* vol. 33, pp. 852-862, 1996.

[15] SCK•CEN, "Measurement of uniform corrosion rate," in *Uniform corrosion rate of carbon steel*, p. 81.

[16] "Basics of Electrochemical Impedance Spectroscopy," [Online]. Available: https://www.gamry.com/application-notes/EIS/basics-of-electrochemical-impedance-spectroscopy/. [Accessed 2015 April 2019].

[17] L. Fan, "The study of industrial aluminum alloy as anodes for aluminum-air batteries in alkaline electrolytes," *Journal of The Electrochemical Society,* vol. 163, no. 2, pp. A8-A12, 2016.

[18] C. Vargel, Corrosion of Aluminum, ELSEVIER, 2004.

[19] [Online]. Available: https://www.world-nuclear.org/information-library/non-power-nuclear-applications/radioisotopes-research/research-reactors.aspx. [Accessed 26 July 2019].

[20] [Online]. Available: http://www.cea.fr/english/Pages/research-areas/nuclear-energy/jules-horowitz-research-reactor-JHR.aspx. [Accessed 26 July 2019].

[21] J. G. Marques, "Radioactive Waste from Research Reactor Operation and Decommissioning.:," *Radioactive Waste: Sources, Types and Management (ISBN 978-1-62100-188-1),* pp. 41-76, 2012.

[22] [Online]. Available: https://www.iaea.org/topics/research-reactor-applications. [Accessed 26 July 2019].

[23] [Online]. Available: https://www.nap.edu/read/24909/chapter/8#31. [Accessed 26 July 2019].

[24] [Online]. Available: http://cement08.in2p3.fr/Presentation%20Workshop%20pour%20site%20web/Monday13/PM/Cau_Dit_Coumes.pdf. [Accessed 8 April 2019].

[25] V. Živica, "Effects of the very low water/cement ratio," *Construction and Building Materials,* vol. 23, no. 12, pp. 3579-3582, 2009.

APPENDIX

APPENDIX A

EIS MEASUREMENT RESULTS

The format used to describe the samples in the appendix is “water-to-cement_ratio_series_Days”, for example: 0.3Li_1_Day1 is the tag of sample with 0.36 water-to-cement ratio plus lithium from series 1 taken at Day 1 of measurement and 0.8_4_Day35 is the tag of sample with 0.8 water-to-cement ratio without lithium from series 4 taken at Day 35 of measurement period.

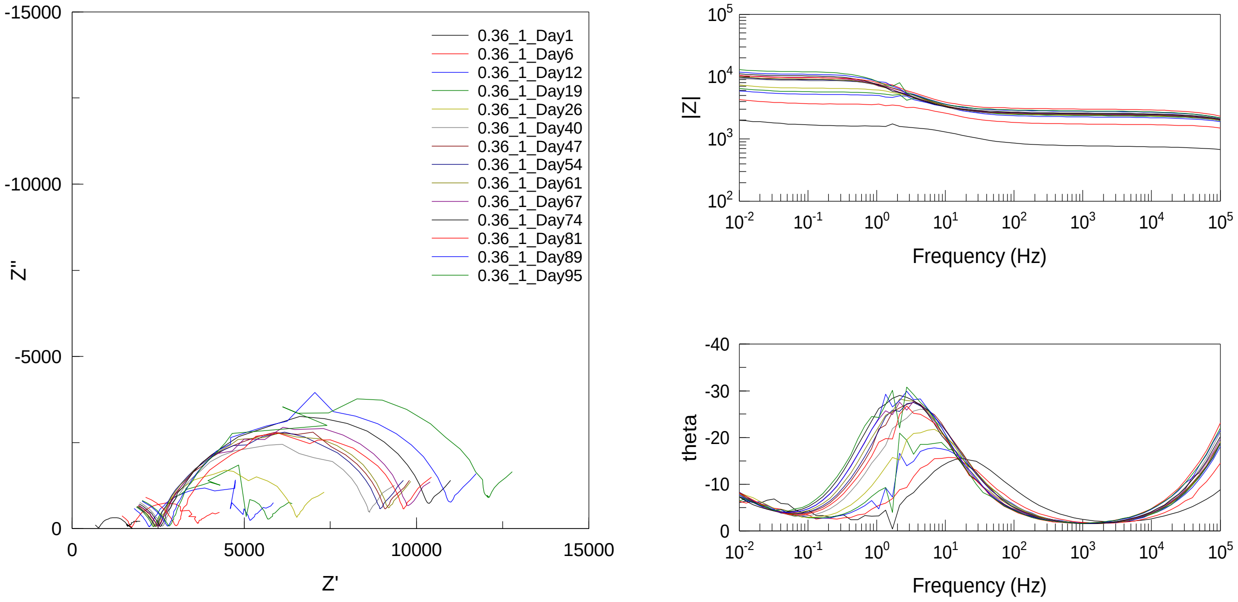

Appendix 1. EIS measurement result 0.36_1

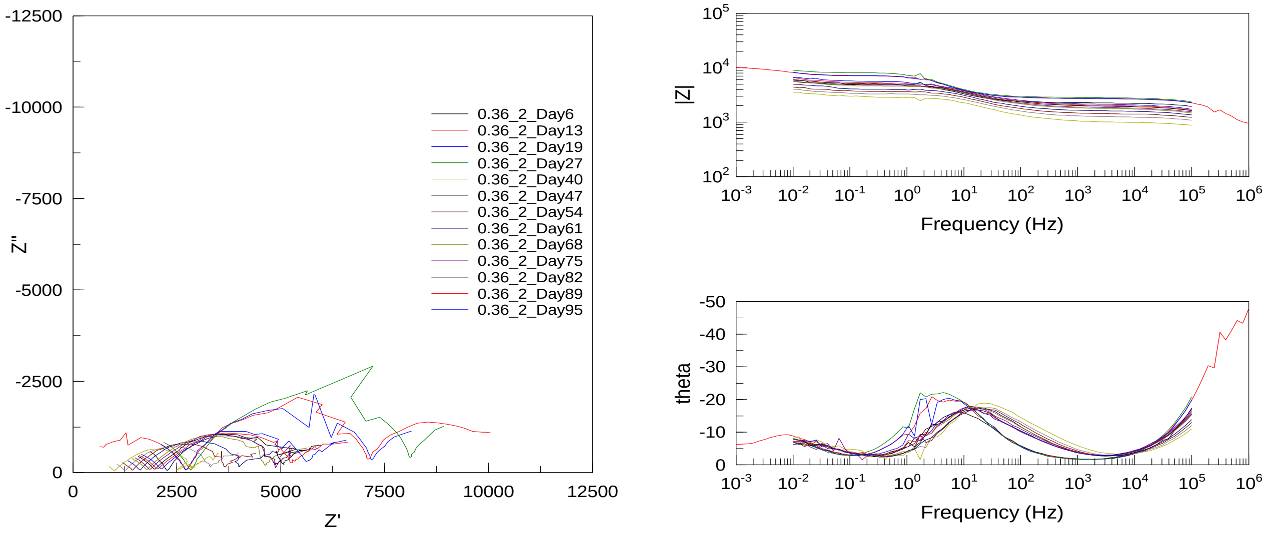

Appendix 2. EIS measurement result 0.36_2

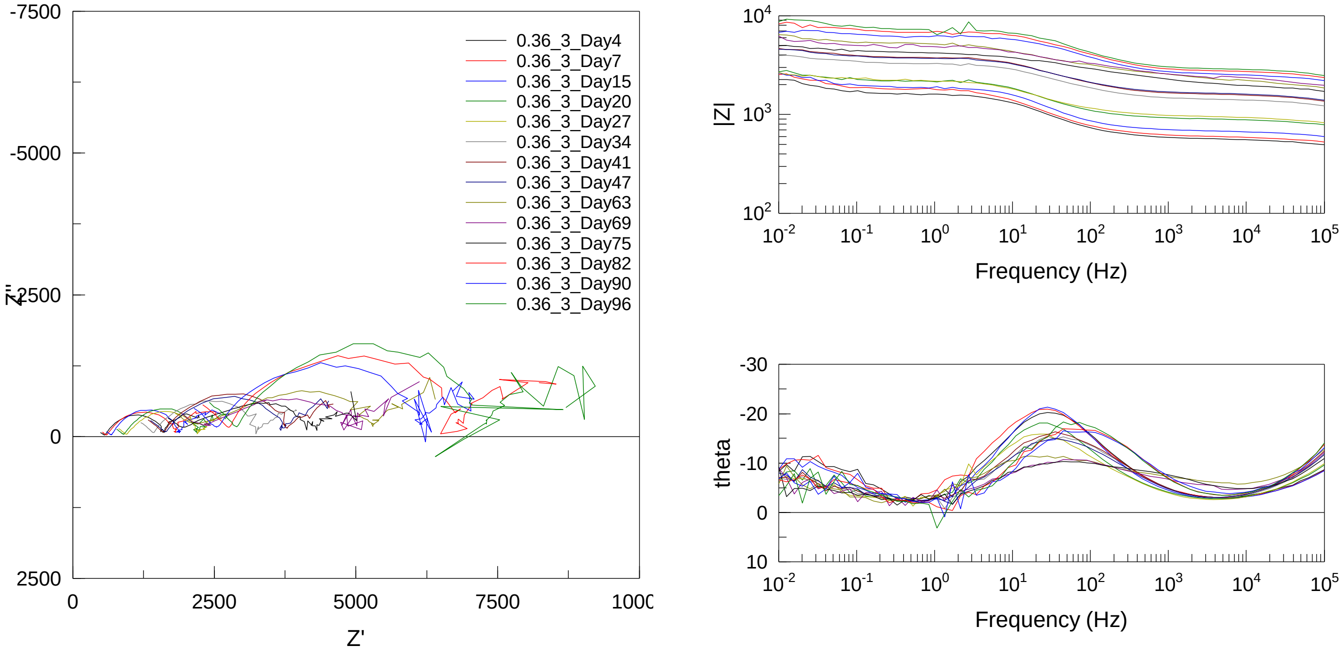

Appendix 3. EIS measurement result 0.36_3

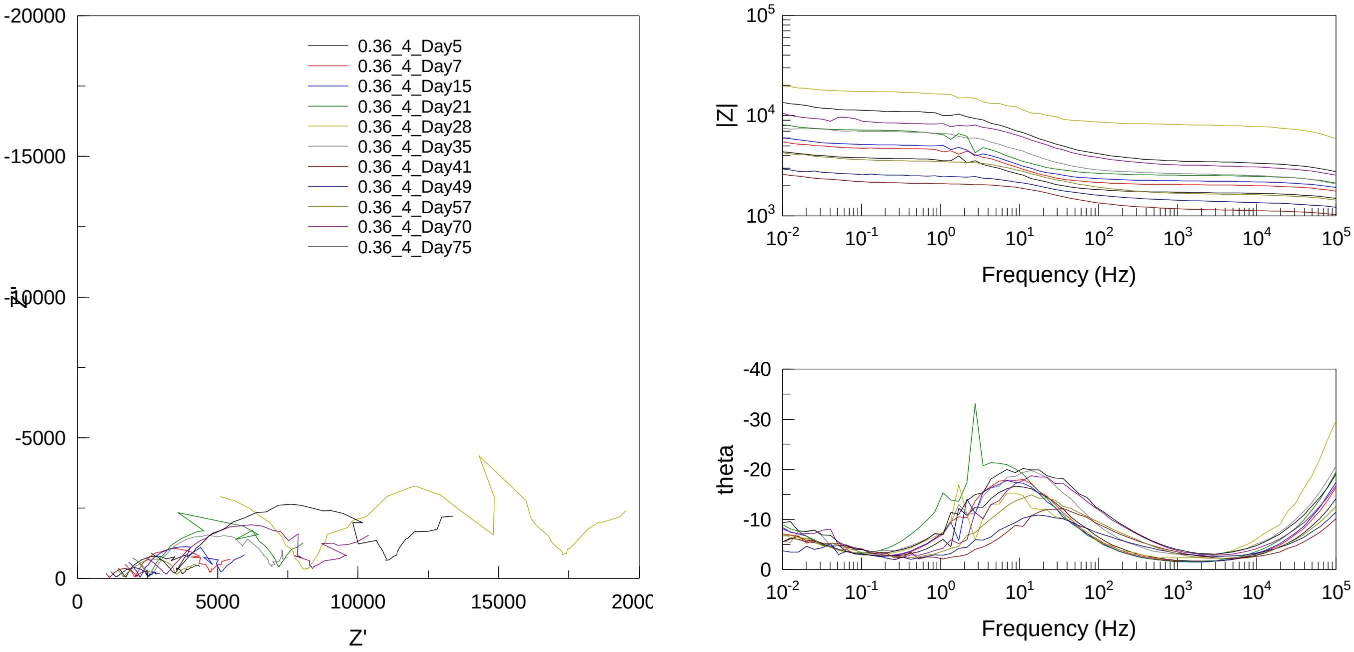

Appendix 4. EIS measurement result 0.36_4

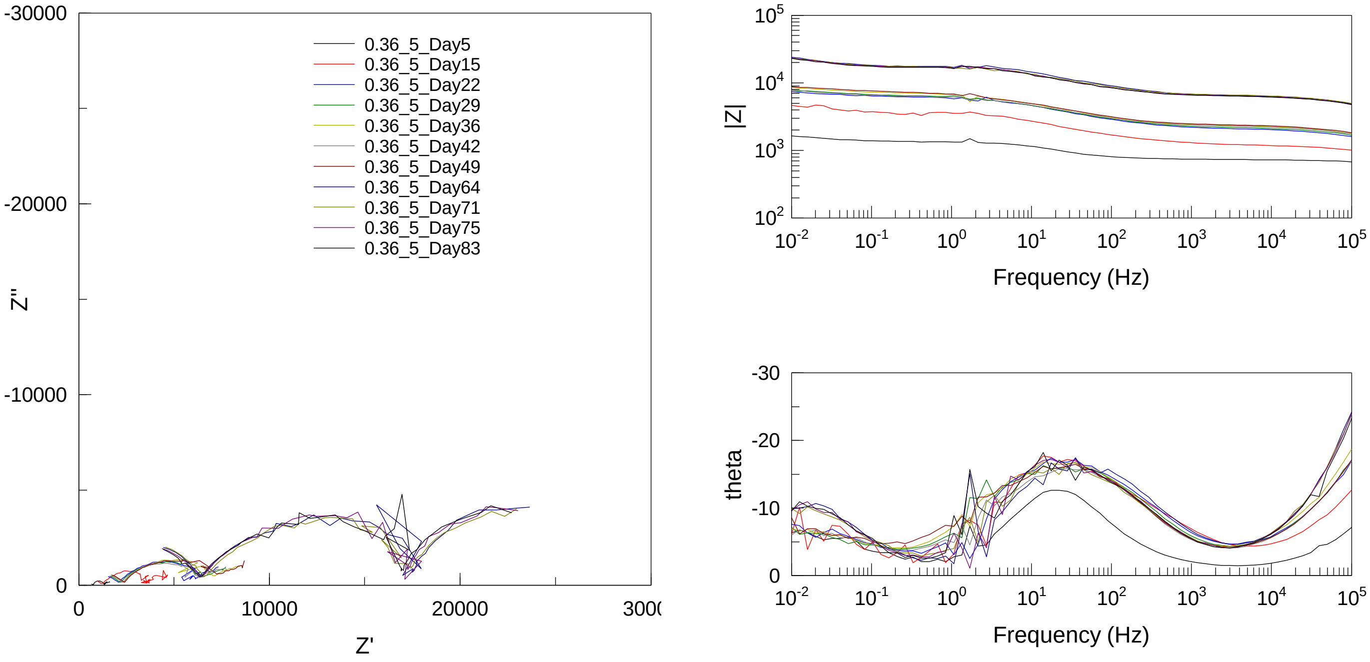

Appendix 5. EIS measurement result 0.36_5

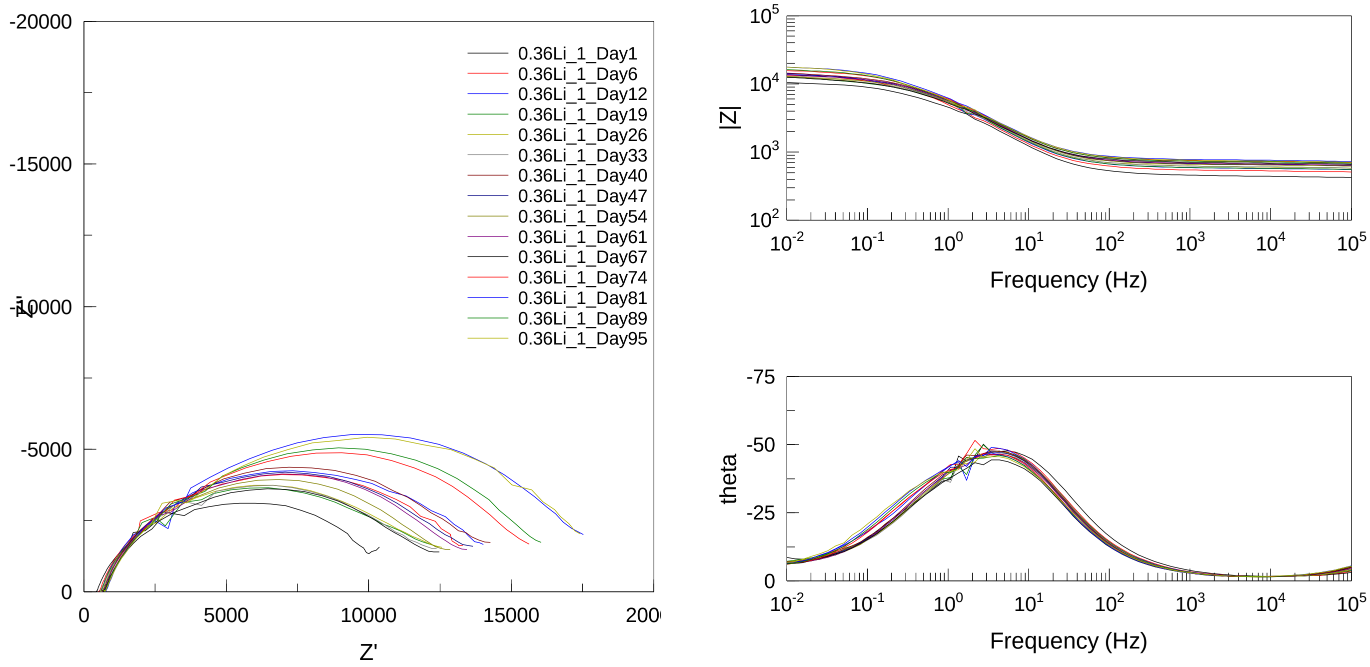

Appendix 6. EIS measurement result 0.36Li_1

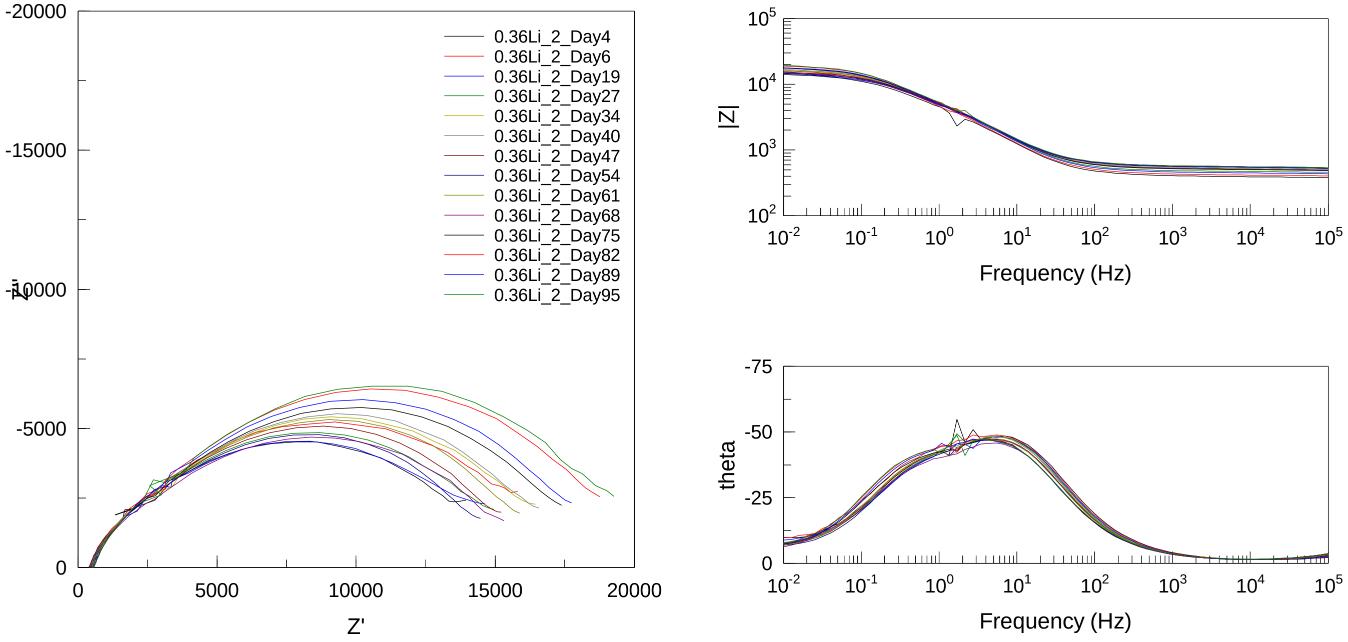

Appendix 7. EIS measurement result 0.36Li_2

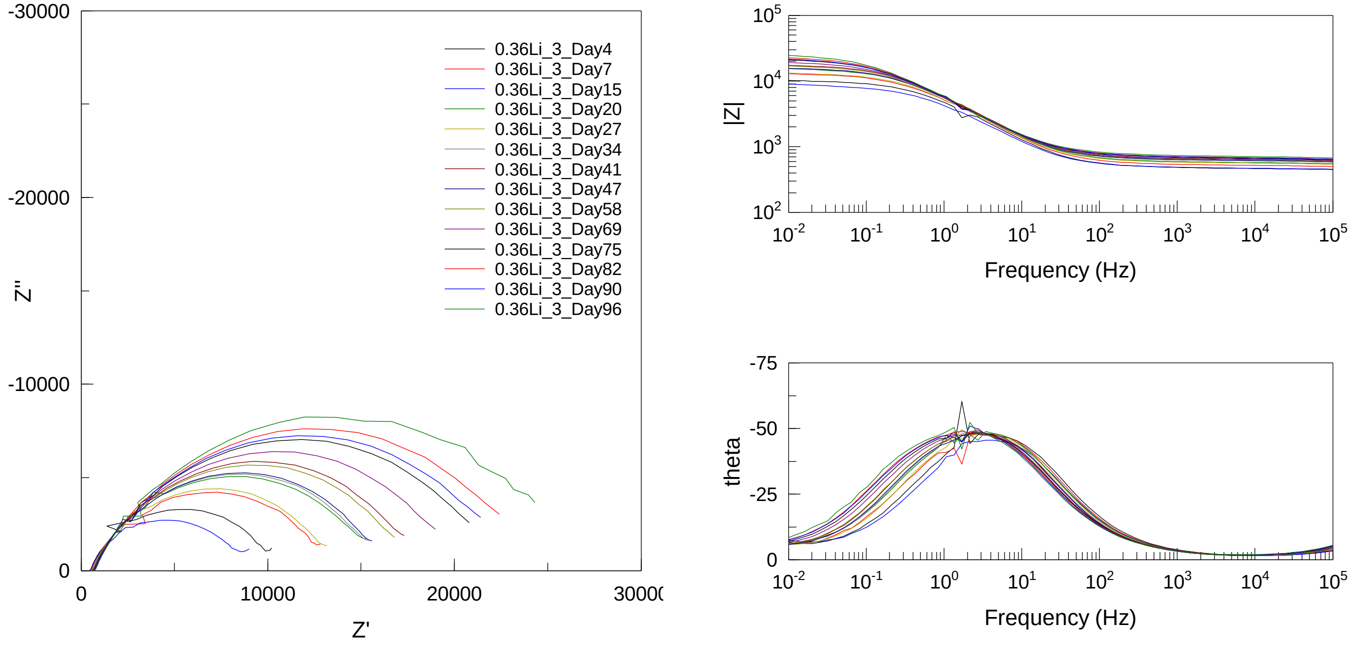

Appendix 8. EIS measurement result 0.36Li_3

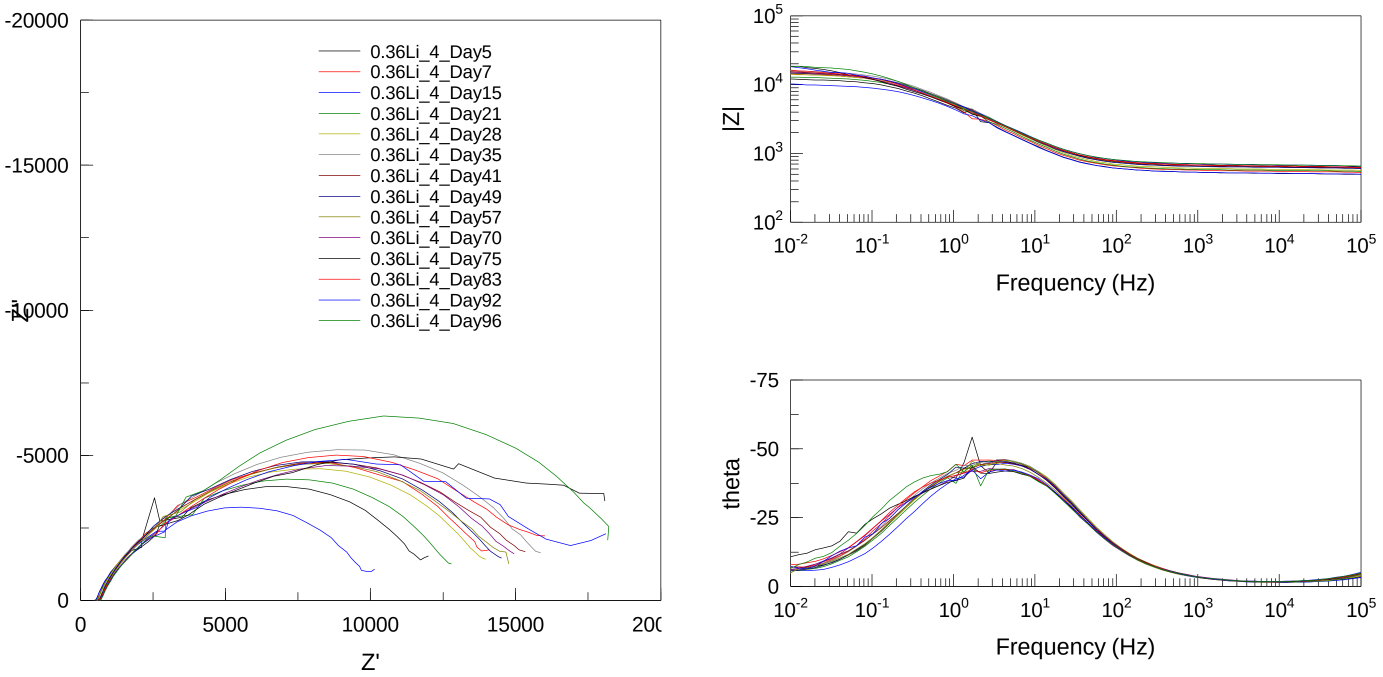

Appendix 9. EIS measurement result 0.36Li_4

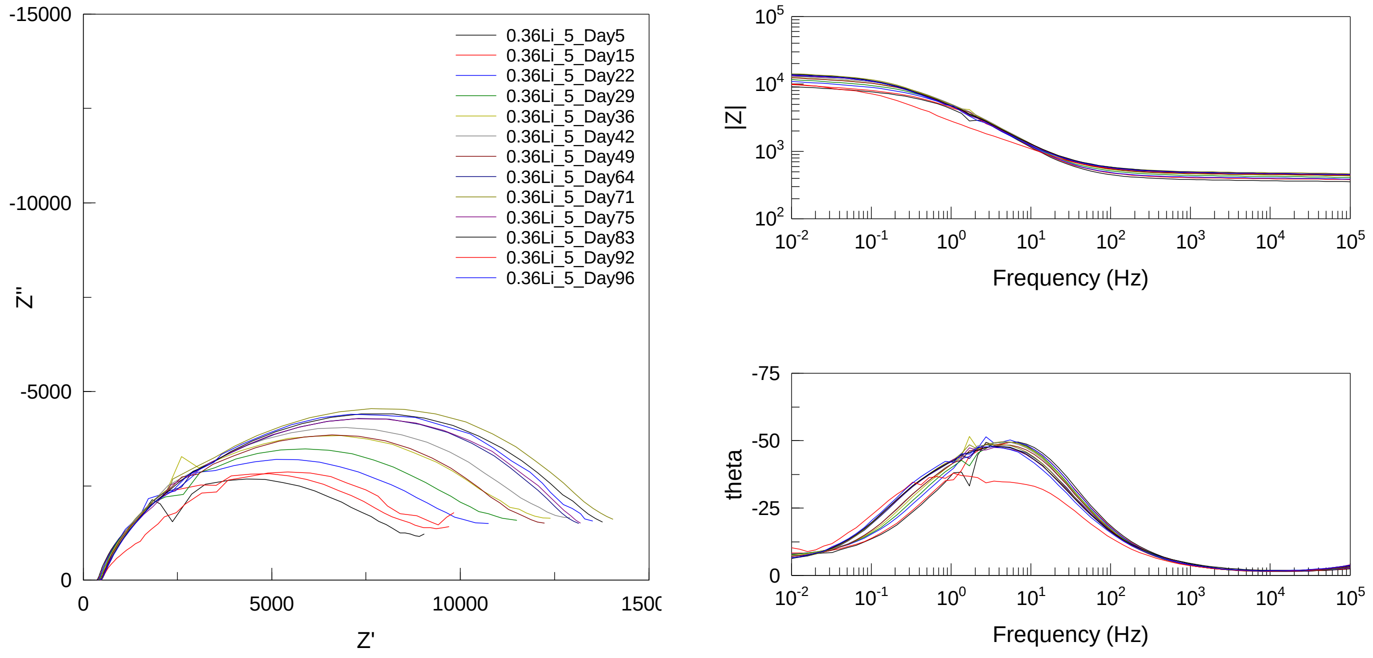

Appendix 10. EIS measurement result 0.36Li_5

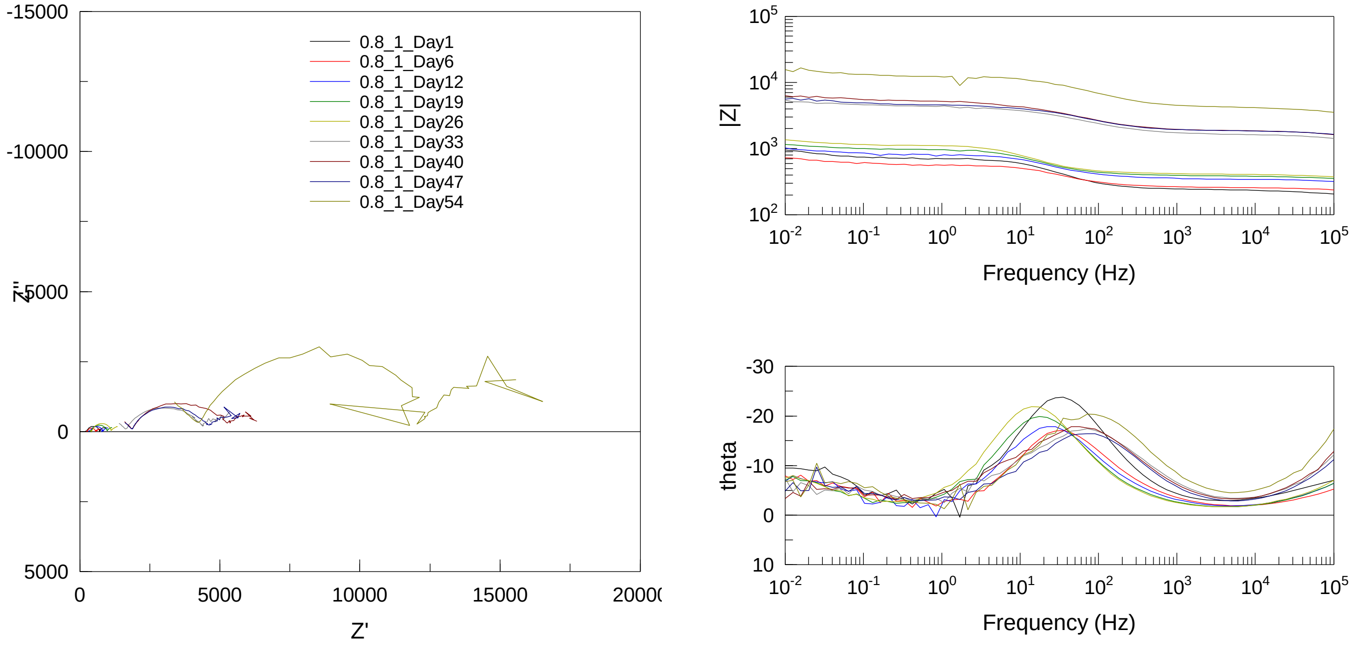

Appendix 11. EIS measurement result 0.8_1

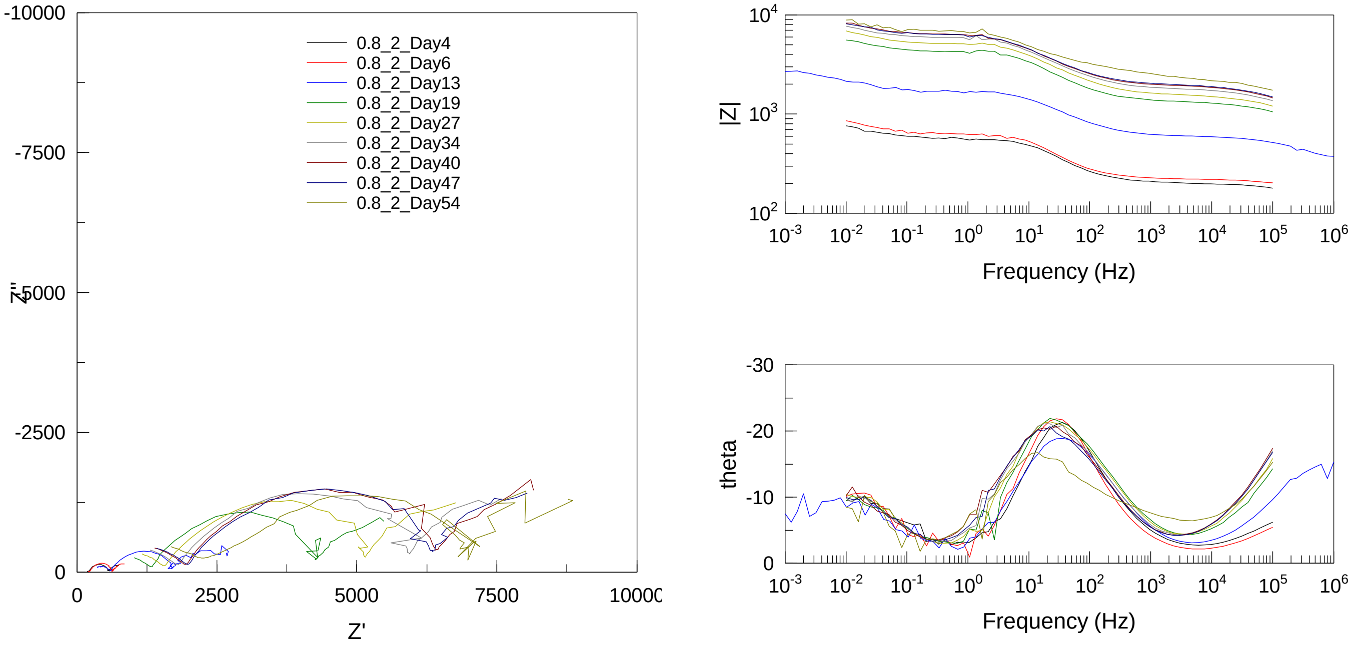

Appendix 12. EIS measurement result 0.8_2

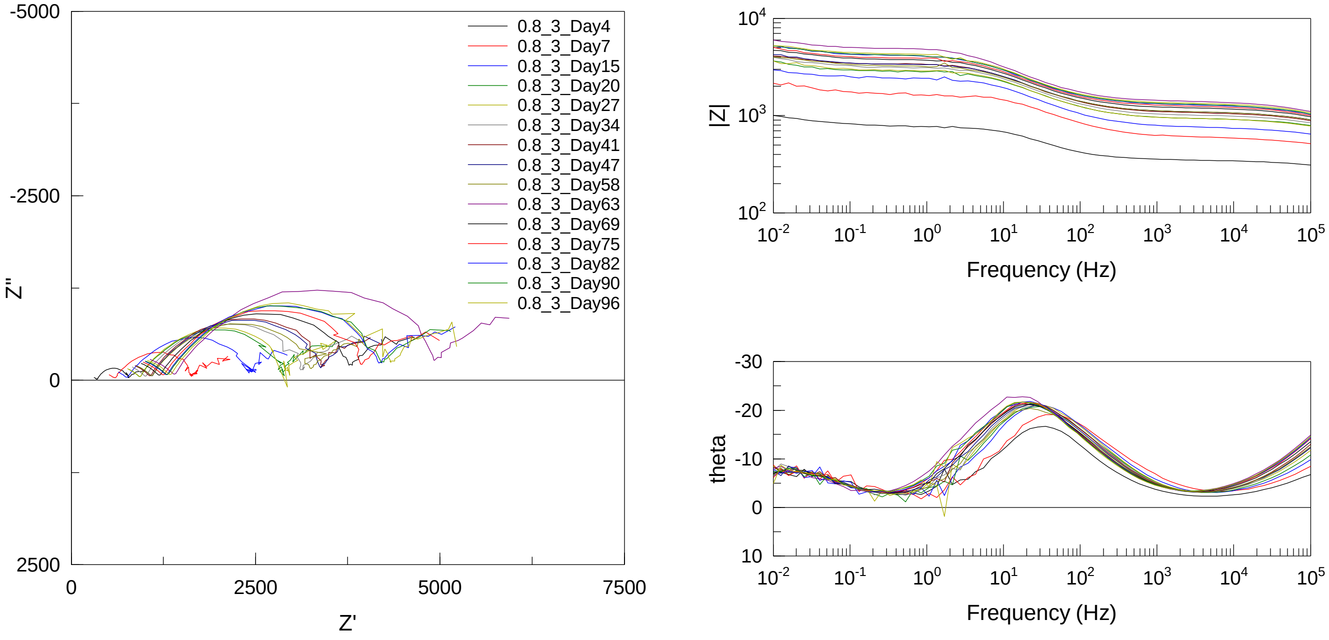

Appendix 13. EIS measurement result 0.8_3

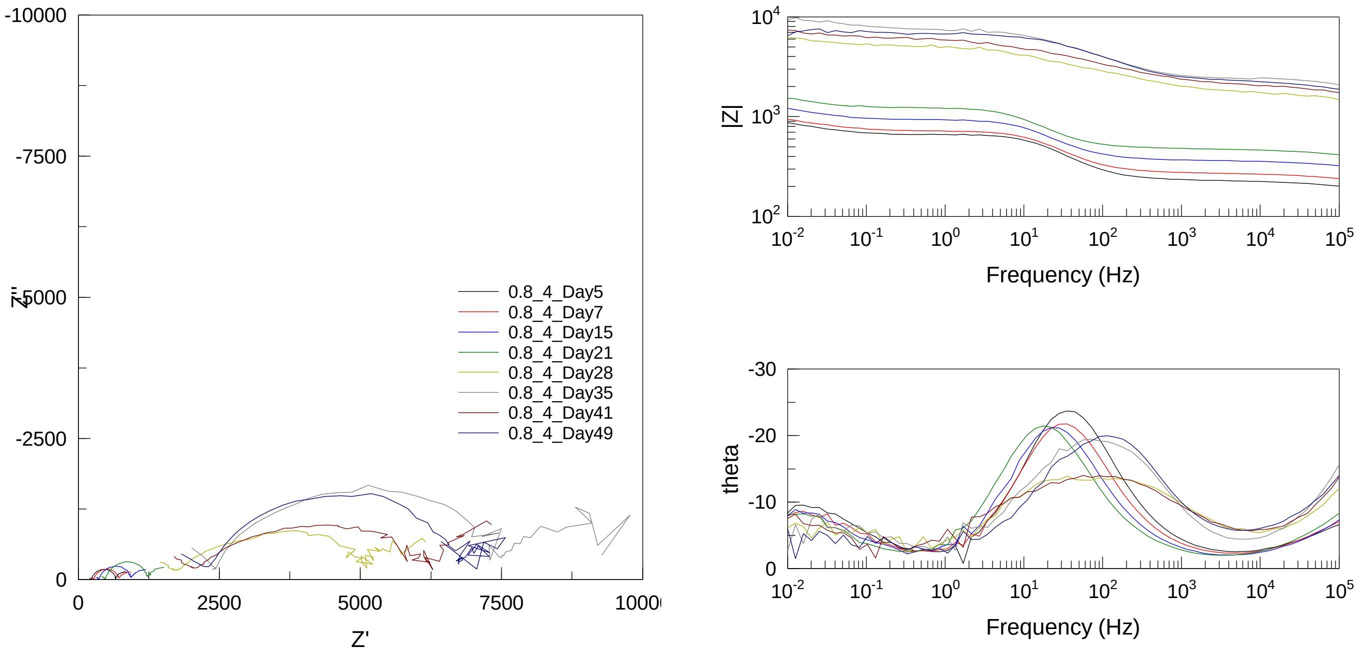

Appendix 14. EIS measurement result 0.8_4

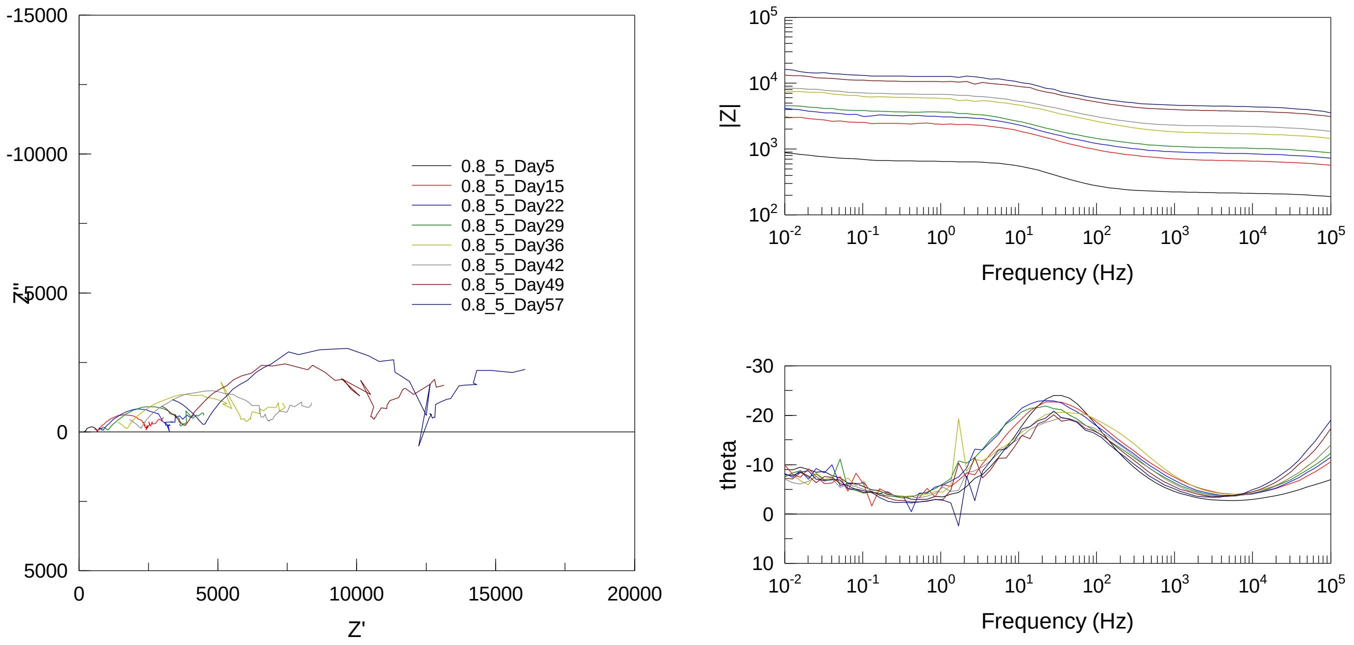

Appendix 15. EIS measurement result 0.8_5

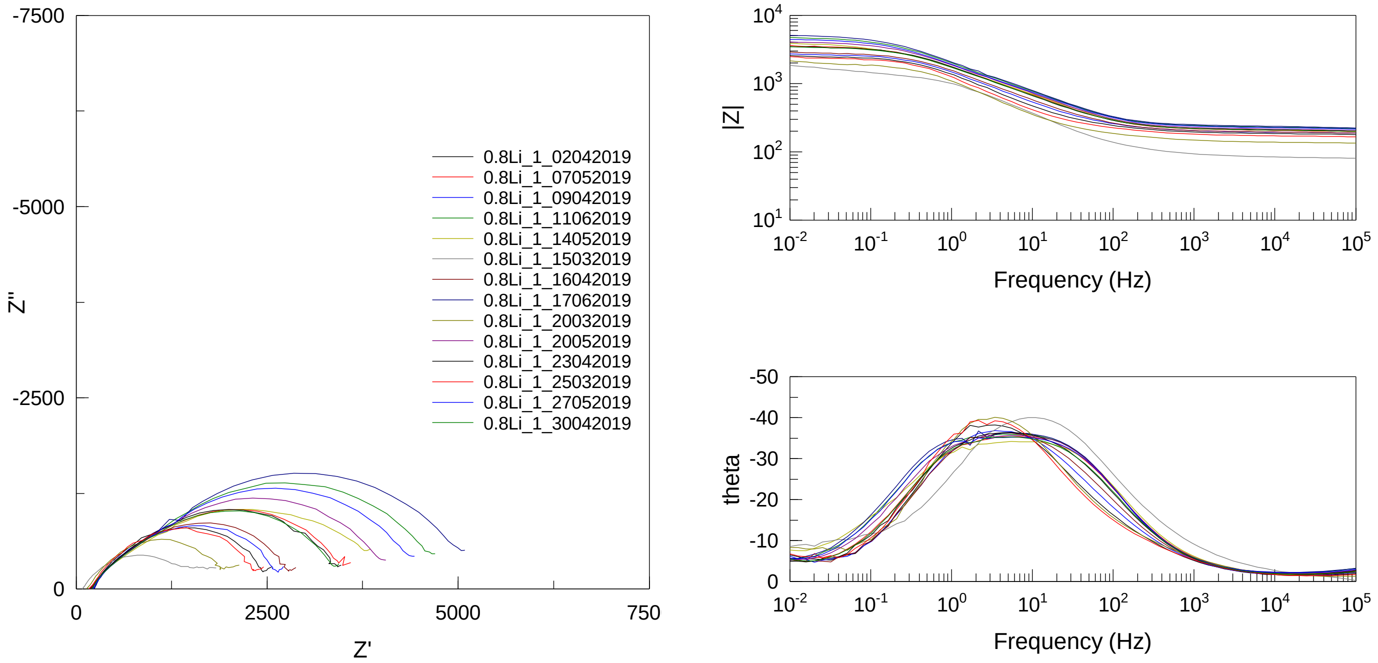

Appendix 16. EIS measurement result 0.8Li_1

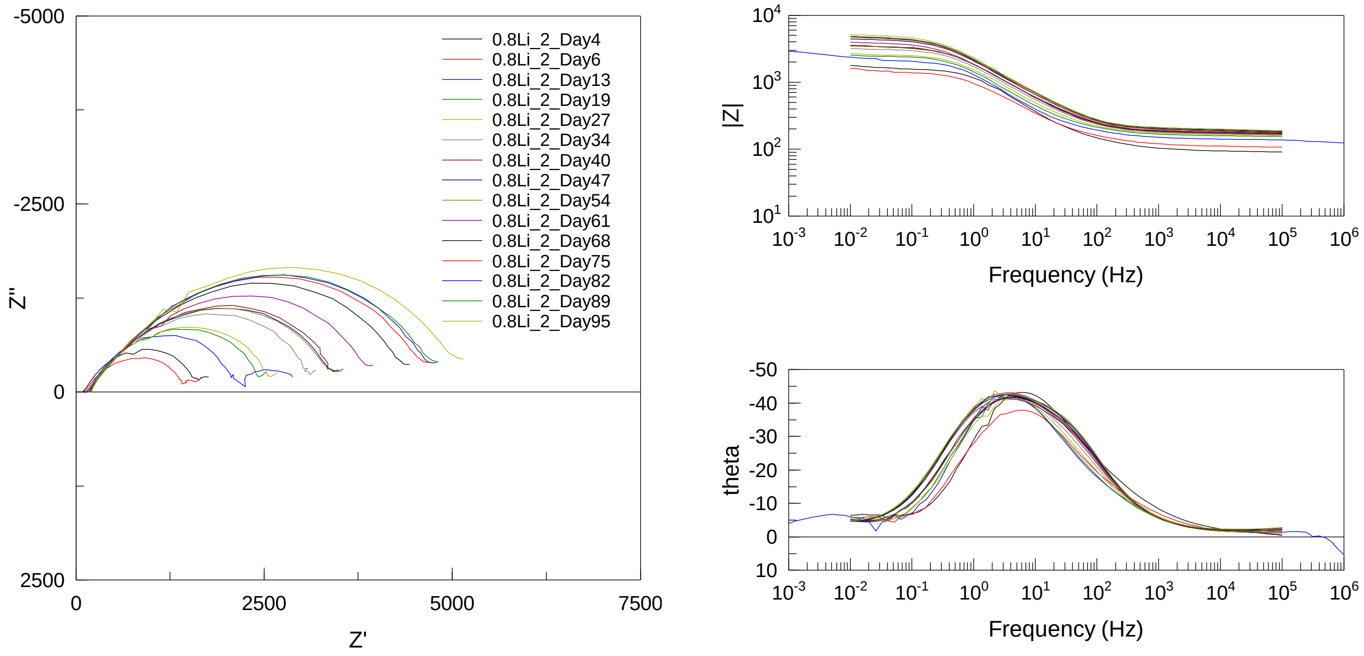

Appendix 17. EIS measurement result 0.8Li_2

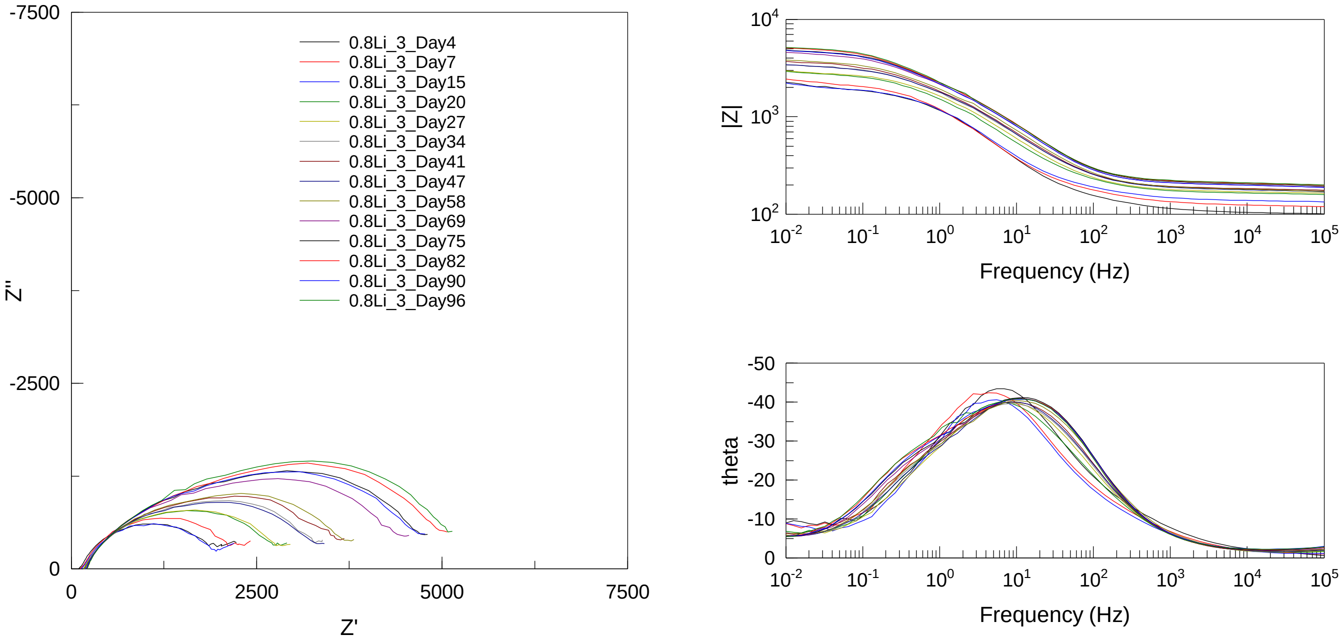

Appendix 18. EIS measurement result 0.8Li_3

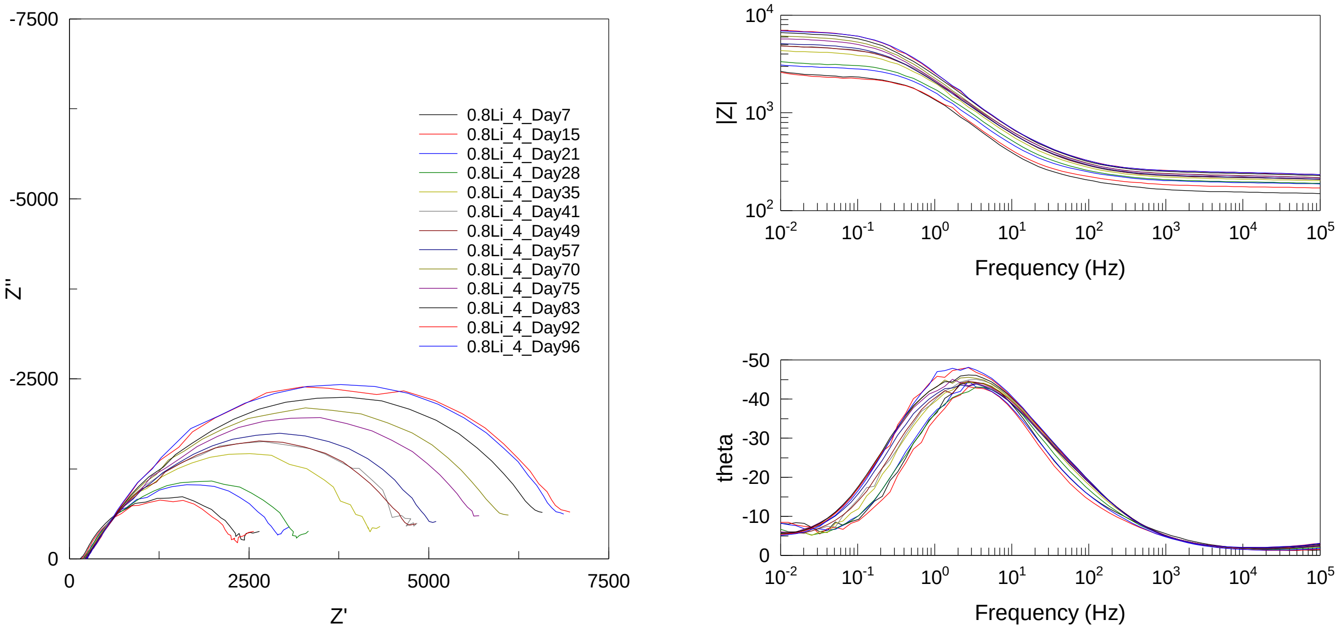

Appendix 19. EIS measurement result 0.8Li_4

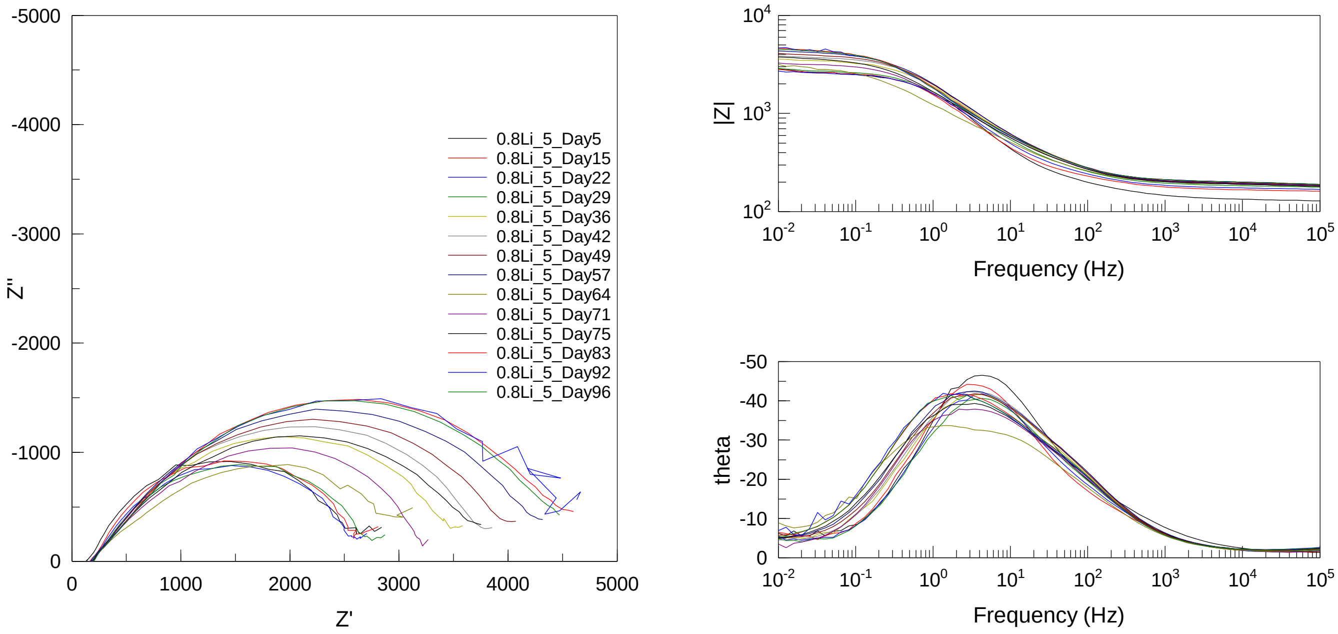

Appendix 20. EIS measurement result 0.8Li_5

APPENDIX B

CORROSION RATE CALCULATION

w-to-c ratio	Sample Number	Date	Day	Rt (ohm)	Rt (µohm)	Error%	icorr max	icorr min	icorr (µA/cm2)	vcorr max	vcorr min	**vcorr (µm/yr)**
0.36	1	15-03-2019	1	855.6	0.000856	1.326	14.93178	14.54097	14.7337876	162.7564	158.4966	**160.5982848**
0.36	1	20-03-2019	6	1938	0.001938	0.59112	6.543442	6.466537	6.504761956	71.32351	70.48525	**70.90190532**
0.36	1	25-03-2019	12	2960	0.00296	1.198	4.310501	4.208444	4.258861037	46.98446	45.87204	**46.4215853**
0.36	1	02-04-2019	19	3400	0.0034	1.5283	3.765259	3.651902	3.707714315	41.04132	39.80573	**40.41408603**
0.36	1	09-04-2019	26	4226	0.004226	0.365	2.993945	2.972168	2.983016723	32.634	32.39663	**32.51488228**
0.36	1	23-04-2019	40	6165	0.006165	0.33792	2.051739	2.037919	2.044805948	22.36396	22.21332	**22.28838483**
0.36	1	30-04-2019	47	6851	0.006851	0.41	1.847632	1.832543	1.840056732	20.13919	19.97472	**20.05661838**
0.36	1	07-05-2019	54	6795	0.006795	0.4083	1.862827	1.847677	1.855221291	20.30482	20.13968	**20.22191207**
0.36	1	14-05-2019	61	7040	0.00704	0.43007	1.798392	1.782989	1.790657482	19.60247	19.43458	**19.51816655**
0.36	1	20-05-2019	67	7574	0.007574	0.488	1.67257	1.656325	1.664408327	18.23102	18.05395	**18.14205077**
0.36	1	27-05-2019	74	8165	0.008165	0.51437	1.551918	1.536034	1.543934926	16.9159	16.74277	**16.82889069**
0.36	1	03-06-2019	81	6773	0.006773	0.44785	1.86962	1.852949	1.861247404	20.37886	20.19714	**20.28759671**
0.36	1	11-06-2019	89	8490	0.00849	0.61151	1.493968	1.475808	1.484832588	16.28426	16.08631	**16.18467521**
0.36	1	17-06-2019	95	9581	0.009581	1.5202	1.336064	1.29605	1.315752914	14.56309	14.12695	**14.34170676**

Appendix 21. Corrosion rate calculation for 0.36_1

w-to-c ratio	Sample Number	Date	Day	Rt (ohm)	Rt (µohm)	Error%	icorr max	icorr min	icorr (µA/cm2)	vcorr max	vcorr min	**vcorr (µm/yr)**
0.8	1	15-03-2019	1	464.4	0.000464	0.90536	27.3932	26.90164	27.14519524	298.5859	293.2279	**295.8826281**
0.8	1	20-03-2019	6	298.7	0.000299	1.0003	42.63007	41.78566	42.20364469	464.6678	455.4637	**460.0197272**
0.8	1	25-03-2019	12	465.9	0.000466	1.107	27.36068	26.76155	27.05779925	298.2314	291.7009	**294.9300118**
0.8	1	02-04-2019	19	584.2	0.000584	0.51799	21.69098	21.46742	21.57861806	236.4316	233.9949	**235.2069368**
0.8	1	09-04-2019	26	713.6	0.000714	0.4009	17.73679	17.59514	17.66567919	193.331	191.787	**192.5559032**
0.8	1	16-04-2019	33	2698	0.002698	1.595	4.748168	4.599079	4.672434644	51.75503	50.12996	**50.92953762**
0.8	1	23-04-2019	40	3446	0.003446	1.1015	3.698965	3.618364	3.65822074	40.31872	39.44017	**39.87460607**
0.8	1	30-04-2019	47	2734	0.002734	1.053	4.65998	4.562863	4.610910267	50.79378	49.73521	**50.25892191**
0.8	1	07-05-2019	54	7997	0.007997	2.0413	1.609219	1.544835	1.576369722	17.54048	16.8387	**17.18242997**

Appendix 22. Corrosion rate calculation for 0.8_1

w-to-c ratio	Sample Number	Date	Day	Rt (ohm)	Rt (µohm)	Error%	icorr max	icorr min	icorr (µA/cm2)	vcorr max	vcorr min	**vcorr (µm/yr)**
0.8Li	1	15-03-2019	1	1045	0.001045	1.367	12.23057	11.90069	12.06337672	133.3132	129.7176	**131.4908062**
0.8Li	1	20-03-2019	6	1669	0.001669	4.2543	7.888775	7.244941	7.553162774	85.98765	78.96986	**82.32947424**
0.8Li	1	25-03-2019	12	1938	0.001938	14.622	7.61878	5.674968	6.504761956	83.0447	61.85715	**70.90190532**
0.8Li	1	02-04-2019	19	1879	0.001879	22.495	8.656228	5.476966	6.709009404	94.35288	59.69893	**73.1282025**
0.8Li	1	09-04-2019	26	1206	0.001206	28.891	14.69986	8.109896	10.45292593	160.2285	88.39787	**113.9368926**
0.8Li	1	16-04-2019	33	1725	0.001725	9.66	8.089394	6.664197	7.307958649	88.1744	72.63975	**79.65674928**
0.8Li	1	23-04-2019	40	2401	0.002401	6.7576	5.630923	4.918064	5.250407609	61.37706	53.6069	**57.22944294**
0.8Li	1	30-04-2019	47	2458	0.002458	4.636	5.377976	4.901423	5.128652836	58.61994	53.42551	**55.90231591**
0.8Li	1	07-05-2019	54	2527	0.002527	6.1531	5.315694	4.699452	4.988614432	57.94107	51.22403	**54.37589731**
0.8Li	1	14-05-2019	61	3864	0.003864	1.0541	3.297238	3.22845	3.26248154	35.93989	35.19011	**35.56104878**
0.8Li	1	20-05-2019	67	3069	0.003069	5.244	4.334925	3.902932	4.107601391	47.25068	42.54196	**44.77285517**
0.8Li	1	27-05-2019	74	3877	0.003877	4.9992	3.422647	3.09673	3.251542087	37.30685	33.75436	**35.44180874**
0.8Li	1	03-06-2019	81	4311	0.004311	6.4677	3.126407	2.746561	2.924200573	34.07784	29.93752	**31.87378624**
0.8Li	1	11-06-2019	89	4030	0.00403	8.9139	3.434219	2.872082	3.128096444	37.43299	31.30569	**34.09625124**
0.8Li	1	17-06-2019	95	5422	0.005422	1.2098	2.353487	2.297223	2.325014509	25.65301	25.03973	**25.34265815**

Appendix 23. Corrosion rate calculation for 0.8Li_1

w-to-c ratio	Sample Number	Date	Day	Rt (ohm)	Rt (µohm)	Error%	icorr max	icorr min	icorr (µA/cm2)	vcorr max	vcorr min	**vcorr (µm/yr)**
0.36Li	1	15-03-2019	1	9939	0.009939	0.83003	1.278976	1.257919	1.268359862	13.94084	13.71131	**13.8251225**
0.36Li	1	20-03-2019	6	12963	0.012963	0.73424	0.979671	0.965389	0.972477719	10.67841	10.52274	**10.60000714**
0.36Li	1	25-03-2019	12	13376	0.013376	0.94774	0.951469	0.933603	0.942451306	10.37101	10.17627	**10.27271924**
0.36Li	1	02-04-2019	19	11191	0.011191	1.0435	1.13834	1.114828	1.126461323	12.4079	12.15163	**12.27842842**
0.36Li	1	09-04-2019	26	11482	0.011482	0.83967	1.107209	1.08877	1.097912269	12.06858	11.8676	**11.96724373**
0.36Li	1	16-04-2019	33	11430	0.01143	0.72125	1.11092	1.095009	1.102907145	12.10902	11.9356	**12.02168788**
0.36Li	1	23-04-2019	40	13333	0.013333	0.64466	0.951626	0.939435	0.945490788	10.37272	10.23984	**10.30584958**
0.36Li	1	30-04-2019	47	12760	0.01276	0.62856	0.994198	0.981778	0.987948955	10.83676	10.70138	**10.76864361**
0.36Li	1	07-05-2019	54	11993	0.011993	0.61581	1.057645	1.044699	1.051132216	11.52833	11.38722	**11.45734116**
0.36Li	1	14-05-2019	61	12621	0.012621	0.58067	1.004663	0.993063	0.998829623	10.95083	10.82439	**10.88724289**
0.36Li	1	20-05-2019	67	11332	0.011332	0.73363	1.120667	1.104343	1.11244517	12.21527	12.03734	**12.12565236**
0.36Li	1	27-05-2019	74	15043	0.015043	0.67247	0.843686	0.832415	0.838012941	9.196183	9.073326	**9.134341056**
0.36Li	1	03-06-2019	81	17149	0.017149	0.72407	0.740461	0.729816	0.735099928	8.071029	7.95499	**8.012589218**
0.36Li	1	11-06-2019	89	15665	0.015665	0.64992	0.810003	0.799542	0.804738504	8.829031	8.715009	**8.771649697**
0.36Li	1	17-06-2019	95	17284	0.017284	1.64992	0.741594	0.71752	0.729358289	8.083375	7.820966	**7.950005352**

Appendix 24. Corrosion rate calculation for 0.36Li_1

w-to-c ratio	Sample Number	Date	Day	Rt (ohm)	Rt (μohm)	Error%	icorr max	icorr min	icorr (μA/cm2)	vcorr max	vcorr min	**vcorr (μm/yr)**
0.36	2	20-03-2019	6	2664	0.002664	0.60233	4.760743	4.703736	4.732067819	51.8921	51.27072	**51.57953923**
0.36	2	26-03-2019	13	4417	0.004417	1.22284	2.889357	2.819547	2.854025055	31.49399	30.73306	**31.1088731**
0.36	2	02-04-2019	19	4609	0.004609	1.302	2.771214	2.699979	2.735133146	30.20624	29.42978	**29.81295129**
0.36	2	10-04-2019	27	4226	0.004226	0.365	2.993945	2.972168	2.983016723	32.634	32.39663	**32.51488228**
0.36	2	23-04-2019	40	1902	0.001902	1.5211	6.730254	6.528574	6.627880478	73.35977	71.16146	**72.24389721**
0.36	2	30-04-2019	47	2124	0.002124	0.71582	5.977927	5.892953	5.935135909	65.15941	64.23319	**64.6929814**
0.36	2	07-05-2019	54	2315	0.002315	0.87512	5.49353	5.398214	5.445455149	59.87948	58.84054	**59.35546112**
0.36	2	14-05-2019	61	2484	0.002484	0.85668	5.118823	5.031864	5.074971284	55.79517	54.84732	**55.317187**
0.36	2	21-05-2019	68	2962	0.002962	0.78093	4.289483	4.223007	4.255985371	46.75537	46.03077	**46.39024055**
0.36	2	28-05-2019	75	3158	0.003158	1.1088	4.036597	3.948063	3.991839351	43.99891	43.03389	**43.51104892**
0.36	2	04-06-2019	82	3235	0.003235	1.1997	3.944143	3.850629	3.896824937	42.99116	41.97186	**42.47539181**
0.36	2	11-06-2019	89	3393	0.003393	0.79484	3.745131	3.686065	3.715363593	40.82193	40.17811	**40.49746316**
0.36	2	17-06-2020	95	3636	0.003636	0.91213	3.498975	3.435721	3.46705959	38.13883	37.44936	**37.79094953**

Appendix 25. Corrosion rate calculation for 0.3_2

w-to-c ratio	Sample Number	Date	Day	Rt (ohm)	Rt (μohm)	Error%	icorr max	icorr min	icorr (μA/cm2)	vcorr max	vcorr min	**vcorr (μm/yr)**
0.8	2	18-03-2019	4	359.1	0.000359	0.72348	35.36089	34.85291	35.10506452	385.4337	379.8967	**382.6452033**
0.8	2	20-03-2019	6	409	0.000409	0.84588	31.08502	30.56354	30.82207499	338.8267	333.1426	**335.9606174**
0.8	2	26-03-2019	13	1095	0.001095	1.0459	11.63422	11.39337	11.5125376	126.813	124.1878	**125.4866598**
0.8	2	02-04-2019	19	3035	0.003035	1.1824	4.203317	4.105079	4.153617354	45.81616	44.74536	**45.27442916**
0.8	2	10-04-2019	27	3732	0.003732	0.84228	3.406568	3.349661	3.377874778	37.13159	36.51131	**36.81883508**
0.8	2	17-04-2019	34	4334	0.004334	0.91045	2.935408	2.882439	2.908682203	31.99594	31.41859	**31.70463602**
0.8	2	23-04-2019	40	4731	0.004731	0.69964	2.683375	2.646088	2.664601283	29.24879	28.84236	**29.04415398**
0.8	2	30-04-2019	47	4559	0.004559	0.77796	2.78681	2.743785	2.765130219	30.37623	29.90725	**30.13991939**
0.8	2	07-05-2019	54	4822	0.004822	2.2097	2.673389	2.557796	2.614315361	29.13994	27.87997	**28.49603743**

Appendix 26. Corrosion rate calculation for 0.8_2

w-to-c ratio	Sample Number	Date	Day	Rt (ohm)	Rt (µohm)	Error%	icorr max	icorr min	icorr (µA/cm2)	vcorr max	vcorr min	**vcorr (µm/yr)**
0.8Li	2	18-03-2019	4	917.1	0.000917	14.507	16.07822	12.00429	13.74575147	175.2526	130.8468	**149.828691**
0.8Li	2	20-03-2019	6	925.8	0.000926	16.547	16.31646	11.68334	13.61657882	177.8495	127.3484	**148.4207091**
0.8Li	2	26-03-2019	13	1646	0.001646	3.6819	7.95147	7.386733	7.658705146	86.67103	80.51539	**83.47988609**
0.8Li	2	02-04-2019	19	1310	0.00131	18.342	11.78461	8.131581	9.623075321	128.4522	88.63423	**104.891521**
0.8Li	2	10-04-2019	27	1485	0.001485	33.597	12.78413	6.354217	8.489042875	139.347	69.26096	**92.53056734**
0.8Li	2	17-04-2019	34	2888	0.002888	3.8016	4.537537	4.205174	4.365037628	49.45915	45.83639	**47.57891015**
0.8Li	2	23-04-2019	40	2694	0.002694	9.8623	5.19136	4.259307	4.679372186	56.58582	46.42644	**51.00515683**
0.8Li	2	30-04-2019	47	2920	0.00292	5.7911	4.582584	4.080874	4.317201599	49.95016	44.48153	**47.05749743**
0.8Li	2	07-05-2019	54	2939	0.002939	6.0711	4.56653	4.043789	4.289291824	49.77518	44.0773	**46.75328088**
0.8Li	2	14-05-2019	61	3320	0.00332	3.7666	3.945675	3.659228	3.797056828	43.00785	39.88559	**41.38791943**
0.8Li	2	21-05-2019	68	3031	0.003031	5.712	4.411059	3.934368	4.159098868	48.08054	42.88461	**45.33417766**
0.8Li	2	28-05-2019	75	4345	0.004345	1.1088	2.933849	2.869501	2.901318451	31.97895	31.27757	**31.62437112**
0.8Li	2	04-06-2019	82	5034	0.005034	1.2279	2.535349	2.473841	2.504217058	27.6353	26.96486	**27.29596593**
0.8Li	2	11-06-2019	89	4993	0.004993	0.73637	2.54351	2.506325	2.524780427	27.72426	27.31894	**27.52010665**
0.8Li	2	17-06-2020	95	5277	0.005277	1.73637	2.431114	2.348128	2.388900639	26.49914	25.5946	**26.03901696**

Appendix 27 Corrosion rate calculation for 0.8Li_2

w-to-c ratio	Sample Number	Date	Day	Rt (ohm)	Rt (µohm)	Error%	icorr max	icorr min	icorr (µA/cm2)	vcorr max	vcorr min	**vcorr (µm/yr)**
0.36Li	2	18-03-2019	4	14346	0.014346	1.7915	0.894757	0.863262	0.878727776	9.752855	9.40956	**9.578132755**
0.36Li	2	20-03-2019	6	16432	0.016432	1.2555	0.77693	0.757663	0.767175552	8.468536	8.258528	**8.362213516**
0.36Li	2	02-04-2019	19	14459	0.014459	1.7345	0.88725	0.856996	0.871860341	9.671022	9.341254	**9.503277716**
0.36Li	2	10-04-2019	27	15055	0.015055	1.3636	0.848921	0.826081	0.83734498	9.253237	9.004278	**9.127060279**
0.36Li	2	17-04-2019	34	16606	0.016606	1.526	0.770901	0.747727	0.759136979	8.40282	8.150221	**8.274593069**
0.36Li	2	23-04-2019	40	16862	0.016862	1.277	0.757282	0.738185	0.747611711	8.254376	8.046217	**8.148967649**
0.36Li	2	30-04-2019	47	15540	0.01554	1.006	0.819455	0.803132	0.811211626	8.932063	8.75414	**8.842206725**
0.36Li	2	07-05-2019	54	14588	0.014588	0.85077	0.871566	0.856861	0.864150581	9.500065	9.339781	**9.419241329**
0.36Li	2	14-05-2019	61	16196	0.016196	0.90776	0.785485	0.771352	0.77835445	8.561784	8.407741	**8.484063503**
0.36Li	2	21-05-2019	68	15066	0.015066	1.0198	0.845355	0.828287	0.836733617	9.214365	9.028326	**9.120396423**
0.36Li	2	28-05-2019	75	17869	0.017869	1.0537	0.712993	0.698124	0.705480367	7.771626	7.609554	**7.689735995**
0.36Li	2	04-06-2019	82	19718	0.019718	1.05	0.64611	0.632683	0.639325929	7.0426	6.896242	**6.968652627**
0.36Li	2	11-06-2019	89	18555	0.018555	0.89642	0.685543	0.673362	0.679397934	7.472422	7.339643	**7.405437483**
0.36Li	2	17-06-2020	95	20125	0.020125	1.3064	0.634688	0.618319	0.626396456	6.918099	6.739674	**6.827721367**

Appendix 28. Corrosion rate calculation for 0.36Li_2

w-to-c ratio	Sample Number	Date	Day	Rt (ohm)	Rt (µohm)	Error%	icorr max	icorr min	icorr (µA/cm2)	vcorr max	vcorr min	**vcorr (µm/yr)**
0.36	3	18-03-2019	4	968.9	0.000969	0.60233	13.08971	12.93297	13.01086662	142.6778	140.9693	**141.8184462**
0.36	3	21-03-2019	7	1246	0.001246	0.695	10.18817	10.04753	10.11735848	111.051	109.5181	**110.2792075**
0.36	3	28-03-2019	15	1194	0.001194	0.81158	10.64437	10.47298	10.55798046	116.0236	114.1555	**115.081987**
0.36	3	03-04-2019	20	1294	0.001294	0.99745	9.840214	9.64585	9.742062341	107.2583	105.1398	**106.1884795**
0.36	3	10-04-2019	27	1290	0.00129	0.97791	9.868778	9.677632	9.772270287	107.5697	105.4862	**106.5177461**
0.36	3	17-04-2019	34	1897	0.001897	1.0149	6.713485	6.578584	6.645349852	73.17699	71.70656	**72.43431339**
0.36	3	24-04-2019	41	2245	0.002245	0.87835	5.665005	5.566355	5.615246624	61.74856	60.67326	**61.2061882**
0.36	3	30-04-2019	47	2118	0.002118	0.97469	6.010533	5.894496	5.951949325	65.51481	64.25001	**64.87624764**
0.36	3	16-05-2019	63	3193	0.003193	2.1394	4.034395	3.865387	3.948082891	43.9749	42.13272	**43.03410351**
0.36	3	22-05-2019	69	2652	0.002652	3.164	4.908794	4.607692	4.753479891	53.50586	50.22385	**51.81293081**
0.36	3	28-05-2019	75	2492	0.002492	2.8824	5.208818	4.916953	5.058679242	56.77612	53.59479	**55.13960373**
0.36	3	04-06-2019	82	4146	0.004146	1.1912	3.077232	3.004783	3.040576138	33.54183	32.75214	**33.14227991**
0.36	3	12-06-2019	90	3601	0.003601	2.5384	3.591935	3.414094	3.500757753	39.1521	37.21363	**38.15825951**
0.36	3	18-06-2020	96	4492	0.004492	1.9651	2.862627	2.752288	2.806373257	31.20263	29.99994	**30.5894685**

Appendix 29. Corrosion rate calculation for 0.36_3

w-to-c ratio	Sample Number	Date	Day	Rt (ohm)	Rt (µohm)	Error%	icorr max	icorr min	icorr (µA/cm2)	vcorr max	vcorr min	**vcorr (µm/yr)**
0.8	3	18-03-2019	4	423.6	0.000424	0.9094	30.03287	29.49155	29.75974662	327.3582	321.4579	**324.3812382**
0.8	3	21-03-2019	7	1050	0.00105	1.5739	12.19792	11.8199	12.00593207	132.9573	128.8369	**130.8646595**
0.8	3	28-03-2019	15	1692	0.001692	1.1236	7.535155	7.367706	7.450489758	82.13319	80.308	**81.21033836**
0.8	3	03-04-2019	20	1990	0.00199	0.83668	6.388237	6.282226	6.334788276	69.63179	68.47626	**69.04919221**
0.8	3	10-04-2019	27	2025	0.002025	1.2629	6.304923	6.147659	6.225298109	68.72366	67.00949	**67.85574938**
0.8	3	17-04-2019	34	2200	0.0022	0.64136	5.767092	5.693588	5.730103941	62.8613	62.0601	**62.45813296**
0.8	3	24-04-2019	41	2403	0.002403	0.73233	5.284739	5.207899	5.246037732	57.60366	56.7661	**57.18181128**
0.8	3	30-04-2019	47	2384	0.002384	0.51305	5.315117	5.260857	5.287847596	57.93477	57.34334	**57.6375388**
0.8	3	09-05-2019	58	2242	0.002242	0.9099	5.674392	5.57206	5.622760334	61.85087	60.73546	**61.28808765**
0.8	3	16-05-2019	63	3691	0.003691	0.52582	3.43345	3.397532	3.415396551	37.42461	37.03309	**37.22782241**
0.8	3	22-05-2019	69	2680	0.00268	0.51399	4.728119	4.679763	4.703816668	51.53649	51.00942	**51.27160168**
0.8	3	28-05-2019	75	2801	0.002801	0.535	4.524825	4.476667	4.500617162	49.32059	48.79567	**49.05672706**
0.8	3	04-06-2019	82	2989	0.002989	0.50288	4.238857	4.196437	4.217540539	46.20354	45.74117	**45.97119187**
0.8	3	12-06-2019	90	3019	0.003019	0.4793	4.195741	4.155712	4.175630563	45.73357	45.29726	**45.51437314**
0.8	3	18-06-2020	96	3113	0.003113	0.70173	4.078161	4.021325	4.049543421	44.45196	43.83244	**44.14002329**

Appendix 30. Corrosion rate calculation for 0.8_3

w-to-c ratio	Sample Number	Date	Day	Rt (ohm)	Rt (µohm)	Error%	icorr max	icorr min	icorr (µA/cm2)	vcorr max	vcorr min	**vcorr (µm/yr)**
0.8Li	3	18-03-2019	4	1733	0.001733	2.6683	7.473642	7.08517	7.274223122	81.4627	77.22835	**79.28903203**
0.8Li	3	21-03-2019	7	2051	0.002051	1.2601	6.224821	6.069895	6.146381604	67.85054	66.16185	**66.99555948**
0.8Li	3	28-03-2019	15	1831	0.001831	0.76232	6.937775	6.8328	6.884887313	75.62175	74.47751	**75.04527171**
0.8Li	3	03-04-2019	20	2722	0.002722	0.62439	4.660336	4.6025	4.631237572	50.79767	50.16725	**50.48048953**
0.8Li	3	10-04-2019	27	2665	0.002665	2.4886	4.851015	4.615433	4.730292184	52.87606	50.30821	**51.5601848**
0.8Li	3	17-04-2019	34	3167	0.003167	5.845	4.227598	3.760683	3.980495317	46.08082	40.99145	**43.38739896**
0.8Li	3	24-04-2019	41	3579	0.003579	0.77022	3.549617	3.495355	3.522276801	38.69082	38.09937	**38.39281713**
0.8Li	3	30-04-2019	47	3288	0.003288	0.60052	3.857174	3.811125	3.834011153	42.0432	41.54126	**41.79072156**
0.8Li	3	09-05-2019	58	3702	0.003702	0.79314	3.432472	3.378452	3.405248155	37.41395	36.82513	**37.11720489**
0.8Li	3	22-05-2019	69	4439	0.004439	1.5755	2.885339	2.795832	2.839880304	31.45019	30.47457	**30.95469531**
0.8Li	3	28-05-2019	75	4609	0.004609	0.90026	2.75998	2.71073	2.735133146	30.08378	29.54695	**29.81295129**
0.8Li	3	04-06-2019	82	4947	0.004947	0.82363	2.56942	2.527441	2.548257261	28.00668	27.5491	**27.77600414**
0.8Li	3	12-06-2019	90	4607	0.004607	1.0309	2.764823	2.7084	2.736320527	30.13657	29.52156	**29.82589375**
0.8Li	3	18-06-2020	96	5162	0.005162	2.0309	2.492746	2.393511	2.442121013	27.17093	26.08927	**26.61911904**

Appendix 31. Corrosion rate calculation for 0.8Li_3

w-to-c ratio	Sample Number	Date	Day	Rt (ohm)	Rt (µohm)	Error%	icorr max	icorr min	icorr (µA/cm2)	vcorr max	vcorr min	**vcorr (µm/yr)**
0.36Li	3	18-03-2019	4	9933	0.009933	1.1037	1.28329	1.255272	1.269126011	13.98786	13.68246	**13.83347352**
0.36Li	3	21-03-2019	7	12636	0.012636	0.85882	1.006286	0.989149	0.997643928	10.96852	10.78172	**10.87431881**
0.36Li	3	28-03-2019	15	7903	0.007903	1.472	1.61895	1.57198	1.595119407	17.64656	17.13458	**17.38680153**
0.36Li	3	03-04-2019	20	14751	0.014751	2.9641	0.880707	0.83	0.854601632	9.599703	9.046996	**9.315157786**
0.36Li	3	10-04-2019	27	12758	0.012758	0.82207	0.996294	0.980047	0.988103831	10.85961	10.68251	**10.77033175**
0.36Li	3	17-04-2019	34	15265	0.015265	0.44876	0.829548	0.822136	0.825825658	9.042077	8.961285	**9.001499673**
0.36Li	3	24-04-2019	41	17344	0.017344	0.50762	0.730544	0.723164	0.72683514	7.962924	7.88249	**7.922503027**
0.36Li	3	30-04-2019	47	15501	0.015501	0.33793	0.81601	0.810514	0.813252608	8.894511	8.834599	**8.864453422**
0.36Li	3	09-05-2019	58	16927	0.016927	0.45817	0.748169	0.741344	0.744740868	8.155039	8.080652	**8.117675459**
0.36Li	3	22-05-2019	69	19282	0.019282	0.67135	0.658201	0.649422	0.653782215	7.174391	7.078703	**7.126226144**
0.36Li	3	28-05-2019	75	21455	0.021455	0.50198	0.59053	0.584631	0.587566007	6.436781	6.372481	**6.404469471**
0.36Li	3	04-06-2019	82	23280	0.02328	0.30304	0.543151	0.539869	0.541504668	5.920342	5.884568	**5.902400881**
0.36Li	3	12-06-2019	90	22304	0.022304	1.015	0.570996	0.559521	0.565200353	6.223856	6.098781	**6.160683846**
0.36Li	3	18-06-2020	96	25444	0.025444	0.81237	0.499508	0.491458	0.495449956	5.444635	5.356887	**5.400404516**

Appendix 32 Corrosion rate calculation for 0.36Li_3

w-to-c ratio	Sample Number	Date	Day	Rt (ohm)	Rt (µohm)	Error%	icorr max	icorr min	icorr (µA/cm2)	vcorr max	vcorr min	**vcorr (µm/yr)**
0.36	4	19-03-2019	5	2093	0.002093	1.186	6.095333	5.952447	6.023042843	66.43914	64.88167	**65.65116699**
0.36	4	21-03-2019	7	2716	0.002716	0.7047	4.674409	4.608989	4.641468582	50.95106	50.23798	**50.59200755**
0.36	4	28-03-2019	15	2941	0.002941	1.0849	4.333388	4.240371	4.28637493	47.23393	46.22005	**46.72148674**
0.36	4	04-04-2019	21	4808	0.004808	1.7505	2.668642	2.576821	2.62192776	29.0882	28.08734	**28.57901258**
0.36	4	11-04-2019	28	9608	0.009608	0.97791	1.325013	1.299349	1.31205544	14.44264	14.1629	**14.3014043**
0.36	4	18-04-2019	35	2655	0.002655	0.59751	4.77665	4.719907	4.748108727	52.06548	51.44698	**51.75438512**
0.36	4	24-04-2019	41	1165	0.001165	1.4527	10.98031	10.66585	10.82079714	119.6854	116.2578	**117.9466888**
0.36	4	02-05-2019	49	1419	0.001419	0.397	8.919292	8.848753	8.883882079	97.22028	96.4514	**96.83431466**
0.36	4	10-05-2019	57	1669	0.001669	0.3486	7.579585	7.526924	7.553162774	82.61748	82.04347	**82.32947424**
0.36	4	23-05-2019	70	5309	0.005309	1.7612	2.417071	2.333406	2.374501539	26.34607	25.43412	**25.88206677**
0.36	4	28-05-2019	75	8011	0.008011	0.69712	1.584662	1.562721	1.573614863	17.27281	17.03366	**17.15240201**

Appendix 33 Corrosion rate calculation for 0.36_4

w-to-c ratio	Sample Number	Date	Day	Rt (ohm)	Rt (µohm)	Error%	icorr max	icorr min	icorr (µA/cm2)	vcorr max	vcorr min	**vcorr (µm/yr)**
0.8	4	19-03-2019	5	428.5	0.000429	0.8774	29.67985	29.16356	29.4194368	323.5103	317.8828	**320.6718611**
0.8	4	21-03-2019	7	444.4	0.000444	0.37399	28.47334	28.26116	28.36685119	310.3594	308.0466	**309.198678**
0.8	4	28-03-2019	15	569.7	0.00057	0.3693	22.20986	22.04642	22.12783688	242.0875	240.306	**241.193422**
0.8	4	04-04-2019	21	759.1	0.000759	7.269	17.90858	15.48146	16.60680894	195.2036	168.7479	**181.0142175**
0.8	4	11-04-2019	28	3711	0.003711	1.6219	3.452994	3.342773	3.396989671	37.63763	36.43623	**37.02718742**
0.8	4	18-04-2019	35	5297	0.005297	0.99275	2.403744	2.356487	2.379880814	26.20081	25.68571	**25.94070087**
0.8	4	24-04-2019	41	4495	0.004495	1.2365	2.839612	2.770246	2.80450026	30.95177	30.19568	**30.56905284**
0.8	4	02-05-2019	49	4548	0.004548	1.9168	2.825987	2.719687	2.771818089	30.80325	29.64459	**30.21281717**

Appendix 34. Corrosion rate calculation for 0.8_4

w-to-c ratio	Sample Number	Date	Day	Rt (ohm)	Rt (µohm)	Error%	icorr max	icorr min	icorr (µA/cm2)	vcorr max	vcorr min	**vcorr (µm/yr)**
0.8Li	4	19-03-2019	5	2047	0.002047	0.54226	6.191969	6.125178	6.15839212	67.49246	66.76444	**67.12647411**
0.8Li	4	21-03-2019	7	2220	0.00222	0.83788	5.726462	5.631298	5.678481383	62.41844	61.38115	**61.89544707**
0.8Li	4	28-03-2019	15	2106	0.002106	1.2504	6.061659	5.911941	5.985863566	66.07208	64.44015	**65.24591287**
0.8Li	4	04-04-2019	21	2587	0.002587	7.269	5.254892	4.542705	4.872914059	57.27832	49.51548	**53.11476324**
0.8Li	4	11-04-2019	28	2868	0.002868	9.44	4.853663	4.016335	4.395477221	52.90493	43.77805	**47.91070171**
0.8Li	4	18-04-2019	35	3571	0.003571	25.109	4.713741	2.821674	3.530167648	51.37978	30.75624	**38.47882736**
0.8Li	4	24-04-2019	41	4256	0.004256	24.718	3.934526	2.37495	2.961989819	42.88633	25.88695	**32.28568903**
0.8Li	4	02-05-2019	49	3864	0.003864	37.655	5.232948	2.370042	3.26248154	57.03914	25.83346	**35.56104878**
0.8Li	4	10-05-2019	57	4605	0.004605	7.653	2.964372	2.542901	2.73750894	32.31166	27.71762	**29.83884745**
0.8Li	4	23-05-2019	70	6325	0.006325	0.74814	2.008103	1.978279	1.993079632	21.88832	21.56324	**21.72456798**
0.8Li	4	28-05-2019	75	5293	0.005293	1.9781	2.429742	2.335481	2.381679326	26.48419	25.45674	**25.96030465**
0.8Li	4	05-06-2019	83	6378	0.006378	0.9198	1.994866	1.958503	1.976517509	21.74404	21.34768	**21.54404084**
0.8Li	4	14-06-2019	92	6752	0.006752	0.49802	1.876381	1.857784	1.867036237	20.45255	20.24985	**20.35069498**
0.8Li	4	18-06-2020	96	7053	0.007053	0.87691	1.803169	1.77182	1.787356964	19.65454	19.31283	**19.48219091**

Appendix 35 Corrosion rate calculation for 0.8Li_4

w-to-c ratio	Sample Number	Date	Day	Rt (ohm)	Rt (µohm)	Error%	icorr max	icorr min	icorr (µA/cm2)	vcorr max	vcorr min	**vcorr (µm/yr)**
0.36Li	4	19-03-2019	5	11916	0.011916	1.1886	1.07065	1.045498	1.057924528	11.67009	11.39593	**11.53137735**
0.36Li	4	21-03-2019	7	14464	0.014464	0.67626	0.877493	0.865705	0.871558951	9.564675	9.436179	**9.499992568**
0.36Li	4	28-03-2019	15	9746	0.009746	0.4181	1.298908	1.288092	1.293477188	14.1581	14.0402	**14.09890134**
0.36Li	4	04-04-2019	21	12782	0.012782	0.54013	0.991604	0.98095	0.986248527	10.80849	10.69236	**10.75010894**
0.36Li	4	11-04-2019	28	13976	0.013976	0.50145	0.906537	0.897491	0.901991176	9.881253	9.782649	**9.831703814**
0.36Li	4	18-04-2019	35	15961	0.015961	0.55287	0.794205	0.785472	0.789814465	8.656839	8.561643	**8.608977664**
0.36Li	4	24-04-2019	41	15132	0.015132	0.52225	0.837458	0.828756	0.833084105	9.128289	9.03344	**9.080616739**
0.36Li	4	02-05-2019	49	14539	0.014539	0.38538	0.870417	0.863734	0.86706298	9.48755	9.414704	**9.450986485**
0.36Li	4	10-05-2019	57	14627	0.014627	0.44318	0.865683	0.858044	0.861846494	9.435945	9.352678	**9.394126786**
0.36Li	4	23-05-2019	70	15193	0.015193	0.71	0.835673	0.82389	0.829739266	9.108831	8.980397	**9.044158001**
0.36Li	4	28-05-2019	75	16620	0.01662	7.2653	0.817922	0.707123	0.758497513	8.91535	7.70764	**8.267622894**
0.36Li	4	05-06-2019	83	15739	0.015739	0.90173	0.808243	0.793797	0.800954868	8.809849	8.652387	**8.730408063**
0.36Li	4	14-06-2019	92	16451	0.016451	2.0739	0.782518	0.75072	0.766289506	8.529448	8.182851	**8.35255562**
0.36Li	4	18-06-2020	96	20318	0.020318	1.2343	0.6282	0.612882	0.620446337	6.847382	6.680409	**6.76286507**

Appendix 36. Corrosion rate calculation for 0.36Li_4

w-to-c ratio	Sample Number	Date	Day	Rt (ohm)	Rt (µohm)	Error%	icorr max	icorr min	icorr (µA/cm2)	vcorr max	vcorr min	**vcorr (µm/yr)**
0.36	5	19-03-2019	5	622.6	0.000623	1.4826	20.55243	19.95191	20.24771711	224.0215	217.4758	**220.7001165**
0.36	5	28-03-2019	15	2512	0.002512	2.1265	5.127438	4.913909	5.018403133	55.88908	53.56161	**54.70059415**
0.36	5	05-04-2019	22	4209	0.004209	1.985	3.055721	2.93677	2.99506502	33.30736	32.01079	**32.64620872**
0.36	5	12-04-2019	29	4714	0.004714	1.3524	2.710872	2.638527	2.674210579	29.54851	28.75995	**29.14889531**
0.36	5	19-04-2019	36	5006	0.005006	2.1153	2.572643	2.466059	2.518223865	28.04181	26.88005	**27.44864013**
0.36	5	25-04-2019	42	4246	0.004246	1.0418	3.000222	2.938354	2.968965772	32.70242	32.02806	**32.36172692**
0.36	5	02-05-2019	49	5157	0.005157	2.358	2.503522	2.388176	2.444488786	27.28839	26.03111	**26.64492777**
0.36	5	17-05-2019	64	11849	0.011849	1.6778	1.082061	1.046351	1.063906547	11.79447	11.40522	**11.59658136**
0.36	5	24-05-2019	71	11462	0.011462	1.2174	1.113382	1.0866	1.099828012	12.13587	11.84394	**11.98812533**
0.36	5	28-05-2019	75	11439	0.011439	1.3575	1.117205	1.08728	1.102039398	12.17754	11.85135	**12.01222943**
0.36	5	05-06-2019	83	11563	0.011563	1.7316	1.109432	1.071664	1.090221281	12.09281	11.68114	**11.88341196**

Appendix 37. Corrosion rate calculation for 0.36_5

w-to-c ratio	Sample Number	Date	Day	Rt (ohm)	Rt (µohm)	Error%	icorr max	icorr min	icorr (µA/cm2)	vcorr max	vcorr min	**vcorr (µm/yr)**
0.8	5	19-03-2019	5	429	0.000429	0.40231	29.50385	29.2674	29.38514841	321.5919	319.0147	**320.2981177**
0.8	5	28-03-2019	15	1810	0.00181	1.0739	7.040374	6.890767	6.964767221	76.74007	75.10936	**75.91596271**
0.8	5	05-04-2019	22	2426	0.002426	0.86562	5.241675	5.151708	5.196302007	57.13426	56.15361	**56.63969188**
0.8	5	12-04-2019	29	2773	0.002773	1.0599	4.594761	4.498383	4.546061547	50.0829	49.03238	**49.55207086**
0.8	5	19-04-2019	36	4491	0.004491	2.0353	2.865316	2.751007	2.806998145	31.23194	29.98598	**30.59627978**
0.8	5	25-04-2019	42	4777	0.004777	0.62954	2.655661	2.622433	2.638942573	28.94671	28.58452	**28.76447404**
0.8	5	02-05-2019	49	7073	0.007073	1.0518	1.801248	1.763752	1.782302937	19.63361	19.22489	**19.42710201**
0.8	5	10-05-2019	57	8377	0.008377	1.2409	1.52377	1.486417	1.504861964	16.6091	16.20195	**16.4029954**

Appendix 38 Corrosion rate calculation for 0.8_5

w-to-c ratio	Sample Number	Date	Day	Rt (ohm)	Rt (µohm)	Error%	icorr max	icorr min	icorr (µA/cm2)	vcorr max	vcorr min	**vcorr (µm/yr)**
0.8Li	5	19-03-2019	5	2527	0.002527	0.98548	5.038266	4.939932	4.988614432	54.91709	53.84526	**54.37589731**
0.8Li	5	28-03-2019	15	2479	0.002479	1.0291	5.138083	5.033408	5.085207209	56.00511	54.86415	**55.42875857**
0.8Li	5	05-04-2019	22	2380	0.00238	1.4702	5.375769	5.21999	5.296734735	58.59589	56.8979	**57.73440861**
0.8Li	5	12-04-2019	29	2502	0.002502	1.6809	5.1246	4.955169	5.038460699	55.85814	54.01134	**54.91922162**
0.8Li	5	19-04-2019	36	3231	0.003231	3.4082	4.039317	3.773056	3.901649232	44.02856	41.12631	**42.52797663**
0.8Li	5	25-04-2019	42	3572	0.003572	0.51425	3.547422	3.511123	3.529179359	38.6669	38.27125	**38.46805501**
0.8Li	5	02-05-2019	49	3814	0.003814	0.54426	3.323339	3.28736	3.305251356	36.22439	35.83222	**36.02723977**
0.8Li	5	10-05-2019	57	4098	0.004098	0.49561	3.091512	3.06102	3.0761905	33.69748	33.36512	**33.53047645**
0.8Li	5	17-05-2019	64	2805	0.002805	2.5981	4.614078	4.380392	4.494199169	50.29344	47.74627	**48.98677095**
0.8Li	5	24-05-2019	71	2382	0.002382	3.4673	5.482378	5.114937	5.292287435	59.75792	55.75282	**57.68593304**
0.8Li	5	28-05-2019	75	3527	0.003527	0.52226	3.592972	3.555637	3.574207165	39.16339	38.75645	**38.9588581**
0.8Li	5	05-06-2019	83	4324	0.004324	0.55543	2.931693	2.899305	2.915409036	31.95545	31.60243	**31.77795849**
0.8Li	5	14-06-2019	92	4448	0.004448	0.92075	2.860472	2.808277	2.834134143	31.17914	30.61022	**30.89206216**
0.8Li	5	18-06-2020	96	4193	0.004193	1.92075	3.065372	2.949835	3.00649384	33.41255	32.1532	**32.77078285**

Appendix 39. Corrosion rate calculation for 0.8Li_5

w-to-c ratio	Sample Number	Date	Day	Rt (ohm)	Rt (µohm)	Error%	icorr max	icorr min	icorr (µA/cm2)	vcorr max	vcorr min	**vcorr (µm/yr)**
0.36Li	5	19-03-2019	5	8371	0.008371	1.0777	1.522347	1.489884	1.505940589	16.59358	16.23974	**16.41475242**
0.36Li	5	28-03-2019	15	8655	0.008655	0.90519	1.46983	1.44346	1.456525554	16.02115	15.73371	**15.87612854**
0.36Li	5	05-04-2019	22	9870	0.00987	0.85344	1.288221	1.266419	1.277226816	14.04161	13.80396	**13.92177229**
0.36Li	5	12-04-2019	29	10679	0.010679	0.85296	1.190625	1.170485	1.18046902	12.97781	12.75829	**12.86711232**
0.36Li	5	19-04-2019	36	11625	0.011625	0.82385	1.093415	1.075546	1.084406767	11.91822	11.72345	**11.82003376**
0.36Li	5	25-04-2019	42	12288	0.012288	0.65612	1.032673	1.01921	1.025897515	11.25614	11.10939	**11.18228292**
0.36Li	5	02-05-2019	49	11738	0.011738	0.65028	1.080997	1.067029	1.073967343	11.78287	11.63061	**11.70624404**
0.36Li	5	17-05-2019	64	13154	0.013154	0.60076	0.964149	0.952634	0.958357053	10.50923	10.38371	**10.44609187**
0.36Li	5	24-05-2019	71	13662	0.013662	0.95477	0.931617	0.913995	0.922722052	10.15462	9.962551	**10.05767036**
0.36Li	5	28-05-2019	75	13081	0.013081	0.8375	0.971844	0.955701	0.963705273	10.5931	10.41714	**10.50438747**
0.36Li	5	05-06-2019	83	13661	0.013661	1.7316	0.93905	0.907083	0.922789596	10.23565	9.8872	**10.0584066**
0.36Li	5	14-06-2019	92	10387	0.010387	1.2117	1.228541	1.199125	1.21365444	13.39109	13.07046	**13.2288334**
0.36Li	5	18-06-2020	96	13565	0.013565	0.52442	0.934219	0.924472	0.929320212	10.18299	10.07675	**10.12959031**

Appendix 40. Corrosion rate calculation for 0.36Li_5

Total Measurement Period						
	Series 1	Series 2	Series 3	Series 4	Series 5	**Average**
0,36_1 (No Crack)	37.05148	-	-	-	-	**37.05148**
0,36_2 and 0,36_3 (Cracked)	-	46.71468	73.59138	-	-	**60.15303**
All 0,36Li	10.6919	8.410836	9.077171	9.528886	12.17025	**9.97581**
0,8_3 (No Wire Corrosion)	-	-	79.00723	-	-	**79.00723**
All 0,8Li	61.73601	64.71652	44.93195	38.60854	43.86317	**50.77124**

Appendix 41. Total measurement period corrosion rate calculation

Plateau Period						
	Series 1	Series 2	Series 3	Series 4	Series 5	**Average**
0,36_1 (No Crack)	18.65222	-	-	-	-	**18.65222**
0,36_2 and 0,36_3 (Cracked)	-	51.36385	47.24489	-	-	**49.30437**
All 0,36Li	9.934813	8.100714	6.987352	8.635417	10.91419	**8.914497**
0,8_3 (No Wire Corrosion)	-	-	49.01342	-	-	**49.01342**
All 0,8Li	41.62178	38.22417	32.78618	25.84342	38.78868	**35.45285**

Appendix 42. Steady state Period Corrosion Rate Calculation

APPENDIX C

STERN-GEARY CONSTANT CALCULATION

	0.3_1			0.3_2			0.3_3			0.3_4			0.3_5			0.3Li_1			0.3Li_2			0.3Li_3			0.3Li_4			0.3Li_5			0.8_1			0.8_2			0.8_3			0.8_4			0.8_5			0.8Li_1			0.8Li_2			0.8Li_3			0.8Li_4			0.8Li_5		
	ba	bc	B	ba	bc	B	ba	bc	B	ba	bc	B	ba	bc	B	ba	bc	B	ba	bc	B	ba	bc	B	ba	bc	B	ba	bc	B	ba	bc	B	ba	bc	B	ba	bc	B	ba	bc	B	ba	bc	B	ba	bc	B	ba	bc	B	ba	bc	B	ba	bc	B	ba	bc	B
02-04-2019	119	151	29	106	185	29										127	203	34	109	195	30										119	168	30	111	184	30										107	200	30	104	193	29									
03-04-2019							119	195	32													117	184	31													115	177	30													114	188	31						
04-04-2019										118	231	34													115	182	31													113	167	29													103	179	28			
05-04-2019													120	180	31													111	213	32													126	188	33													117	208	33
09-04-2019	113	203	32													125	211	34													117	169	30													110	197	31												
10-04-2019				111	216	32	124	233	35										113	208	32	128	201	34										125	202	34	123	188	32										112	209	32	122	212	34						
11-04-2019										123	200	33													122	190	32													133	168	32													100	191	29			
12-04-2019													128	196	34													113	208	32													124	199	33													124	199	33
16-04-2019	149	177	35													125	213	34													125	165	31													113	200	31												
17-04-2019				141	198	36	123	188	32										115	209	32	127	191	33										120	194	32	118	178	31										113	201	31	117	205	32						
18-04-2019										136	201	35													125	206	34													128	162	31													108	178	29			
19-04-2019													129	187	33													120	199	33													126	212	34													113	197	31
23-04-2019	113	215	32	117	203	32										120	187	32	117	197	32										128	197	34	115	186	31										114	185	31	115	193	31									
24-04-2019							125	208	34	130	173	32										126	184	32	127	178	32										119	180	31	128	169	32										122	203	33	111	182	30			
25-04-2019													128	190	33													116	182	31													141	225	38													119	193	32
B AVERAGE	32			32			33			34			33			33			32			33			32			32			31			32			31			31			34			31			31			32			29			32		
	33															32															32															31														
	32																																																											
B MIN	32			32			32			32			31			32			32			32			32			31			30			31			31			31			33			31			31			32			29			31		
B MAX	35			36			35			35			34			34			32			34			34			33			34			34			32			32			38			31			32			34			30			33		

Appendix 43. Stern-Geary constant calculation for cemented samples

	Al_1			**Al_2**			**Al_3**		
	ba	bc	B	ba	bc	B	ba	bc	B
02-04-2019									
03-04-2019									
04-04-2019									
05-04-2019	148	178	35						
09-04-2019				117	185	31			
10-04-2019							105	201	30
11-04-2019	115	192	31						
12-04-2019				88	226	28			
16-04-2019							121	209	33
17-04-2019	100	213	30						
18-04-2019				86	207	26			
19-04-2019							116	200	32
23-04-2019	95	191	28						
24-04-2019				92	202	27			
25-04-2019							94	219	29
B AVERAGE	31			28			31		
	30								
B MIN	28			26			29		
B MAX	31			31			33		

Appendix 44. Stern-Geary constant calculation for bare aluminum samples

APPENDIX D

CORROSION RATE

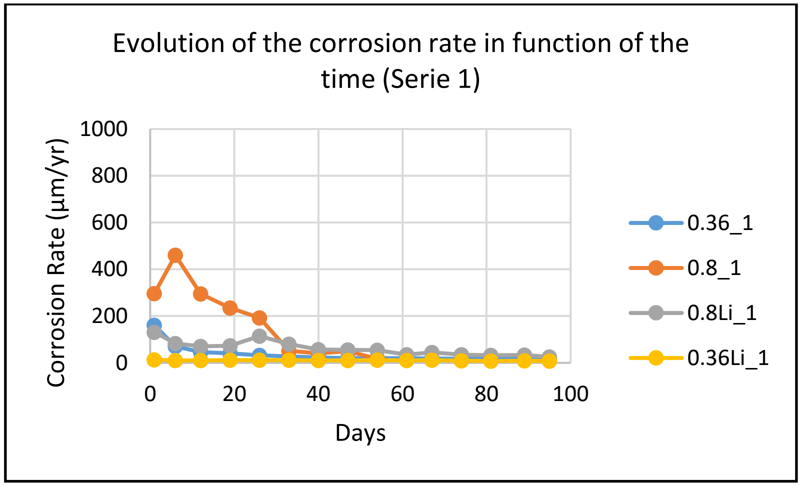

Appendix 45. Corrosion rate comparison of Series 1

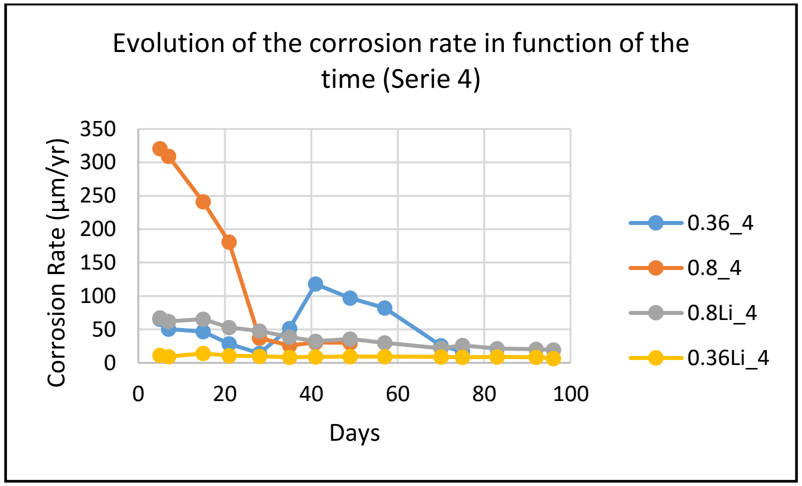

Appendix 47. Corrosion rate comparison of Series 4

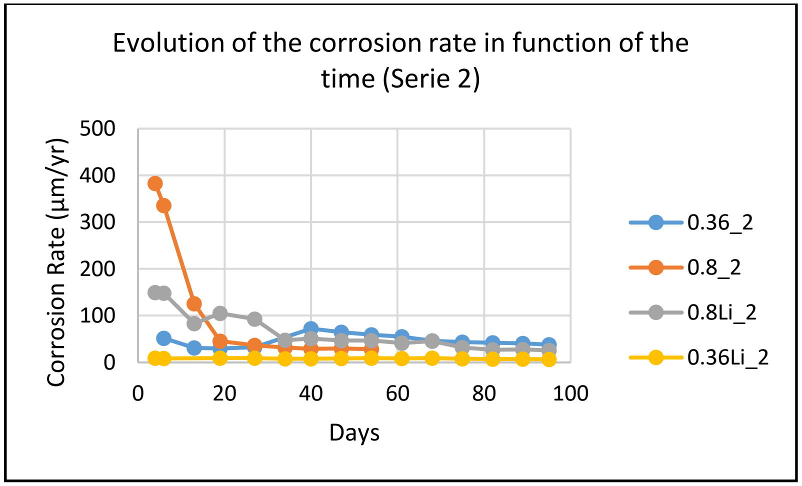

Appendix 46. Corrosion rate comparison of Series 2

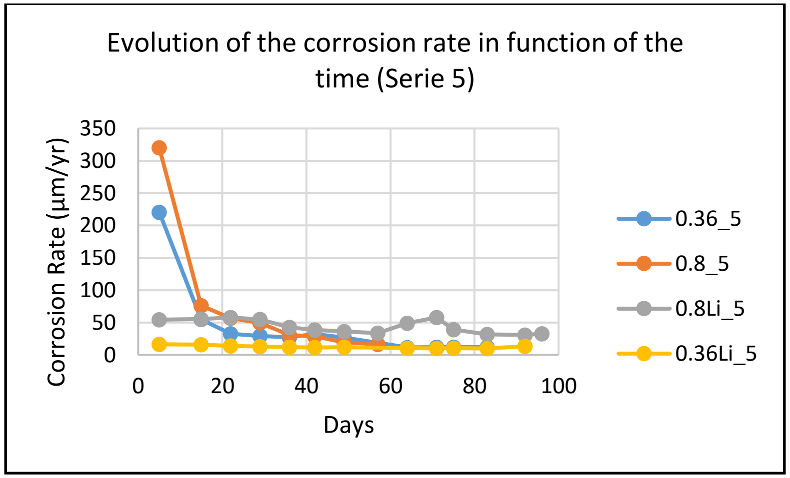

Appendix 48. Corrosion rate comparison of Series 5

APPENDIX E

PORE SIZE DISTRIBUTION IN DIFFERENT CEMENTS

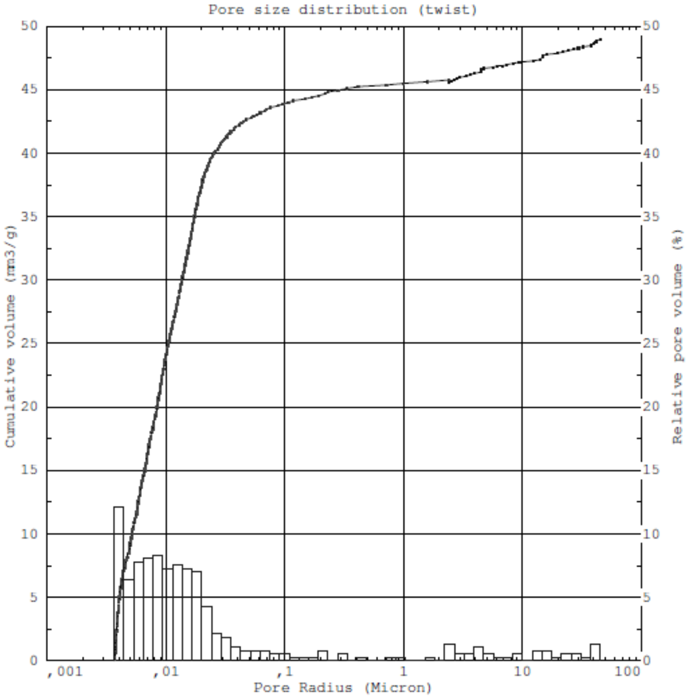

Appendix 49. Pore Size Distribution for 0.36

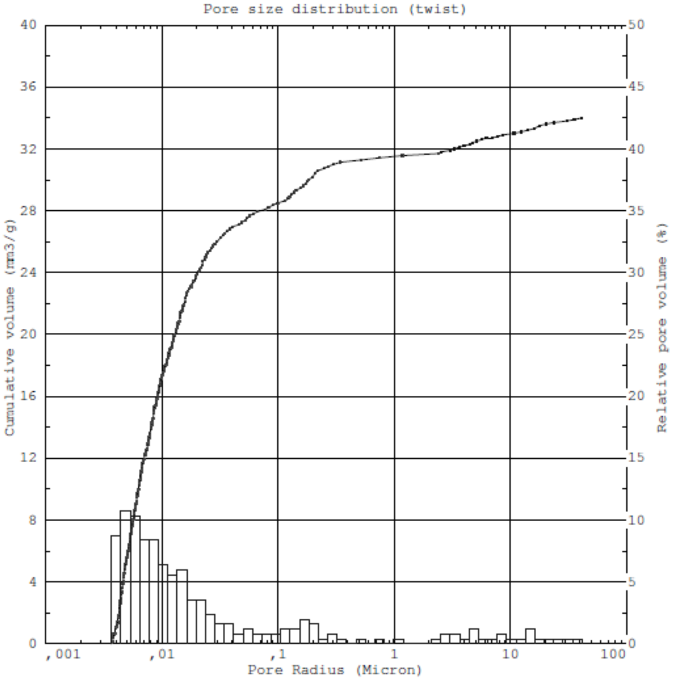

Appendix 50. Pore Size Distribution for 0.36Li

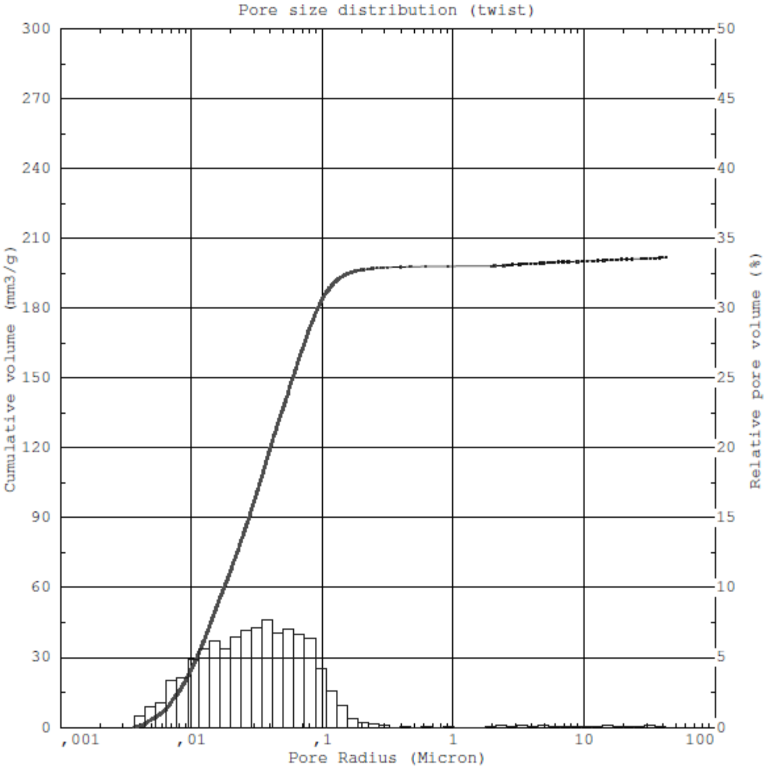

Appendix 51. Pore Size Distribution for 0.8

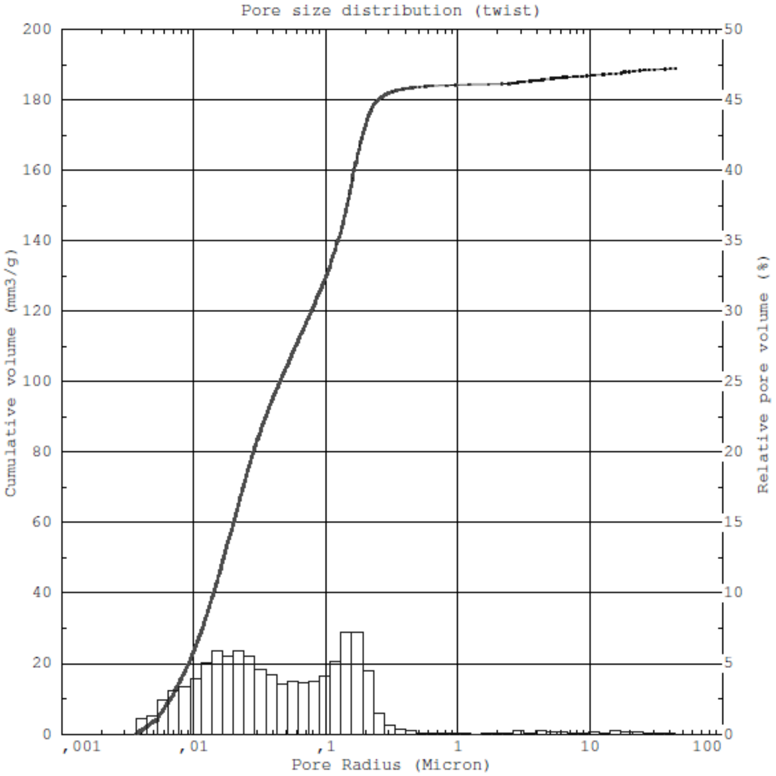

Appendix 52. Pore Size Distribution for 0.8Li

	0.36	**0.36Li**	**0.8**	**0.8Li**
Total Cumulative volume (mm3/g)	48.9766	34.0107	201.8425	188.8996
Total specific surface area (m2/g)	11.18	7.36	19.593	16.846
Average Pore Radius (nm)	10.724	10.121	31.627	38.732
Total Porosity (%)	10.0044	7.1093	30.3753	30.3414
Bulk density (g/cm3)	2.04269	2.09032	1.5049	1.60622
Apparent density (g/cm3)	2.26977	2.2503	2.16144	2.30585

Appendix 53. Summary of Mercury Porosimetry

APPENDIX F

CORROSION CALCULATION FROM STATIC CORROSION TEST

Corrosion rate calculation by using GC:

- Gas chromatography (GC) gives the result of H_2 content in µL/L.
- The result from GC is then divided by the head space of the container to obtain the H_2 volume in the headspace.
- Using 0,08988 g/L as the density of H_2 then the mass of H_2 can be calculated.
- The mass of H_2 is then used to calculate the number of moles of H_2 produced by dividing the mass with 2,01594 g/mole as the molar mass of H_2.
- The mole of H_2 correlates with Equation 6 in Section 2.3.1 which can be used to calculate the mol of corroded aluminum.
- The mole of aluminum is then used to calculate the mass of corroded aluminum by using 26,98 g/mole as the molar mass of aluminum.
- The volume of corroded Al is then calculated by dividing the mass of corroded aluminum with the density of aluminum (26.98 g/mol).
- The volume of corroded aluminum is then divided with aluminum surface area in contact with cement which is 10.8 cm^2 to obtain the thickness of aluminum that corrodes during the period of the test.
- The thickness obtained from calculation is obtained in centimeter, this thickness is converted to micron and divided by the test duration to obtain the corrosion rate of micron/days, the result is then multiplied by 365,25 days/year to obtain the corrosion rate in micron/year.

Corrosion rate calculation by measuring H_2 pressure:

- The barometer gives the pressure the gas inside the container.
- The pressure of H_2 is pressure measured by barometer minus 1 bar which is the pressure of Argon inside the container.
- The pressure of H_2 is used to calculate mole of H_2 using ideal gas law (see Section 2.8) by using the head space of the container as the gas volume, 8.314 J/K/mol as gas constant, and 295 K as the gas temperature.
- The mole of H_2 correlates with Equation 6 in Section 2.3.1 which can be used to calculate the mole of corroded aluminum.
- The mole of aluminum is then used to calculate the mass of corroded aluminum by using 26,98 g/mole as the molar mass of aluminum.
- The volume of corroded Al is then calculated by dividing the mass of corroded aluminum with the density of aluminum (26.98 g/mol).

- The volume of corroded aluminum is then divided with aluminum surface area in contact with cement which is 10.8 cm^2 to obtain the thickness of aluminum that corrodes during the period of the test.
- The thickness obtained from calculation is obtained in centimeter, this thickness is converted to micron and divided by the test duration to obtain the corrosion rate of micron/days, the result is then multiplied by 365,25 days/year to obtain the corrosion rate in micron/year.

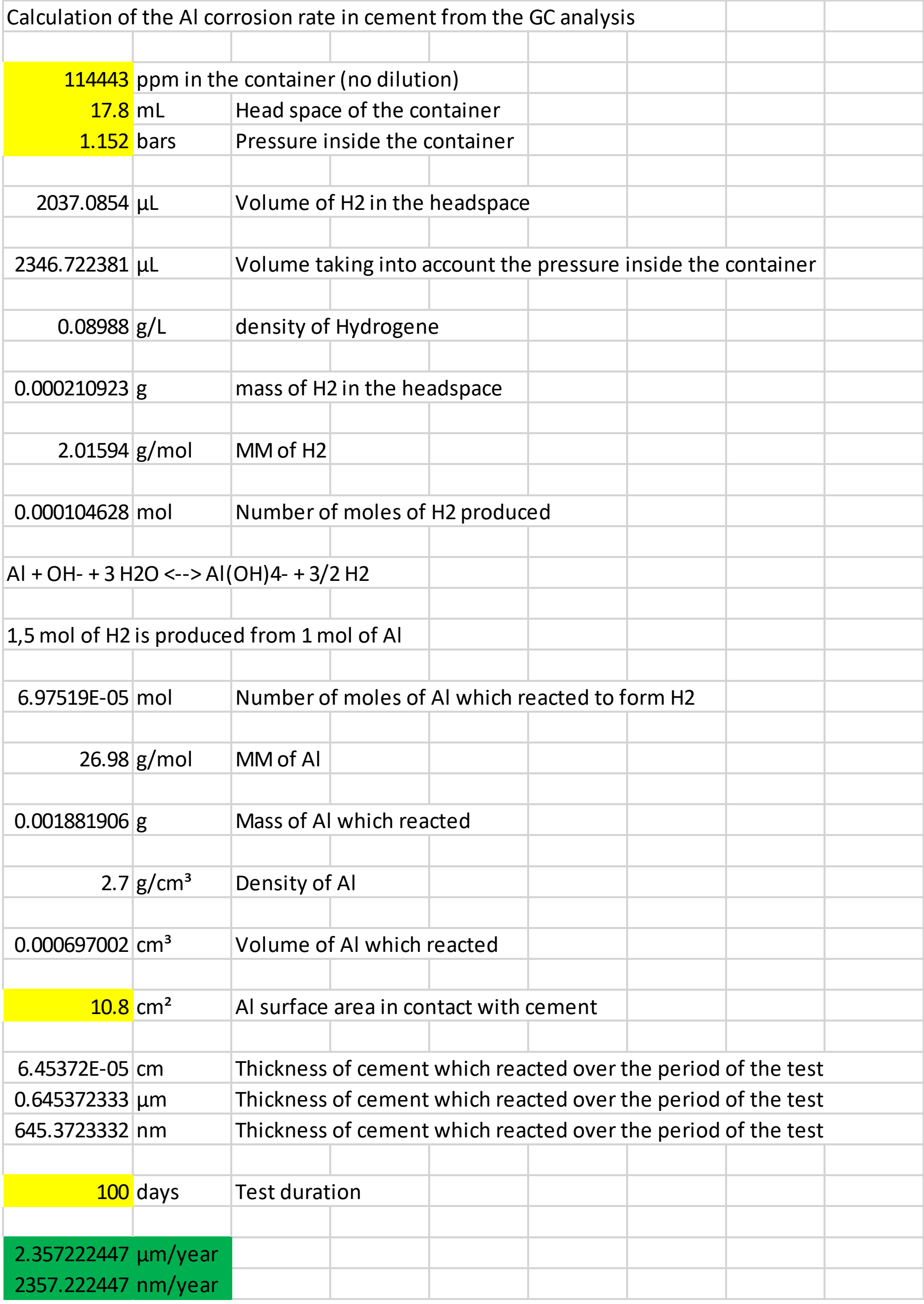

Calculation of the Al corrosion rate in cement from the GC analysis		
114443	ppm in the container (no dilution)	
17.8	mL	Head space of the container
1.152	bars	Pressure inside the container
2037.0854	µL	Volume of H2 in the headspace
2346.722381	µL	Volume taking into account the pressure inside the container
0.08988	g/L	density of Hydrogene
0.000210923	g	mass of H2 in the headspace
2.01594	g/mol	MM of H2
0.000104628	mol	Number of moles of H2 produced
Al + OH- + 3 H2O <--> Al(OH)4- + 3/2 H2		
1,5 mol of H2 is produced from 1 mol of Al		
6.97519E-05	mol	Number of moles of Al which reacted to form H2
26.98	g/mol	MM of Al
0.001881906	g	Mass of Al which reacted
2.7	g/cm³	Density of Al
0.000697002	cm³	Volume of Al which reacted
10.8	cm²	Al surface area in contact with cement
6.45372E-05	cm	Thickness of cement which reacted over the period of the test
0.645372333	µm	Thickness of cement which reacted over the period of the test
645.3723332	nm	Thickness of cement which reacted over the period of the test
100	days	Test duration
2.357222447	µm/year	
2357.222447	nm/year	

Appendix 54. Example of Corrosion rate calculation by GC

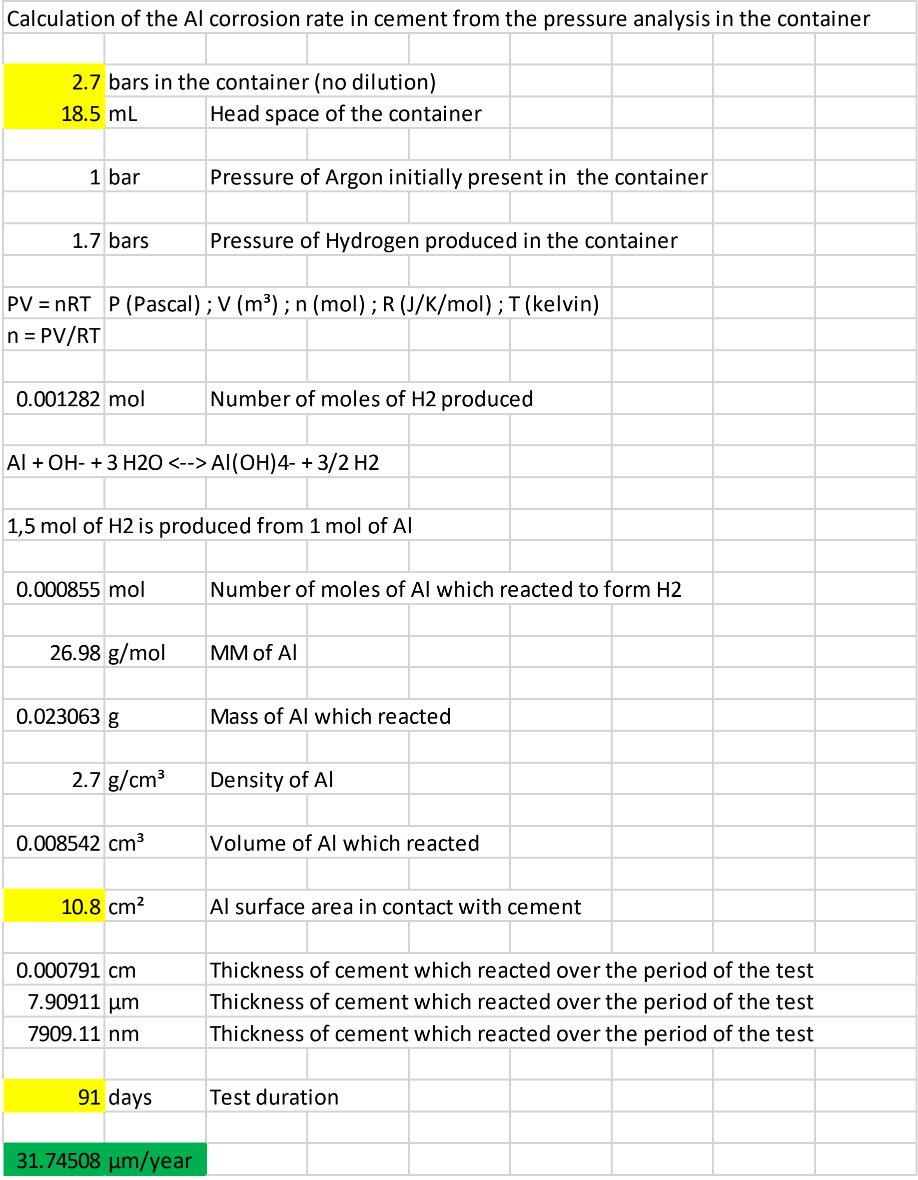

Calculation of the Al corrosion rate in cement from the pressure analysis in the container

2.7	bars in the container (no dilution)	
18.5	mL	Head space of the container
1	bar	Pressure of Argon initially present in the container
1.7	bars	Pressure of Hydrogen produced in the container
PV = nRT	P (Pascal) ; V (m³) ; n (mol) ; R (J/K/mol) ; T (kelvin)	
n = PV/RT		
0.001282	mol	Number of moles of H2 produced
Al + OH- + 3 H2O <--> Al(OH)4- + 3/2 H2		
1,5 mol of H2 is produced from 1 mol of Al		
0.000855	mol	Number of moles of Al which reacted to form H2
26.98	g/mol	MM of Al
0.023063	g	Mass of Al which reacted
2.7	g/cm³	Density of Al
0.008542	cm³	Volume of Al which reacted
10.8	cm²	Al surface area in contact with cement
0.000791	cm	Thickness of cement which reacted over the period of the test
7.90911	µm	Thickness of cement which reacted over the period of the test
7909.11	nm	Thickness of cement which reacted over the period of the test
91	days	Test duration
31.74508	µm/year	

Appendix 55. Example of Corrosion rate calculation by gas pressure measurement

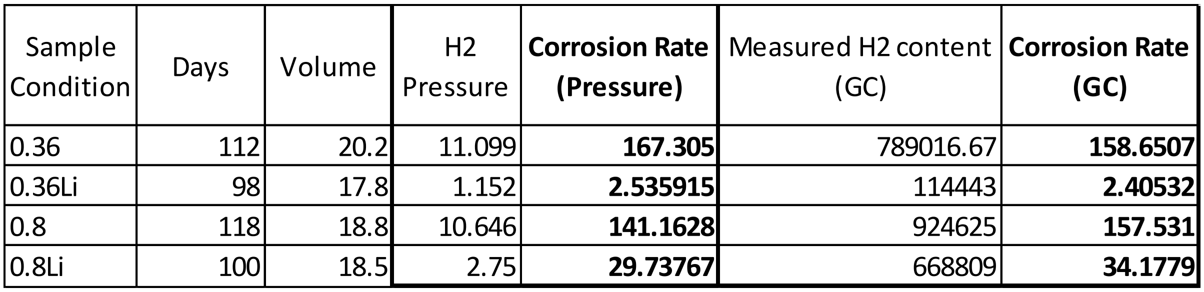

Sample Condition	Days	Volume	H2 Pressure	**Corrosion Rate (Pressure)**	Measured H2 content (GC)	**Corrosion Rate (GC)**
0.36	112	20.2	11.099	**167.305**	789016.67	**158.6507**
0.36Li	98	17.8	1.152	**2.535915**	114443	**2.40532**
0.8	118	18.8	10.646	**141.1628**	924625	**157.531**
0.8Li	100	18.5	2.75	**29.73767**	668809	**34.1779**

Appendix 56. Corrosion Rate from Static Corrosion Test

Investigation of The Corrosion Behavior of Metallic Aluminum Embedded in A Cement Matrix

The Belgian Reactor 1 (BR1) is a Belgian research reactor. Its natural metallic uranium fuel is encapsulated in an aluminum cladding. In Belgium, spent fuel of the BR1 is to be stored by means of geological disposal in a poorly indurated clay placed in supercontainers, involving the use of a cement buffer. Therefore, the corrosion of the fuel in these conditions (high pH and anaerobic) needs to be studied. In this Master thesis, the corrosion of aluminum cladding was investigated by observing the electrochemical behavior and the H_2 gas release when aluminum was embedded in Ordinary Portland Cement (OPC) immersed in limewater under anaerobic conditions. Four different conditions of OPC were tested to study the influence of different porosity, induced by different water-to-cement ratio, and the presence of $LiNO_3$ as corrosion inhibitor. Corrosion rates were calculated by measuring the H_2 gas release by gas chromatography and pressure sensors, and by the electrochemical impedance spectroscopy response. Corrosion rate ranges from 3 to 168 μm/y after three months of experiment. The lowest results were obtained when a cement with a lower porosity in presence of $LiNO_3$ was used, while the highest corrosion rates were observed when a cement possessing a higher porosity without $LiNO_3$ addition was used. In the conditions studied here, both cement porosity and the presence of a corrosion inhibitor play an important role on the corrosion of embedded aluminum in OPC cement.

Keywords: corrosion, aluminum, cement, EIS, hydrogen measurement